STUDY OF INFLUENCE OF OXYGEN VACANCIES ON PHOTOVOLTAIC EFFECT IN LEAD-FREE CERAMICS

WONG KI HEI

MPhil

The Hong Kong Polytechnic University

2022

The Hong Kong Polytechnic University

Department of Applied Physics

Study of Influence of Oxygen Vacancies on Photovoltaic Effect in Lead-free Ceramics

Wong Ki Hei

A thesis submitted in partial fulfilment of the requirements

for the degree of Master of Philosophy

August 2021

Certificate of Originality

I hereby declare that this thesis is my own work and that, to the best of my knowledge and belief, it reproduces no material previously published or written, nor material that has been accepted for the award of any other degree or diploma, except where due acknowledgement has been made in the text.

_____ (Signature)

Wong Ki Hei ___ (Name of candidate)

Abstract

The ferroelectric photovoltaic effect has received considerable research interest due to its fascinating features, including the above bandgap voltage and switchable polarization-dependent photocurrent. However, during the fabrication process of the common ABO_3 perovskite ferroelectric oxides, the formation of defects such as oxygen vacancies inside the ceramic is unpreventable. It has been reported that the defects (oxygen vacancies) would affect the photovoltaic response in ferroelectric photovoltaic devices. For example, the direction of the photocurrent response of the device can be independent of its polarization. In addition, the photocurrent may depend on the distribution of oxygen vacancies inside the ferroelectric material. In this study, we aim to study the influence of oxygen vacancies on the photovoltaic effect in ferroelectric ceramic oxide. The weak photocurrent generated by the ferroelectric material may even be enhanced by modifying the distribution of oxygen vacancies inside the ceramics.

In this work, Barium titanate-based ferroelectric ceramic $Ba_{0.9}Ca_{0.1}TiO_3$ (BCT) has been chosen as the based material due to its ferroelectric photovoltaic response and easy doping with other chemicals. In addition, Ca^{2+} ions in BCT ceramics can act as an acceptor inhibitor to reduce the possibility of the formation of the hexagonal structure. Therefore, the tetragonal structure of the BCT ceramics will be more stable. It is suggested that the formation of oxygen vacancies in BCT –ceramics can be promoted through acceptor doping. Since Fe^{3+} and Ti^{4+} share similar radii, Fe^{3+} has been chosen as the dopant to BCT ceramics. 0.025 mol and 0.1 mol Fe^{3+} is doped in BCT ceramic to fabricate the

$Ba_{0.9}Ca_{0.1}Ti_{0.975}Fe_{0.025}O_3$ (BCT-Fe-0.025) and $Ba_{0.9}Ca_{0.1}Ti_{0.9}Fe_{0.1}O_3$ (BCT-Fe-0.1) ceramics.

$Ba_{0.9}Ca_{0.1}Ti0_{.9}Fe_{0.1}O_3$ (BCT-Fe-0.1) and $Ba_{0.9}Ca_{0.1}Ti_{0.975}Fe_{0.025}O_3$ (BCT-Fe-0.025) have been fabricated by conventional solid-state reaction method. To study the influence of oxygen vacancies on the photocurrent response of the BCT-Fe-0.1 and BCT-Fe-0.025 ceramics, they are sintered in different atmospheres (O_2, N_2 and air) and their oxygen vacancies content are analyzed with the XPS O1s spectrums. The ferroelectric and dielectric properties of the BCT-Fe-0.1 and BCT-Fe-0.025 ceramics sintered in different atmospheres are also examined. It is revealed that the BCT-Fe-0.025 ceramic exhibits ferroelectric properties at room temperature, while the BCT-Fe-0.1 remains non-ferroelectric. In addition, the ferroelectric properties of the BCT-Fe-0.025 ceramics are also affected by the sintering atmosphere. The BCT-Fe-0.025 ceramics sintered in Air (BCT-Fe-0.025-Air) have the largest remnant polarization (4.5 $\mu C/cm^2$) and saturated polarization (18 $\mu C/cm^2$), while the BCT-Fe-0.025 ceramics sintered in O_2 (BCT-Fe-0.025-O_2) have the lowest remnant polarization (2.5 $\mu C/cm^2$) and saturated polarization (10 $\mu C/cm^2$). The remnant polarization and saturated polarization of the BCT-Fe-0.025 sintered in N_2 (BCT-Fe-0.025-N_2) are 3.5 $\mu C/cm^2$ and 15 $\mu C/cm^2$ respectively.

The photocurrent effect of non-ferroelectric BCT-Fe-0.1 ceramics have been investigated using vertical symmetric ITO and Au electrodes configuration. Photocurrent can be observed in non-ferroelectric BCT-Fe-0.1 oxides, and this should be attributed to the accumulation of oxygen vacancies which generate diffusion current and drift current that contribute to the photovoltaic response. The BCT-Fe-0.1 sintered in O_2, N_2 and Air have a significantly different photocurrent response. For the BCT-Fe-0.1 ceramics with ITO

electrodes, for 30 seconds of A.M. 1.5 solar light illumination, the average photocurrent generated by the as-fabricated BCT-Fe-0.1-Air and BCT-Fe-0.1-O_2 ceramics are 2.4 nA (4.8 nA/cm^2) and 3.5 nA (6.9 nA/cm^2) respectively. However, steady photocurrent cannot be observed in the BCT-Fe-0.1-N_2 ceramic and only sharp current peaks (0.38 nA or 0.75 nA/cm^2) are observed once the light source is turned on / off. Similar results can also be observed in ceramics with Au electrodes. The distribution of oxygen vacancies of the BCT-Fe-0.1 can be modified by applying an external field at a high temperature. As a result, the photocurrent of the BCT-Fe-0.1 ceramics can be switchable. Furthermore, the photocurrent response of the BCT-Fe-0.1 ceramics can even be enhanced by applying appropriate external electric fields.

The ferroelectric photovoltaic effect of BCT-Fe-0.025 ceramics sintered in O_2, N_2 and Air are also investigated with vertical symmetric Au electrode configuration. The ceramics are poled at 1kV/mm at room temperature. The steady photocurrent generated by the BCT-Fe-0.025-Air, BCT-Fe-0.025-N_2 and BCT-Fe-0.025-O_2 are 3.34 nA (6.68 nA/cm^2), 3.2 nA (6.4 nA/cm^2) and 2.2 nA (4.4 nA/cm^2) respectively. It illustrates that the sintering atmosphere would affect the ferroelectric properties of the BCT-Fe-0.025 ceramics and influence the ferroelectric photovoltaic response. As illustrated in BCT-Fe-0.1 ceramics, the distribution of oxygen vacancies inside the ceramics can be modulated by applying external electric fields at high temperatures. To study the influence of the distribution of oxygen vacancies on the photovoltaic response of the BCT-Fe-0.025 ceramics, the ceramics are poled with 1kV/mm at 100^{o}C. The electric field is removed after the ceramic is cooled down for preventing depolarization. The enhancement of the photocurrent responses of BCT-Fe-0.025-O_2 and BCT-Fe-0.025-N_2 cannot be observed. For

the BCT-Fe-0.025-Air, a significant enhancement of photocurrent response is resulted after poling at 100^{o}C. Compared with the ceramic poled at room temperature, the average short-circuit photocurrent of the ceramic is 3 times larger (14.5 nA vs 3.34 nA). It is suggested that the accumulation of oxygen vacancies near the bottom electrodes contributes additional photocurrent that enhances the photocurrent performance of the BCT-Fe-0.025-Air ceramics.

It is proposed that the distribution of oxygen vacancies can be modulated to enhance the ferroelectric photovoltaic response. However, further investigations are still required to study deeper the mechanisms behind the influence of the distribution of oxygen vacancies towards the ferroelectric photovoltaic effect.

Acknowledgements

I would like to express my sincere appreciation to my chief supervisor, Prof. K. W. Kwok for his patience, advice, support and constant encouragement throughout my whole study.

I also need to thank Prof. J. Y. Dai for the photovoltaic measurement and the polishing process to produce thin films from bulk ceramics. Moreover, I gratefully acknowledge the technical support provided by the Materials Research Centre and Clean Room of the Hong Kong Polytechnic University. Without their help, I cannot finish my experiment. I would also like to thank all members of Prof. Kwok's group, especially Dr. Yu Sun, Mr. M.K. Chan and Miss Y. L. Chan for their friendship, help and valuable discussions on my experiments. In addition, I would like to give my sincere thanks to my colleagues in our department, Mr. Chi Man Wong, Mr. Chun Hung Suen, Mr. Man Chung Wong and Mr. Chi Chung Tsoi for their great help and assistance.

Last but not the least, I am deeply indebted to my family for their understanding, constant support and encouragement.

Table of Contents

Certificate of Originality i

Abstract ii

Acknowledgements vi

Table of Contents vii

List of Figures xi

List of Tables xvi

Chapter 1. Introduction 1

1.1. Introduction of ferroelectric material 2

1.1.1. Lead-free perovskite ferroelectric material 6

1.1.2. Barium titanate-based ceramic (BT-based system) 6

1.2. Pyroelectric effect 7

1.3. Photovoltaic effect 8

1.3.1. Ferroelectric photovoltaic effect 9

1.3.1.1. Bulk photovoltaic effect 10

1.3.1.2. Domain wall theory 11

1.3.1.3. Depolarization field model 12

1.3.1.4. Schottky-barrier effect 13

1.4. Abnormal photovoltaic response 14

1.4.1. Influence of oxygen vacancies in photovoltaic response 15

1.5. Motivation of research 19

1.6. Scope of work 20

Chapter 2. Methodology 22

2.1. Sample preparation 22

2.2. Indium Tin Oxide (ITO) and Gold (Au) electrode preparation 23

2.3. Characterization 25

2.3.1. Scanning electron microscope (SEM) 25

2.3.2. Density measurement 27

2.3.3. Crystalline structure 27

2.4. Binding energy and oxygen vacancy concentration 28

2.4.1. X-ray photoelectron spectroscopy (XPS) 28

2.4.2. Oxygen content analysis 29

2.5. Dielectric properties 31

2.5.1. Temperature dependence of dielectric properties 31

2.6. Ferroelectric properties (P-E Loop) 32

2.7. Optical band gap estimation 34

2.8. Photocurrent measurement 36

Chapter 3. BCT-Fe-0.1 and BCT-Fe-0.025 Ceramics Sintered in Different Atmospheres 37

3.1. Introduction 37

3.2. SEM Image of the BCT-Fe-0.1 and BCT-Fe-0.025 ceramics 38

3.3. Crystalline structure 39

3.3.1. XPS analysis (Binding energy) 41

3.3.2. Oxygen vacancies analysis 44

3.4. Dielectric properties 46

3.5. Temperature dependence of dielectric property 47

3.6. Ferroelectric properties 51

3.6.1. P-E Loops of BCT-Fe-0.025 ceramics sintered in different atmospheres 52

3.7. Optical bandgap estimation 54

3.7.1. Tauc's plot of BCT-Fe-0.1 and BCT-Fe-0.025 ceramics sintered in various atmospheres 54

3.8. Conclusions 57

Chapter 4. Photocurrent Response of BCT-Fe-0.1 Non-ferroelectric Ceramics 58

4.1. Introduction 58

4.2. Photocurrent response of the BCT-Fe-0.1 ceramics with the symmet- ric electrode configuration 59

4.3. Controllable photocurrent response of the BCT-Fe-0.1 ceramics with ITO electrodes 63

4.3.1. BCT-Fe-0.1-N_2 ceramics 66

4.3.2. BCT-Fe-0.1-Air ceramics 68

4.3.3. BCT-Fe-0.1-O_2 ceramics 69

4.4. Photocurrent response of the BCT-Fe-0.1 ceramics with symmetric Au electrode configuration..... 72

4.4.1. BCT-Fe-0.1-N_2 ceramics 74

4.4.2. BCT-FE-0.1-O_2 ceramics..... 76

4.4.3. BCT-Fe-0.1-Air ceramics 77

4.5. Conclusions 79

Chapter 5. Photocurrent Response of BCT-Fe-0.025 Ceramics..... 81

5.1. Introduction 81

5.2. Photocurrent response of BCT-Fe-0.0225 ceramics poled at room temperature ……...82

5.3. Photocurrent response of BCT-Fe-0.025 ceramics poled at 100^{o}C..... 87

5.3.1. BCT-Fe-0.025-N_2 ceramics 90

5.3.2. BCT-Fe-0.025-O_2 ceramics 92

5.3.3. BCT-Fe-0.025-Air ceramics 93

5.4. Conclusions 95

Chapter 6. Conclusions..... 97

Reference..... 101

List of Figures

Figure 1.1 The perovskite structure ABO3, shown here for $PbTiO_3$ which has a cubic structure in the paraelectric phase and tetragonal structure in the ferroelectric phase [5] 3

Figure 1.2 Ferroelectric (P-E) hysteresis loop of a typical ferroelectric material [5] 4

Figure 1.3 The domains' arrangement in a polycrystalline ferroelectric material before and after poling [5]. 5

Figure 1.4 Demonstration of pyroelectric effect in ferroelectric material with top and bottom electrodes 8

Figure 1.5 The working mechanism of (a) P-N junction solar cells and (b) Ferroelectric Photovoltaic Devices [3] 9

Figure 1.6 The typical I_{sc} current generated by the ferroelectric photovoltaic device [33] 10

Figure 1.7 Schematics of the device with (a) a perpendicular domain wall and (b) a parallel domain wall. The corresponding photocurrent vs voltage curves for the devices in (a) and (b) are represented in (c) and (d), respectively [2]. 11

Figure 1.8 Schematic diagram of Depolarization field model 13

Figure 1.9 Schematic energy band diagram of ferroelectric photovoltaic devices with a) upward polarization and b) downward polarization state. BE, TE and FE stand for bottom electrode, top electrode and ferroelectric material respectively. The bold dash line represents the energy band in the absence of polarization[13]. 14

Figure 1.10 The abnormal short-circuit photocurrent response of $BiFeO_3$ devices [9]. . 15

Figure 1.11 Schematic energy band diagrams illustrating the variation in Schottky barrier height for an a) upward and b) downward poled samples. I_{drift}, $I_{diffusion}$ and I_{sc} vary with time for a downward poled sample at the moment when the laser is turned c) on and d) off [9]. 17

Figure 1.12 (a)-(c) Schematic energy band diagrams of the upward poled samples. d The I_{sc} response of the upward and downward poled sample with illumination on the top/bottom electrodes [59]. 18

Figure 2.1 Flow chart of sample fabrication. 22

Figure 2.2 Transmission of the ITO and Au electrode..... 25

Figure 2.3 Schematic diagram of the sample after the deposition of top and bottom electrodes..... 25

Figure 2.4 A schematic diagram of SEM [63]. 26

Figure 2.5 The schematic diagram of X-ray diffraction in the crystal [64]. 27

Figure 2.6 An example of XPS O1s spectrum of ceramic oxide [70]..... 30

Figure 2.7 Schematic diagram of the dielectric measurement setup..... 32

Figure 2.8 The schematic diagram of the P-E loop measurement setup 33

Figure 2.9 The top view of the diffuse reflectance measurement setup..... 34

Figure 2.10 An example of Tauc's plot from UV-Vis analysis of a ZnO thin film. The direct band gap is estimated to be 3.35eV [74]. 35

Figure 2.11 Schematic diagram of the setup for photovoltaic measurement. 36

Figure 3.1 SEM micrograph of BCT-Fe-0.025 ceramics sintered in (a) N_2, (b) Air and (C) O_2 and BCT-Fe-0.1 ceramics sintered in (d) N_2, (e) Air and (f) O_2..... 38

Figure 3.2 The XRD patterns of the BCT-Fe-0.1 ceramics in the range of 20^o-80^o. 40

Figure 3.3 (a) The XRD patterns of the BCT-Fe-0.025 ceramics in the range of 20°-80°. (b) The XRD patterns of the BCT-Fe-0.1 and BCT-Fe-0.025 ceramics in the range of 44.5°-46.5°. 40

Figure 3.4 XPS survey spectrum of BCT-Fe-0.1 ceramics 43

Figure 3.5 XPS survey spectrum of BCT-Fe-0.025 ceramics 44

Figure 3.6 High-resolution O1s spectrum of the BCT-Fe-0.1 ceramics in various atmospheres: (a) O_2, (b) air and (c) N_2. 45

Figure 3.7 Temperature dependence of dielectric constant and dielectric loss of BCTFe-0.025-Air ceramics measured at 1 kHz, 10 kHz and 100kHz. 48

Figure 3.8 Temperature dependence of dielectric constant of BCTFe-0.025 ceramics sintered in various atmospheres (O_2, Air and N_2) at 1 kHz. 49

Figure 3.9 Temperature dependence of dielectric constant of BCTFe-0.1 ceramics sintered in various atmospheres (O_2, Air and N_2) at 1 kHz. 50

Figure 3.10 Ferroelectric properties of the BCT-Fe-0.025 and BCT-Fe-0.1 ceramics... 51

Figure 3.11 The P-E Loops of BCT-Fe-0.025 ceramics sintered in O_2, air and N_2. 52

Figure 3.12 Tauc's plot of BCT-Fe-0.1 and BCT-Fe-0.025 ceramics. 55

Figure 4.1 Schematic diagram of a BCT-Fe-0.1 ceramic with oxygen vacancies accumulated near the top electrode. . The orange and blue arrows indicate the direction of the diffusion current and the built-in electric field. 60

Figure 4.2 The short-circuit photocurrent of the BCT-Fe-0.1-N_2, BCT-Fe-0.1-Air and BCT-Fe-0.1-O_2 under periodic AM 1.5G illumination. 62

Figure 4.3 (a) Schematic diagram of the setup used for applying an external electric field. A heater was used to heat the sample to 100°C before applying the external electric field. (b) Schematic diagram predicting the new distribution of oxygen vacancies in a BCT-Fe-

0.1 ceramic after the application of an external electric field and the expected photocurrent under the illumination. The orange and blue arrows indicate the direction of the diffusion current and the built-in electric field respectively. 65

Figure 4.4 The short-circuit photocurrent of the BCT-Fe-0.1-N_2 under periodic AM 1.5G illumination. 66

Figure 4.5 The short-circuit photocurrent of the BCT-Fe-0.1-Air under periodic AM 1.5G illumination. 68

Figure 4.6 The short-circuit photocurrent of the BCT-Fe-0.1-O_2 under periodic AM 1.5G illumination. 70

Figure 4.7 The short-circuit photocurrent of BCT-Fe-0.1-Air ceramics with symmetric ITO and Au electrode under periodic AM 1.5G illumination. 73

Figure 4.8 The short-circuit photocurrent of BCT-Fe-0.1-N_2 ceramics with Au electrodes under periodic AM 1.5G illumination. 74

Figure 4.9 The short-circuit photocurrent of BCT-Fe-0.1-O_2 ceramics with Au electrodes under periodic AM 1.5G illumination. 76

Figure 4.10 The short-circuit photocurrent of BCT-Fe-0.1-Air ceramics with Au electrodes under periodic AM 1.5G illumination. 77

Figure 5.1 The schematic diagram of (a) the downward poling process (positive poling) and (b) the current direction for the ferroelectric photovoltaic process after poling in a positive electric field. 83

Figure 5.2 The short-circuit photocurrent of the as-fabricated, poled (1kV/mm and -1kV/mm) and depoled BCT-Fe-0.025-Air ceramic under AM 1.5G illumination. 85

Figure 5.3 The short-circuit photocurrent of the poled (1kV/mm) BCT-Fe-0.025 ceramics sintered in N_2, Air and O_2. 86

Figure 5.4 (a) The schematic diagram of the downward poling process at 100°C for the BCT-Fe-0.025 ceramic and the resultant distribution of oxygen vacancies. (b) The schematic diagram of the photocurrent generated by the coupling effect of oxygen vacancies and ferroelectric photocurrent effect BCT-Fe-0.025-N_2 ceramics 89

Figure 5.5 The short-circuit photocurrent of the poled BCT-Fe-0.025-N_2 ceramics after poling (1kV/mm) at 100°C. 90

Figure 5.6 The short circuit photocurrent of the as-fabricated, poled at room temperature and 100°C BCT-Fe-0.025-N_2 ceramics. 91

Figure 5.7 The short-circuit photocurrent of the as-fabricated, poled (room temperature and 100°C) BCT-Fe-0.025-O_2 ceramics. 92

Figure 5.8 The short-circuit photocurrent of the as-fabricated, poled at 1 kV/mm (room temperature and 100°C) BCT-Fe-0.025-Air ceramics. 93

List of Tables

Table 2.1 Deposition parameter of ITO and Au electrode 24

Table 3.1 Density of the BCT-Fe-0.025 and BCT-Fe-0.1 ceramics sintered in N2, air and O2 39

Table 3.2 The dielectric constant (ε_r) and dielectric loss (tan δ) of BCT-Fe-0.025 and BCT-Fe-0.1 ceramics sintered in different atmospheres were measured at 1kHz at room temperature 47

Table 3.3 Summary of ferroelectric properties of the BCT-Fe-0.025 ceramics sintered in O_2, Air and N_2 53

Table 3.4 Estimated optical band gaps of BCT-Fe-0.1 and BCT-Fe-0.025 ceramics. ... 56

Chapter 1. Introduction

Since the discovery of the ferroelectric photovoltaic effect in the early 1960s, researchers have shown great interest in studying the mechanism behind the effect [1]–[3]. In contrast to the traditional P-N junction semiconducting materials, the ferroelectric photovoltaic effect originates from the spontaneous polarization of the ferroelectric material [3]–[6]. The different working mechanism gives the ferroelectric photovoltaic effect some unique features, including the above bandgap photovoltage response and even more importantly, the tunable photovoltaic output [2], [3], [7]. The direction of the photocurrent generated by the ferroelectric photovoltaic effect can be switched by changing the direction of the polarization of the ferroelectric material [1], [8], [9].

The working mechanism of the ferroelectric photovoltaic effect is still not fully understood [1], [3], [10]. The mechanism behind the ferroelectric photovoltaic effect is complicated as the photovoltage generated by the effect has been revealed to be dependent on different factors which includes the electrical conductivity of the material, the remnant polarization of the material, the number of domain walls, the distance between the electrodes and the contacts between the ferroelectric and the electrode interfaces [3], [10].

For decades, researchers have proposed different models to explain the ferroelectric photovoltaic effect. The bulk photovoltaic effect, domain wall theory and depolarization field effect are some of the popular models trying to interpret the ferroelectric photovoltaic effect [1], [3], [8]–[11]. Nevertheless, these models fail to completely explain the whole ferroelectric photovoltaic effect [1], [3], [8]–[11].

It is commonly believed that the direction of the photocurrent generated by the ferroelectric photovoltaic devices is always opposite to the direction of the polarization of the devices. However, recent reports have revealed that for some ferroelectric photovoltaic devices, the polarization direction of the devices and the direction of the generated photocurrent can be the same [8], [9], [11]–[15]. These findings make the problem even more complicated. It has been suggested that the defects such as oxygen vacancies inside the material play an important role which leads to such an unusual photovoltaic response [8]–[12], [12]–[16]. This study aims to investigate the role of oxygen vacancies and how they contribute to the photovoltaic response.

This chapter will first give a brief introduction to ferroelectric materials. Then, the working mechanism of the ferroelectric photovoltaic will be discussed and compared with the conventional photovoltaic effect. Next, the abnormal photovoltaic responses in ferroelectric devices and their origins will be studied. Finally, the objectives and motivations of this study will be given.

1.1. Introduction of ferroelectric material

Ferroelectric materials are polar materials which exist with at least 2 equilibrium orientations of the spontaneous polarization without the existence of any external electric field and the orientation of the polarization vector can be switched by an external electric field [3], [15], [17]–[19]. Ferroelectric materials can be classified into 4 different families, the perovskite group, the tungsten-bronze group, the bismuth layer-structure group and the pyrochlores group [5], [20]–[22]. Among them, the perovskites group (ABO_3) is the most widely studied. In the following discussion, lead titanate ($PbTiO_3$) will be used as an example. As demonstrated in Figure 1.1, $PbTiO_3$ has a typical perovskite structure in which the Pb atoms occupy the A sites and the Ti atom occupies the B site and is trapped

in the space of the octahedral oxygen atoms [5]. For the tetragonal ferroelectric phase, as a consequence of the energy minimization, Ti atoms will shift along the centric symmetry axis instead of staying at the geometric centre of the structure [5], [23]. This asymmetrical structure leads to the net dipole moment (spontaneous polarization) in one certain direction [5].

Most ferroelectric materials undergo a structural phase transition from a paraelectric phase (also called a high-temperature non-ferroelectric phase) to a low-temperature ferroelectric phase. The temperature of the phase transition is defined as Curie temperature T_c [11], [21], [24]. When the material is heated to a temperature above the Curie temperature, it will undergo a phase transition from the ferroelectric phase to the paraelectric phase [5]. As shown in Figure 1.1, in the case of $PbTiO_3$, it will switch to a cubic paraelectric phase and the Ti atom will stay at the geometric centre of the structure [21], [24]. As a result, the crystal structure will become symmetric and the $PbTiO_3$ material lose the net polarization and the ferroelectric properties.

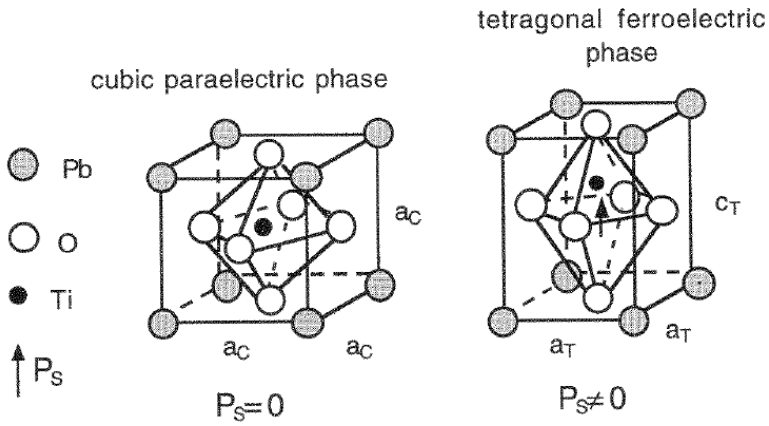

Figure 1.1 The perovskite structure ABO3, shown here for $PbTiO_3$ which has a cubic structure in the paraelectric phase and tetragonal structure in the ferroelectric phase [5].

The ferroelectric properties of ferroelectric materials can be described by a ferroelectric (P-E) hysteresis loop. Figure 1.2 shows a P-E hysteresis loop of typical ferroelectric material. At point A, the ferroelectric material is initially in a non-polar state and the domains are randomly arranged. As a result, the net polarization of the material in this stage is zero [5], [25]. After the introduction of a strong electric field, the domains are aligned coercively and a non-linear polarization response will have resulted (Point A to Point C) [5], [25]. When the electric field is decreased back to zero or removed, the polarization of the material does not decrease to zero (point E); a further reversed electric field is needed to bring the ferroelectric material back to the zero-polarization state (point F) [5], [25]. The polarization at zero electric field is known as the remnant polarization (P_r) and the electric field which is required to bring the polarization back to zero is identified as the coercive field (E_c) [5], [25]. When the reversed electric field is further increased, the material reaches another polarization state (point F) in which the polarization direction is opposite to that at point D [5], [25].

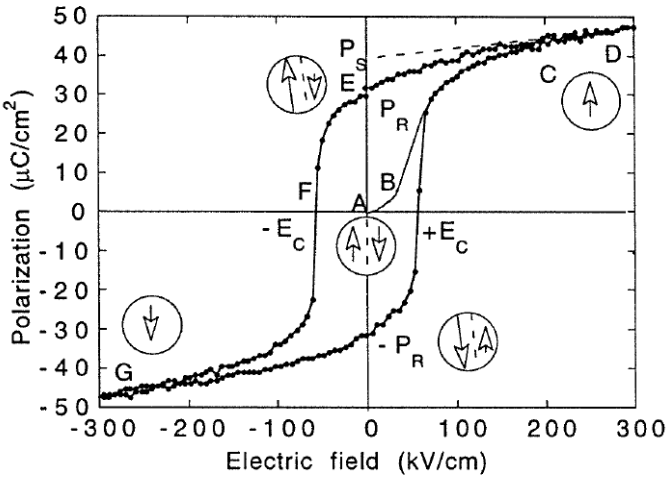

Figure 1.2 Ferroelectric (P-E) hysteresis loop of a typical ferroelectric material [5].

As mentioned, the domains of an as-fabricated ferroelectric material are usually randomly oriented with a zero net polarization. The alignment of the domains can be controlled by applying a high external electric field which is called poling [5], [25]. After poling, the domains will be aligned and a net remnant polarization is produced [5], [25]. A schematic diagram of the arrangement of domains in a ferroelectric material is illustrated in Figure 1.3.

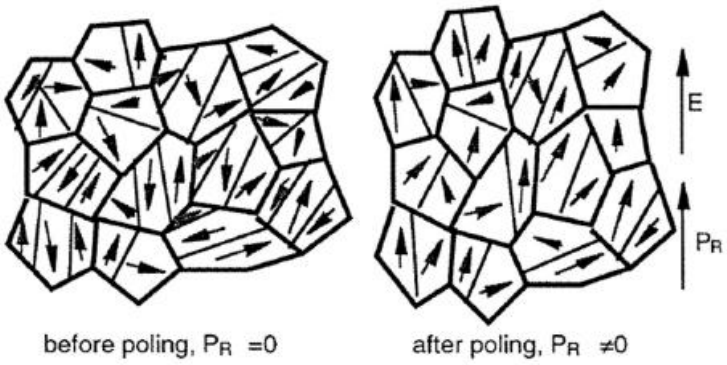

Figure 1.3 The domains' arrangement in a polycrystalline ferroelectric material before and after poling [5].

1.1.1. Lead-free perovskite ferroelectric material

Lead-based ferroelectric ceramics such as $Pb(Mg_{1/3}Nb_{2/3})O_3$–$PbTiO_3$ (PMN-PT) and $Pb(Zr_{1-x}Ti_x)O_3$ (PZT) have been widely used for various piezoelectric and dielectric applications [26]. The lead-based ferroelectric materials have occupied the industry in the past two decades due to their higher Curie temperature and larger piezoelectric coefficients. However, lead is toxic to the environment and the human body. Developments of lead-free ferroelectric materials are required to substitute lead-based materials [26].

The lead-free perovskite structure ferroelectric ceramics can be classified into 3 families: $K_{0.5}Na_{0.5}NbO_3$ (KNN system), $BaTiO_3$ (BT system) and $Na_{0.5}Bi_{0.5}TiO_3$ (BNT system). Among them, the ceramics in KNN and BNT system exhibits relatively high curie temperature (T_C exceeds 300^{o}C) and large remnant polarization (P_r ~33μC/cm^2) [26]–[28]. However, ceramics of BNT and KNN-based systems always contain volatile elements. A predesigned stoichiometric ratio may not be maintained during the high-temperature fabrication process. Different from the BNT and KNN -based system ceramics, the BT system ceramics do not contain volatile elements and the predesigned stoichiometric ratio will be maintained during the fabrication process [26].

1.1.2. Barium titanate-based ceramic (BT-based system)

$BaTiO_3$ (BTO) is one of the earliest lead-free ferroelectric materials which has a high dielectric constant (d33~190pC/N) and piezoelectric constant. BT-based ferroelectric ceramics have a relatively low Curie temperature (T_c~120^{o}C). When the temperature of the BTO is below 120^{o}C, the BTO is in the tetragonal ferroelectric phase and the spontaneous polarization is along the [001] direction. If the temperature of the BTO exceeds 120^{o}C, it

will undergo a phase transformation to the cubic phase (paraelectric phase) and spontaneous polarization does not exist at this phase. The relatively low Curie temperature of the BT-based ferroelectric materials limited their practical applications.

BT-based ceramics receive considerable attention in research due to their easy doping with other chemicals. However, the tetragonal phase of the BTO may be affected due to transition metal doping. For example, it is reported that the increase in Fe doping content in BTO will lead to the development of the hexagonal phase [29]. The ferroelectric and dielectric properties of the BT-based material may be affected. Research shows the possibility of the formation of the unwanted hexagonal phase by doping Ca into BTO [27], [28]. In $Ba_{0.9}Ca_{0.1}TiO_3$ (BCT) ceramics, Ca act as a reduction inhibitor to prevent the formation of the hexagonal phase [28]. Therefore, BCT ceramic is chosen as the base material in the study.

1.2. Pyroelectric effect

The pyroelectric effect is defined as a phenomenon in which a material releases electric charges due to a change in temperature [5], [7], [10], [30]. This effect can be observed in a poled ferroelectric material.

Figure 1.4 demonstrates the mechanism of the pyroelectric effect of a poled ferroelectric material with top and bottom electrodes. It is suggested that the remnant polarization of the ferroelectric material is sensitive to temperature [7], [10]. If the temperature of the material suddenly changes, the oscillation state of the electric dipole will be disturbed and the polarization of the material is affected [10]. As shown in Figure 1.4, charges are induced at the electrodes due to the aligned spontaneous polarization. When

the temperature of the material increases, the electric dipoles oscillate with a higher degree and the average polarization decreases [7], [10]. In consequence, the induced charges are reduced, causing a flow of current from the bottom electrode to the top electrode. In contrast, when the temperature of the material decreases, a reverse induced current (flow from the top to bottom electrode) is resulted [7].

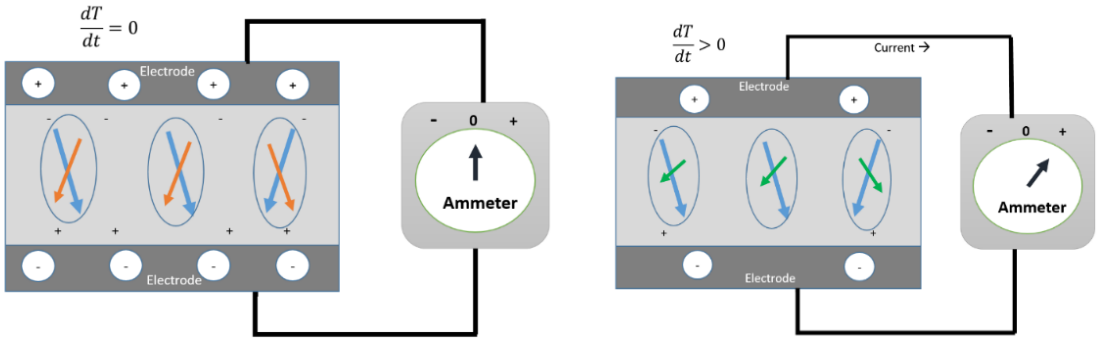

Figure 1.4 Demonstration of pyroelectric effect in ferroelectric material with top and bottom electrodes.

1.3. Photovoltaic effect

The photovoltaic effect refers to a process that generates electricity by converting the incident photons into flowing free charge carriers [8]–[10], [31]. Since the photovoltaic effect involves converting light energy into electrical energy, it can be applied for solar energy harvesting and is considered as one of the renewable energy sources [8]–[11], [13], [31], [32]. The p-n junction semiconductor solar cells have dominated the solar cell industry for decades. The working mechanism of a p-n junction solar cell is shown in Figure 1.5. When light with sufficient energy illuminates the p-n junction solar cell, electrons

from the valence band will be excited to the conduction band, creating a number of electron-hole pairs [3], [10]. The free electrons will move to the n-type side while the holes go to the p-type side of the devices [3], [10]. The accumulated holes and electrons on opposite sides will generate a potential difference known as photovoltage [3], [10].

Compared with the photovoltaic effect generated by the traditional p-n junction solar cell, the ferroelectric photovoltaic effect has some fascinating characteristics including the above bandgap photovoltage and the switchable photocurrent [2], [3], [9]. However, the working principle of ferroelectric photovoltaic effect is still a mystery [3]. The possible working mechanism will be discussed in the following sections.

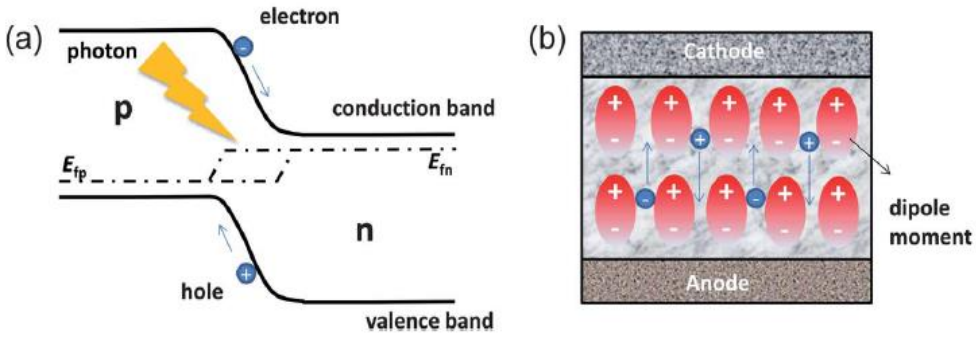

Figure 1.5 The working mechanism of (a) P-N junction solar cells and (b) Ferroelectric Photovoltaic Devices [3].

1.3.1. Ferroelectric photovoltaic effect

Before considering the ferroelectric photovoltaic effect, the pyroelectric response in ferroelectric photovoltaic devices should be considered. Under illumination, the device is heated and the net polarization of the material will decrease. As a result, the induced charges in the electrodes are reduced. resulting in a net flow current flow [10], [31], [33].

After the light is switched off, the sudden decrease in temperature will generate an opposite pyroelectric current.

Figure 1.6 shows a typical I_{sc} current generated by a ferroelectric photovoltaic device. The sharp current peaks are identified as the transient pyroelectric current while the steady photovoltaic current is the current originated by the ferroelectric photovoltaic effect [10], [31], [33].

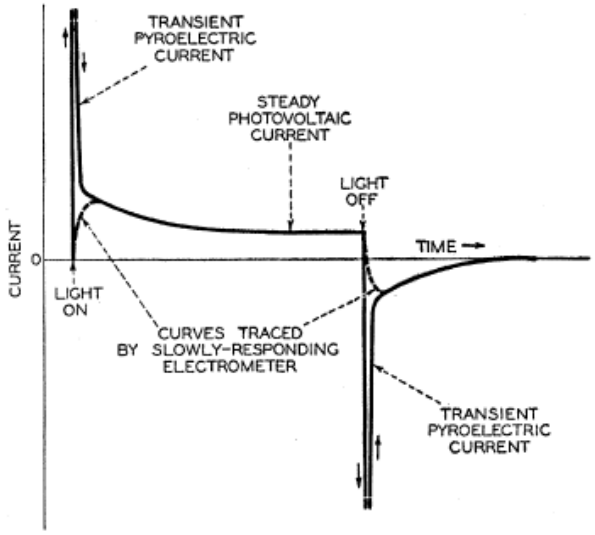

Figure 1.6 The typical I_{sc} current generated by the ferroelectric photovoltaic device [33].

The mechanism of the ferroelectric photovoltaic effect is still not fully understood. Serval theories have been proposed for explaining the ferroelectric photovoltaic effect. The Bulk photovoltaic effect, domain wall theory and the depolarization field model are some of the common models, which will be discussed in the next section.

1.3.1.1. Bulk photovoltaic effect

According to the bulk photovoltaic effect, ferroelectric materials work as a current source. In this theory, the steady photocurrent formation is related to the non-centrosym-

metric nature of the ferroelectric crystal [3], [21]. In the crystal, due to the non-centro-symmetric nature, the probability of the excited electrons jumping from a k momentum state to a k' state and the probability for the reverse process can be different [24], [34]–[36]. Therefore, an asymmetric momentum distribution of the photo-generated charge carriers is resulted, causing a steady photocurrent.

1.3.1.2. Domain wall theory

Domain wall theory was proposed by Yang *et al* [2], [3], [13], [37]. They studied the photovoltaic response on the $BiFeO_3$ (BFO) film with ordered domain strips [2], [3]. They found that the photovoltage in the BFO film is larger than the bandgap of the material and can be increased linearly with the number of domain walls as shown in Figure 1.7.

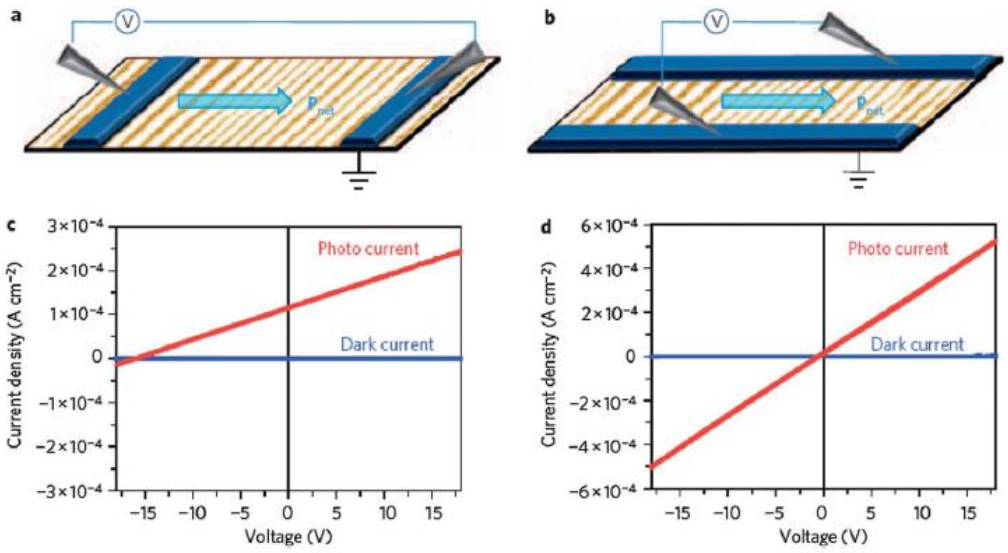

Figure 1.7 Schematics of the device with (a) a perpendicular domain wall and (b) a parallel domain wall. The corresponding photocurrent vs voltage curves for the devices in (a) and (b) are represented in (c) and (d), respectively [2].

To explain these interesting phenomena, Yang *et al* [2] suggested that each narrow domain wall of the ferroelectric material contributes a specific amount of photovoltage. This proposed mechanism is similar to the case of putting a large number of solar cells in series and, as a result, an ultra-high photovoltage which exceeds the band gap of the material can be generated [2]. Domain wall theory works ideally for bulk ferroelectric materials and successfully explains the ultra-high photovoltage phenomenon [3]. However, it fails to explain the photovoltage effect in thin-film ferroelectric devices. Therefore, the depolarization field model has been introduced [2], [3], [13], [37].

1.3.1.3. Depolarization field model

The depolarization field theory is commonly used to explain the ferroelectric photovoltaic effect in thin-film devices [3]–[5], [38]–[40]. A schematic diagram of the ferroelectric photovoltaic effect in thin-film devices is illustrated in Figure 1.8. When the ferroelectric thin film is brought in contact with the metal electrodes, the surface charges caused by the spontaneous polarizations of the ferroelectric material will be imperfectly screened by the free charges in the metals [3]. Therefore, an internal electric field will be built up by those unscreened charges. This electric field is known as the depolarization field [3]. It is noticed that the direction of the depolarization field is opposite to the polarization direction of the ferroelectric thin film [3], [4]. This depolarization field can act as a driving force for the electron-hole separation when the ferroelectric thin film is stimulated by photons [3]. In thin-film scale, it is believed that the depolarization field effect plays an important role in the photovoltaic response of the thin-film devices.

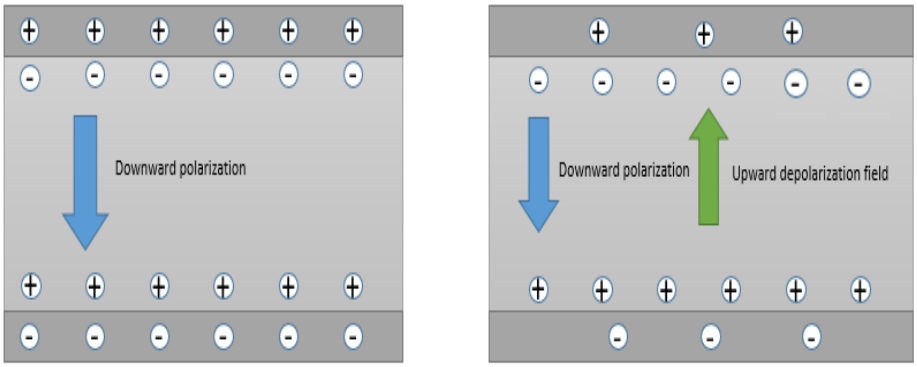

Figure 1.8 Schematic diagram of Depolarization field model.

1.3.1.4. Schottky-barrier effect

In ferroelectric photovoltaic devices, the contacts between the ferroelectric material and the metal electrodes also affect their photovoltaic responses/performances [3], [13], [41]–[43]. When materials with different work functions are in contact, an energy barrier will be formed at the interface which results in a local electric field. Some researchers suggested that such a local electric field caused by the Schottky-barrier effect can be cancelled by choosing symmetrical electrodes for their ferroelectric photovoltaic devices [3]. Moreover, they also suggested that the Schottky barrier effect is independent of the polarization of the ferroelectric material [3]. However, other researchers argued that the height of the Schottky barrier at the interface can be modulated by the spontaneous polarization of the ferroelectric material [13], [41]–[45].

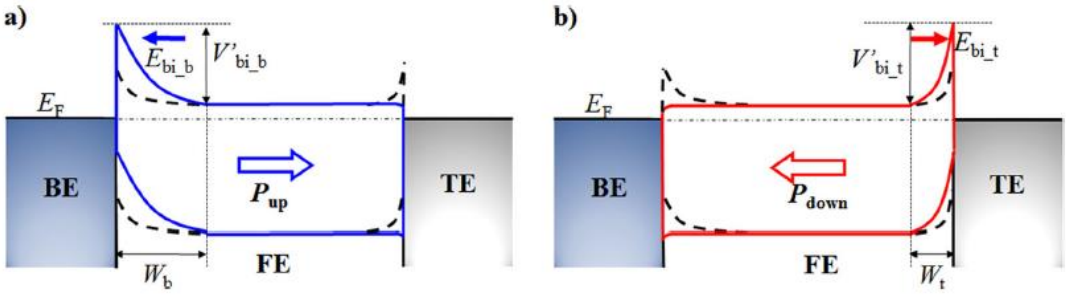

Figure 1.9 Schematic energy band diagram of ferroelectric photovoltaic devices with a) upward polarization and b) downward polarization state. BE, TE and FE stand for bottom electrode, top electrode and ferroelectric material respectively. The bold dash line represents the energy band in the absence of polarization [13].

As illustrated in Figure 1.9, for the case of an upward polarization state, positive bounded charges are accumulated at the interface between the top electrode and the ferroelectric material which will lower the energy barrier [13], [43]. In contrast, the negative bounded electrons near the bottom electrode will increase the barrier height [13], [43]. As a result, a built-in electric field is created in the devices[41], [43], [44]. Figure 1.9b illustrates the schematic energy band diagram of the ferroelectric photovoltaic device in a downward polarization state [13], [43].

The built-in electric field in the depletion region provides the driving force for separating the photo-induced electrons [42]–[45]. As a result, a polarization-dependent photovoltaic response is observed.

1.4. Abnormal photovoltaic response

The built-in electric field in the depletion region provides the driving force for separating the photo-induced electrons [42]–[45]. As a result, a polarization-dependent photovoltaic response is observed. As mentioned, one of the characteristics of the ferroelectric

photovoltaic effect is the polarization-dependent photocurrent. It is well believed that the direction of the generated photocurrent is always opposite to the polarization of the devices [2], [3], [7], [10], [22], [46]. However, a few reports are showing different findings. Bai et al. have revealed that the direction of the generated photocurrent can be the same as the polarization direction of the material as shown in Figure 1.10 [9]. Other researchers have also reported similar results [14], [47]–[50]. They proposed that chemical defects such as oxygen vacancies inside the material lead to such an abnormal photovoltaic response [10], [11], [14], [15], [18], [51]. The proposed mechanism will be discussed in the following sections.

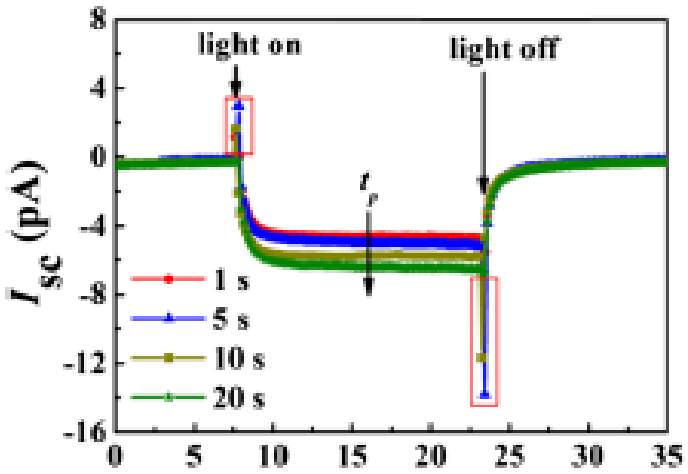

Figure 1.10 The abnormal short-circuit photocurrent response of $BiFeO_3$ devices [9].

1.4.1. Influence of oxygen vacancies in photovoltaic response

The existence of defects such as oxygen vacancies cannot be prevented during the fabrication process of ceramic oxides [15], [51]–[56]. As mentioned in the previous section, researchers believed that chemical defects such as oxygen vacancies inside the material also contribute to the photovoltaic response of the devices [12], [14], [15], [18],

[57], [58]. They suggested that the uneven distribution of oxygen vacancies in the material plays a main role as the accumulation of oxygen vacancies near the electrode-ceramic interface will reduce the barrier height at the interface [14], [48], [57], [59]. As a result, a Schottky-like barrier is formed, which contributes a build-in field for separating the photo-generated electron-holes pairs [14], [36], [59]. In addition, oxygen vacancies can trap the photo-induced electrons while the photo-induced holes can act as external diffusion carriers and result in a diffusion current [14], [36], [59]. Figure 1.11a and b show the schematic energy diagrams for a $BiFeO_3$ photovoltaic device with an upward poled and downward poled sample, respectively. In general, the photocurrent (short-circuited current I_{sc}) is contributed by the diffusion current ($I_{diffusion}$) and the drift current (I_{drift}) [14], [36], [59]. Figure 1.11a demonstrates that for the upward poled sample, the direction of I_{sc} is opposite to the polarization direction of the material which agrees with the expectation of a typical ferroelectric photovoltaic response. However, for the downward poled sample, as presented in Figure 1.11c, the direction of I_{sc} is the same as the polarization direction of the material [14]. Bai et al. explained this phenomenon by taking into account the contribution of oxygen vacancies inside the material [14]. As shown in Figure 1.11c, when the downward poled sample is illuminated, the diffusion current is greater than the drift current; as a result, a net I_{sc} with the same direction of the polarization has resulted.

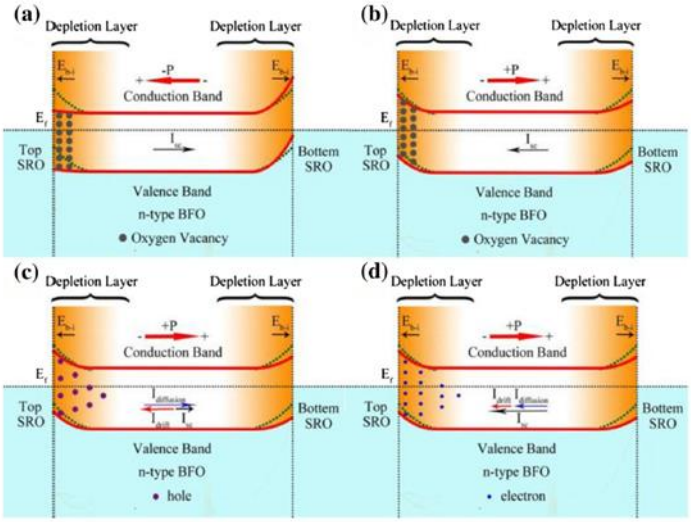

Figure 1.11 Schematic energy band diagrams illustrating the variation in Schottky barrier height for an a) upward and b) downward poled samples. I_{drift}, $I_{diffusion}$ and I_{sc} vary with time for a downward poled sample at the moment when the laser is turned c) on and d) off [9].

Yi et al. also showed the influence of oxygen vacancies on the photovoltaic response in ferroelectric photovoltaic devices [10]. They fabricated a ferroelectric photovoltaic device with BFO and a pair of symmetric Au electrodes. The schematic diagram of the device is shown in Figure 1.12d. It was expected that the magnitude of the photocurrent of the device was the same when the light was shone on the top or bottom electrode. But it turned out that for their device, a much larger photocurrent was generated when the light was shone on the top electrode [10]. They explained that the phenomenon was the result of the accumulation of oxygen vacancies near the illuminated electrode [10]. As demonstrated in Figure 1.12c, in the case of bottom surface illumination, I_{sc} was nearly zero [10]. They explained that due to the absence of oxygen vacancies near the bottom electrode, a relatively small $I_{diffusion}$ was cancelled out by the I_{drift} [10]. Moreover, Figure 1.12d shows that the photocurrent generated by the upward poled and downward poled

devices differ by more than ten times [10]. It supports that oxygen vacancies inside the material can contribute to or enhance the photovoltaic response of the devices [10].

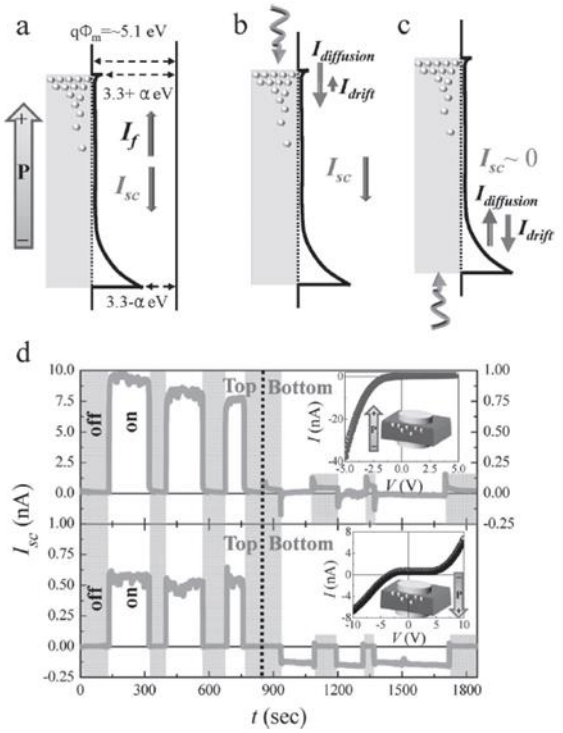

Figure 1.12 (a)-(c) Schematic energy band diagrams of the upward poled samples. d The I_{sc} response of the upward and downward poled sample with illumination on the top/bottom electrodes [59].

The oxygen vacancy content of the ceramic can be controlled by the synthesis process, such as the sintering time and sintering atmospheric [47], [49], [51]–[53]. For example, if the sample is sintered in an atmosphere with a lower oxygen partial pressure, the oxygen vacancy concentration will be higher. In contrast, ceramics with a lower oxygen vacancies concentration can be produced by sintering with a higher oxygen partial pressure. In addition, serval researchers have reported that an external electric field to the device can lead to the migration of the oxygen vacancies within the material [9], [15], [16], [19]. As a result, the distribution of the oxygen vacancies inside the material can be

changed and it will affect the photovoltaic response or performance of the devices [15], [59]. These characteristics provide a chance to tailor-make a material with different oxygen distributions and concentrations, and then optimize the performance of the photovoltaic devices [15], [59].

1.5. Motivation of research

It is well believed that the direction of the photocurrent generated by the ferroelectric photovoltaic effect is always opposite to the polarization direction of the material. However, some recent reports have shown that the photocurrent and the polarization in ferroelectric photovoltaic devices can have the same direction. It has also been shown that defects such as oxygen vacancies inside the material lead to such an unusual photovoltaic response. As defects (such as oxygen vacancies) can contribute to the photovoltaic response, it is worth studying how the oxygen vacancies affect the photovoltaic response. In addition, it has been shown that the oxygen vacancy content inside the oxide ceramic can be controlled by the fabrication process. For example, by controlling the sintering time and sintering atmosphere, the oxygen vacancy profile in the ceramic can be modified. It provides an opportunity to enhance the photovoltaic performance of the material by controlling the oxygen vacancy profile of the material.

It has been reported that the ferroelectric photovoltaic effect can be observed in $BaTiO_3$ (BTO) ceramics [10]. Moreover, through doping Ca^{2+} to BTO, the possibility of the formation of the unwanted hexagonal phase in the ceramic will be reduced [28]. As a result, the tetragonal phase of the Ca doped BTO will become more stable. Therefore, in this work, barium titanate–based ferroelectrics ceramic $Ba_{0.9}Ca_{0.1}TiO_3$ (BCT) has been chosen as the base material. Researchers also suggested that acceptor doping will promote the formation of oxygen vacancies in BCT ceramic [60]. Fe^{3+} and Ti^{4+} share similar ionic

radii and it is believed that the tolerance factor may not change significantly if the doping level of $Fe^{3+}$is low [61]. Moreover, researches also show that the optical bandgap of the BTO ceramics is reduced after doping of Fe^{3+} [62]. The photovoltaic response of the BCT ceramic may enhance after doping Fe^{3+} [62]. Therefore, Fe^{3+} has been chosen as a dopant for the BCT ceramic. 0.025 mol and 0.1 mol Fe^{3+} is doped in BCT ceramic to fabricate $Ba_{0.9}Ca_{0.1}Ti_{0.975}Fe_{0.025}O_3$ (BCT-Fe-0.025) and $Ba_{0.9}Ca_{0.1}Ti_{0.9}Fe_{0.1}O_3$ (BCT-Fe-0.1) ceramics. The BCT-Fe-0.1 and BCT-Fe-0.025 ceramics will be sintered in different atmospheres (Air, N_2 and O_2). It is suggested that the oxygen vacancies content of the ceramics is highly related to the sintering atmosphere. This study will focus on the influence of oxygen vacancies on the photovoltaic response of the BCT-Fe-0.1 and BCT-Fe-0.025 ceramics.

1.6. Scope of work

The main objectives of this work are to demonstrate the photovoltaic effect of BCT-Fe-0.1 and BCT-Fe-0.025 ceramics and study the relationship between the sintering atmosphere and the photovoltaic response of the ceramics. The thesis consists of six chapters:

Chapter 1 briefly introduces the background of ferroelectricity and corresponding materials. In this chapter, the photovoltaic mechanisms in both semiconductor and ferroelectric materials are reviewed. In addition, the influence of oxygen vacancies on the photovoltaic performance in ferroelectric devices is also discussed. It also gives possible pathways to control the oxygen vacancies content inside the ceramic oxides. In the final part of this chapter, the motivation and objectives of the present work are given.

Chapter 2 introduces the fabrication process of the Fe-doped BCT ceramics. It also provides the characterization and techniques for crystal structure, grain size and oxygen vacancy content inside the perovskite oxide. In addition, the equipment setup for the dielectric, ferroelectric properties, optical properties and photovoltaic measurements are given in this chapter.

Chapter 3 gives the grain size, optical bandgap, oxygen vacancy concentration, dielectric and ferroelectric properties of the Fe doped BCT-Ceramics. The studies of the relationship between the sintering atmosphere, grain size, dielectric properties and ferroelectric properties are also presented in this chapter.

Chapter 4 examines the photocurrent response of non-ferroelectric BCT-Fe-0.1ceramics. Two different types of electrodes (ITO and Au) are used for studying the relation between the sintering atmosphere and the photovoltaic response of BCT-Fe-0.1 ceramics.

Chapter 5 demonstrates the ferroelectric photovoltaic effect of BCT-Fe-0.025 ceramics. The BCT-Fe-0.025 ceramics are sintered in different atmospheres and their photovoltaic responses are compared. In addition, poling field is applied to the ceramic at different temperatures and then demonstrates the change in the photovoltaic response of the ceramic samples.

Chapter 6 gives the conclusion of the work.

Chapter 2. Methodology

2.1. Sample preparation

The $Ba_{0.9}Ca_{0.1}Ti_{0.9}Fe_{0.1}$ (BCT-Fe-0.1) and $Ba_{0.9}Ca_{0.1}Ti_{0.975}Fe_{0.025}$ (BCT-Fe-0.025) ceramics were prepared by a conventional solid-state reaction. High purity $BaCO_3$, CaCO3, TiO_2 and Fe_2O_3 (International laboratory USA) were used in the fabrication process. The powders in the stoichiometric ratio were ball-milled in ethanol using zirconia balls for 10 hours. Then the well-mixed powders were calcined at 1000^{o}C for 4 hours. The calcined powders were then ball-milled again for 10 hours. Then the powders were mixed thoroughly with 5-wt% polyvinyl alcohol (PVA) binder solution and pressed into disk samples with 12 mm diameter and 0.5 mm thickness. After that, the binder in the samples was completely burned out at 650^{o}C for 2 hours. Finally, the samples were sintered at 1350^{o}C-1410^{o}C for 4 hours in pure oxygen, air or pure nitrogen for densification.

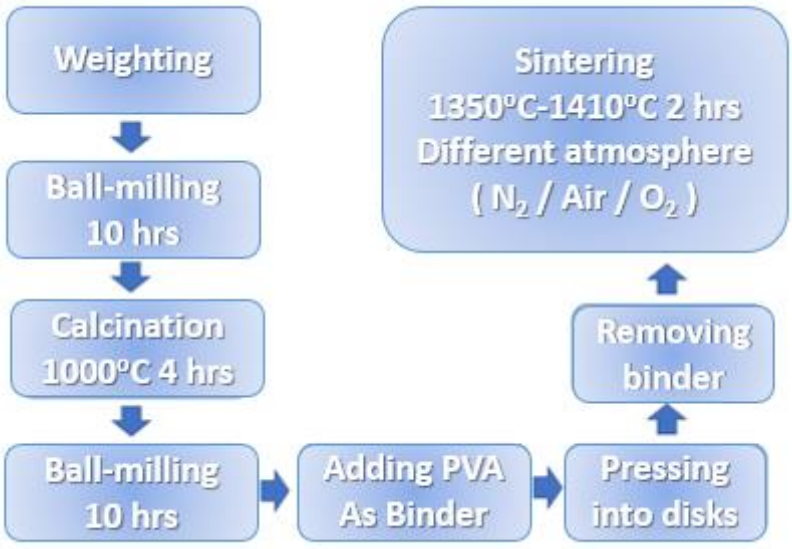

Figure 2.1 Flow chart of sample fabrication.

2.2. Indium Tin Oxide (ITO) and Gold (Au) electrode preparation

For conducting the photocurrent measurement, transparent indium tin oxide (ITO) electrodes were deposited on the surfaces of the ceramic samples. The thick ceramic samples were first attached to a glass substrate. Then, the thick ceramic samples were thinned down to 100 μm by polishing with sandpapers. An ITO electrode was introduced on the polished surface by RF magnetron sputtering as a bottom electrode. After that, the sample was attached to a gold (Au) coated substrate using silver paste. The other surface of the samples was deposited with ITO as a top electrode. The diameter of the top electrode is 8 mm.

For studying the relationship between the photovoltaic response of the samples and the electrodes, a 40 nm thick Au electrode was used to replace the bottom ITO electrode of some samples. The Au electrode was deposited by DC magnetron sputtering.

The deposition parameters of the ITO and Au electrodes are summarized in Table 1. Figure 2.2 shows the transmittance of the ITO electrode deposited by the parameters shown in Table 1. Figure 2.3 shows a schematic diagram of the sample with the top and bottom electrodes.

Table 2.1 Deposition parameter of ITO and Au electrode

	ITO	AU
Type of sputtering	RF magnetron sputtering	DC magnetron sputtering
Sample Temperature	200°C	Room Temperature
Power	70W	60W
Gas flow	Ar : O2 (60:1)	Ar
Pressure	5 mTorr	7.5 mTorr
Deposition time	40 min	45 sec
Annealing (Time/Temperature)	1hr/200°C	N/A

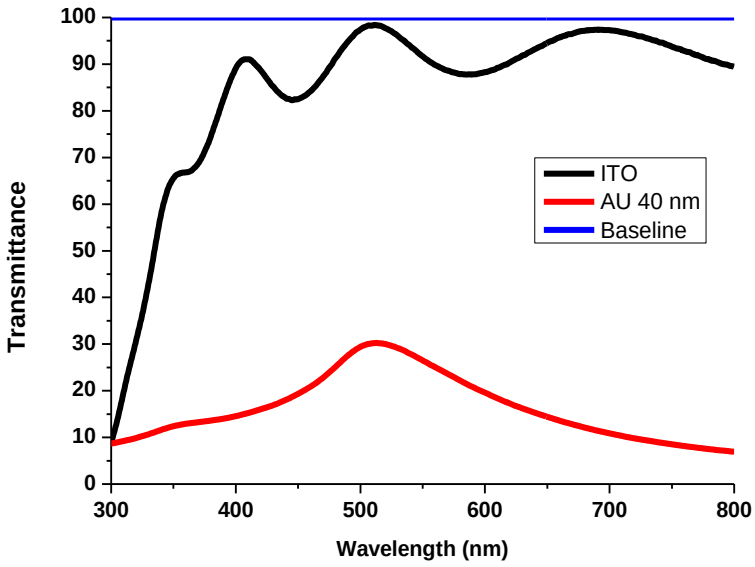

Figure 2.2 Transmission of the ITO and Au electrode.

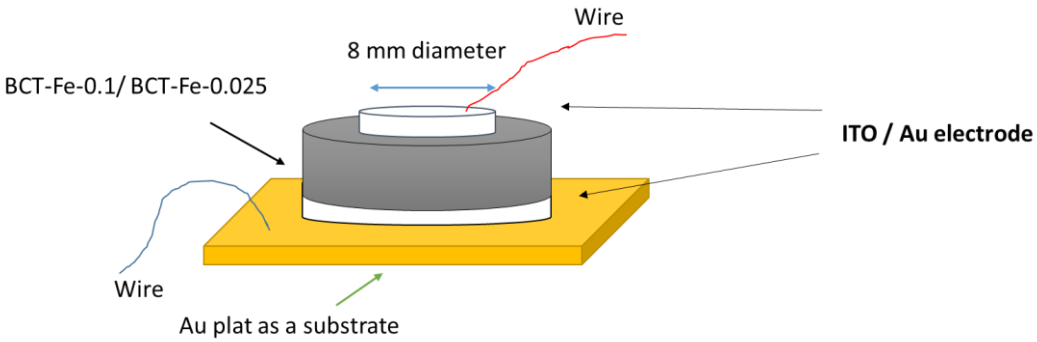

Figure 2.3 Schematic diagram of the sample after the deposition of top and bottom electrodes.

2.3. Characterization

2.3.1. Scanning electron microscope (SEM)

A scanning electron microscope (SEM) is a type of electron microscope which produces images by scanning the surface of the sample with a high energy beam of electrons.

A typical SEM consists of 5 main components which include an electron gun, an electro-magnetic lens system, electrons detectors, a sample chamber and a display unit. Figure 2.4 shows a schematic diagram of SEM [63].

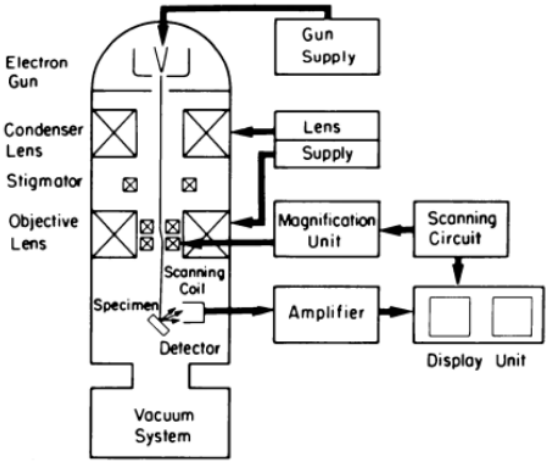

Figure 2.4 A schematic diagram of SEM [63].

During the operation process, a high energy focused electron beam is generated by the electron gun and the electromagnetic lens system. The electrons of the focused beam will interact with the sample. The above interaction will produce secondary electrons (SE), backscattered electrons (BE), auger electrons and characteristics X-rays, all of which are collected by the respective detectors [63]. The received signals are then converted into images and displayed on the display unit.

In this study, a 10 nm think gold thin layer was deposited on the as-sintered ceramic through sputtering. SEM (JEOL Model JSM-6490) was used for the topography analysis.

2.3.2. Density measurement

The density of the ceramic was determined using Archimedes' principle. The mass (m_{air}) of the sample was first measured in air. After that, the sample was immersed into water. The apparent mass (m_{water}) of the sample when submerged was then measured. The density of the sample was calculated by the following equation:

$$\rho = \frac{\rho_{water} m_{air}}{m_{air} - m_{water}} \quad (2.1)$$

where $\boldsymbol{\rho}$ is the density of the sample and $\boldsymbol{\rho}_{water}$ is the density of water which is equal to 1g/ml.

2.3.3. Crystalline structure

The crystalline structure of the ceramic oxides can be examined by X-ray diffraction. X-ray diffraction (XRD) is a non-destructive technique to study the crystalline structure of materials. An XRD pattern will be produced from the interaction of the X-ray and the crystal lattice. By analysing the XRD patterns, the crystalline structure of the samples can be determined.

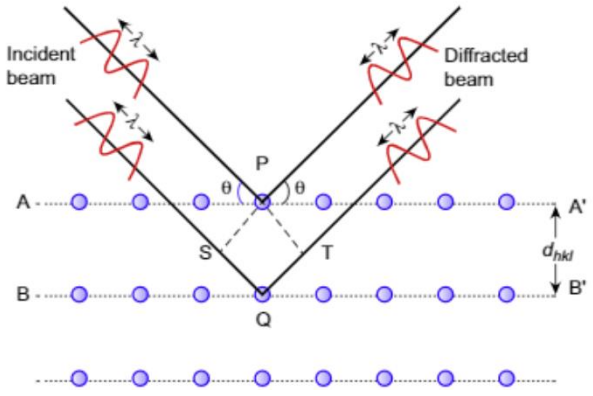

Figure 2.5 The schematic diagram of X-ray diffraction in the crystal [64].

As shown in Figure 2.5, during the operation, an X-ray beam is incident on the sample surface with an angle θ_{hkl}. The scattered X-rays from different crystalline planes will interfere with each other and produce a variation of intensity with different angles which is identified as an XRD pattern [64]. The XRD pattern follows the Bragg's law, where the local maxima of the intensity of the detected X-ray occur if the incident angle of the X-ray satisfies the following condition:

$$2d_{hkl}\sin\theta_{hkl} = n\lambda \tag{2.2}$$

where λ is the wavelength of the X-ray, n is the order of diffraction, h, k and l are the Miller indices, d_{hkl} is the interplanar spacing of {hkl} set of lattice planes, and θ_{hkl} is the incident angle [64].

In this work, an XRD analysis equipment with CuKα (wavelength of the incident ray λ = 0.154 nm) radiation (SmartLab; Rigaku Co., Japan) was used to examine the crystalline structure of the ceramics.

2.4. Binding energy and oxygen vacancy concentration

2.4.1. X-ray photoelectron spectroscopy (XPS)

The elements and oxygen vacancy information can be obtained through the X-ray photoelectron spectroscopy technique. X-ray photoelectron spectroscopy (XPS) is a surface spectroscopic technique which belongs to the photoemission spectroscopy family [14], [51], [65]–[68]. The working principle of this technique is based on the photoelectric effect. During the characterization process, the sample is irradiated by a focused X-ray beam, the excited electrons are then collected and an electron population spectrum will be obtained. The elements that exist in the sample can then be identified. Furthermore,

apart from identifying the elements in the material, XPS allows researchers to get information about the electronic structure and chemical states of the elements in the material.

The electron binding energy of the emitted electrons can be determined by the photoelectric effect equation:

$$E_{binding} = E_{photon} - (E_{kinetic} + \phi) \quad (2.3)$$

where $E_{binding}$, E_{photon} and $E_{kinetic}$ are the binding energy of the electron, the energy of the X-ray photons being used and the kinetic energy of the electron measured by the instrument, respectively. Φ refers to the work function of the specific material.

2.4.2. Oxygen content analysis

The information on the oxygen content inside the samples can be obtained by analysing the O1s spectra.

It has been reported that the O1s spectrum can be fitted into 3 different curves [14], [66], [68]–[70]. The first one is the low energy curve (O1s I) which is related to the oxygen atoms bonded to the cations that are in the stoichiometric oxidation state [66], [69], [70]. The second one is the medium curve (O1s II) which is attributed to O^{-2} ions bonded to non-stoichiometric oxidation states [66], [70]. If oxygen vacancies are present in the material, cations will have oxidation states less than that of the formula to maintain the charge balance in the structure of the material [54], [69], [70]. Therefore, the information on the oxygen vacancies of the sample can be obtained by detecting the signal from the O^{-2} ions.

Finally, the high energy curve (O1s III) represents the loosely bound oxygen atoms on the surface of the sample [69], [70]. These oxygen atoms are usually found in H_2O and OH groups from the atmosphere and not from bonding with the atoms in the sample. In

other words, these signals are not the signals from the sample[54], [69], [70]. Therefore, XPS measurements are always conducted under a high vacuum to reduce or eliminate this type of signal [65].

The number of oxygen vacancies inside the sample can be roughly estimated by calculating the relative peak area ratio of the middle energy curve and the low energy curve (O1s II / O1s I) [14], [54], [69]–[71]. A higher relative peak area ratio of the two curves means that the sample contains more oxygen vacancies [14], [54], [69]–[71].

Figure 2.6 shows an O1s XPS spectrum of a $Ba_{0.85}Ca_{0.15}Zr_{0.1}Ti_{0.9}O_3$(BCZT) pellet as an example. It has been shown that the corresponding O1s XPS spectrum can be fitted into 3 curves. (O1s I, O1s II and O1s III) [70].

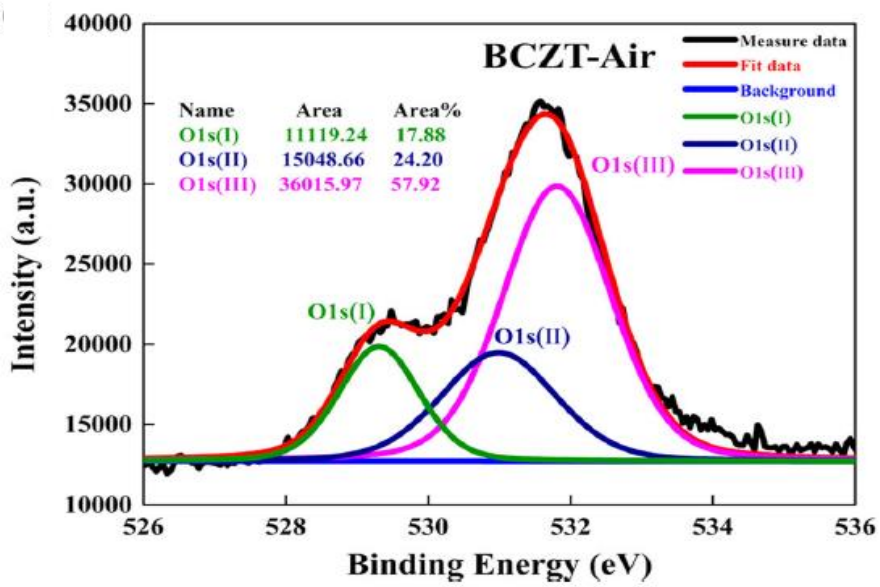

Figure 2.6 An example of XPS O1s spectrum of ceramic oxide [70].

2.5. Dielectric properties

In order to obtain flat ceramic samples with smooth top and bottom surfaces, the surfaces of the as-sintered ceramics were polished using sandpapers. The polished ceramic was then coated with top and bottom silver electrodes which were fired at 750°C for 30 min for the measurements of dielectric, piezoelectric and ferroelectric properties.

An impedance analyzer (HP 4294A, Agilent Technologies Inc., Palo Alto, CA) was used to measure the capacitance (C) and dielectric loss (tan δ) of the samples at 1 kHz at room temperature.

The dielectric constant which is also known as relative permittivity (ε_r) is then calculated from:

$$C = \frac{\varepsilon_0 \varepsilon_r \mathrm{A}}{\mathrm{d}} \tag{2.4}$$

where C is the capacitance, ε_0 is the permittivity of vacuum (~8.85×10^{-12} F/m), A is the area of the electrode and d is the thickness of the sample.

2.5.1. Temperature dependence of dielectric properties

The ceramic samples were placed on a temperature-controlled probe stage (HFS600E-PB4, Linkam Scientific Instrument, UK). The probe stage was connected to an impedance analyzer (Hewlett Packard 4194A, Agilent Technologies Inc., USA) for the temperature dependence dielectric properties measurement. A home-made LabVIEW program was used to control the temperature of the stage and collect data from the impedance analyzer.

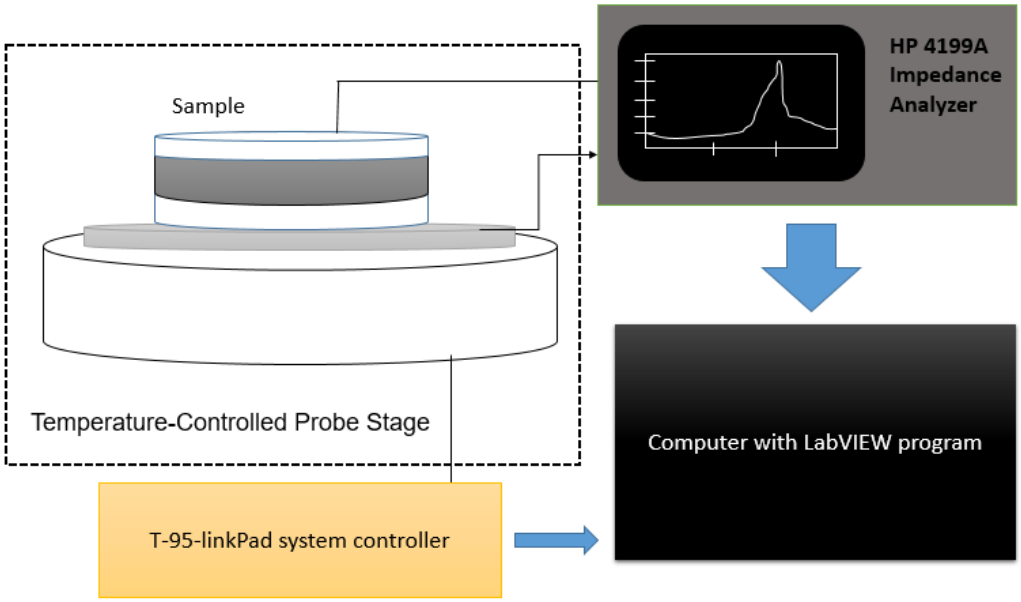

Figure 2.7 Schematic diagram of the dielectric measurement setup

2.6. Ferroelectric properties (P-E Loop)

As mentioned in Chapter 1, the ferroelectric properties of ferroelectric materials can be expressed by the ferroelectric (P-E) hysteresis loop. Through analysing the information from the P-E loop, the remnant polarization P_r, the coercive field E_c and the spontaneous polarization P_s of the material can be obtained. In this study, the P-E loop of the ceramic samples was obtained with a modified Sawyer-Tower circuit at 100 Hz. The schematic diagram of the P-E loop measurement setup is given in Figure 2.8. During the measurement, the ceramic sample was immersed in silicon oil to prevent electrical breakdowns. An AC voltage signal with a sinusoidal waveform was generated by a function generator (HP 91164A). The AC voltage signal was then amplified by 2000 times with a high voltage amplifier (Trek 609D-R 20/20A). A reference capacitor with a capacitance 1000 times larger than that of the ceramic sample was used to collect the charges generated from the ceramic sample. The voltages across the sample and the reference capacitor were

then measured by a digital oscilloscope. The data was recorded by a home-made Lab-VIEW program. The polarization (P) of the material was calculated by:

$$P = \frac{C_r V_0}{A} \tag{2.5}$$

where A is the area of the silver electrode, C_r is the capacitance of the reference capacitor and V_0 is the voltage across the reference capacitor.

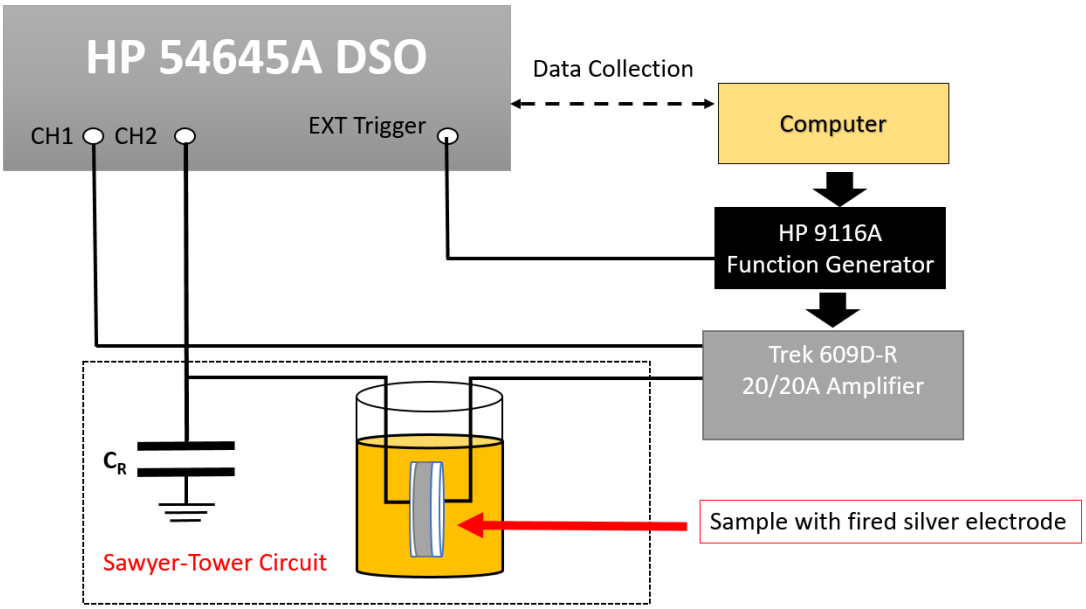

Figure 2.8 The schematic diagram of the P-E loop measurement setup.

2.7. Optical band gap estimation

The bandgap of the material was estimated by diffuse reflectance spectroscopy. Figure 2.9 shows the top view of the setup for the diffuse reflectance measurement.

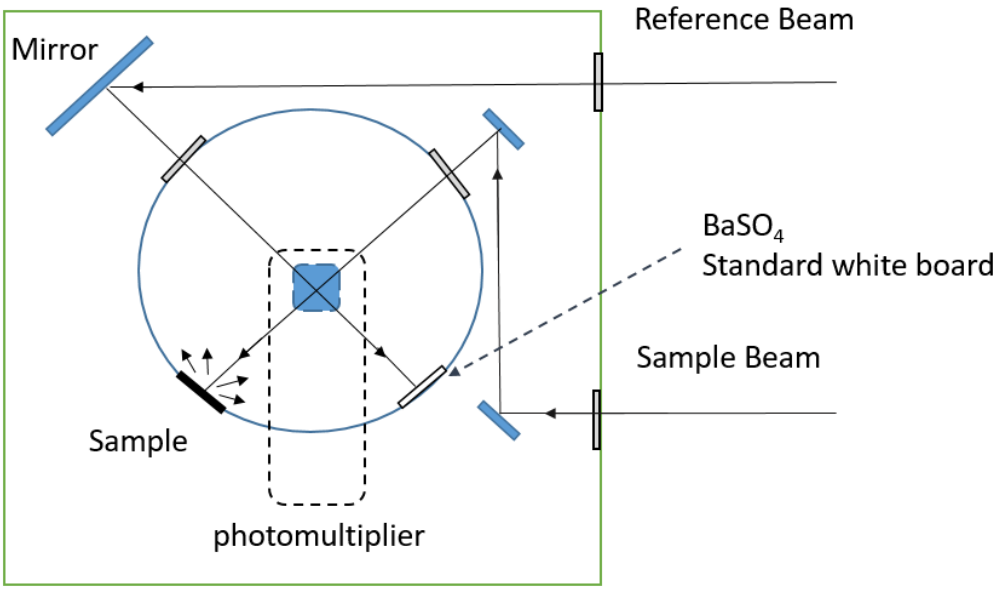

Figure 2.9 The top view of the diffuse reflectance measurement setup.

The disk shape ceramics were first ground into powder and sieved with an 80-mesh screen. $BaSO_4$ powder was used as a non-absorbing reference. The diffuse reflectances of the samples (in powder form) from 300 nm to 800 nm were measured with a UV-Vis spectrophotometer (UV-2550, Shimadzu Co.).

The absorption coefficient α of the samples was then calculated with the Kubelka-Munk (K-M) function [72]:

$$\alpha = \frac{(1-R)^2}{2R} = \frac{K}{S} \tag{2.6}$$

where R is the measured reflectance, K and S are the absorption and scattering coefficients.

After obtaining the absorption coefficient α, Tauc's plot was used to estimate the optical bandgap. The Tauc equation is expressed as follows:

$$(h\nu\alpha)^n = A(h\nu - E_g) \tag{2.7}$$

where h, ν and α is the Plank's constant, frequency of the photon, the absorption coefficient and the bandgap of the material respectively [73], [74]. A is the proportional constant of Tauc's plot in the linear region. n is the exponent coefficient which determines the nature of electronic transition [73], [74]. For n=2, the Tauc equation refers to the direct allowed transition while for n=0.5, it refers to the indirect allowed transition [74].

$(h\nu\alpha)^n$ was then plotted against $h\nu$ to estimate the bandgap of the material. The linear region of the curve was extended to the x-axis and the corresponding x-intercept indicated the bandgap of the material [74].

A typical Tauc's plot of Zinc Oxide (ZnO) thin film is shown in Figure 2.10 which is used as an example. The direct bandgap was estimated to be 3.35eV [73].

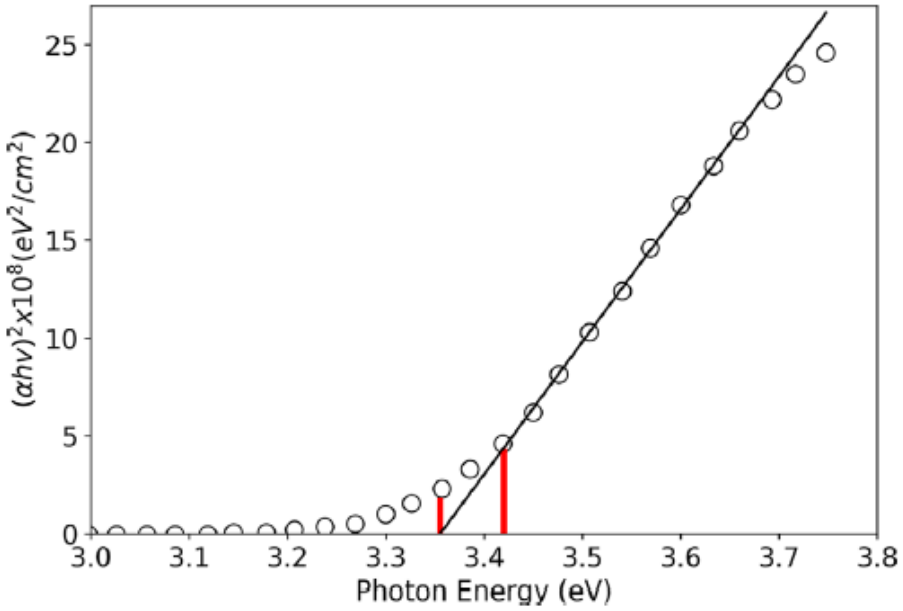

Figure 2.10 An example of Tauc's plot from UV-Vis analysis of a ZnO thin film. The direct band gap is estimated to be 3.35eV [74].

2.8. Photocurrent measurement

A solar simulator (Newport 91160, 300W) with an AM 1.5 filter (100mW/cm^2) was used as a light source to illuminate the samples. The photocurrent signals of the samples were collected by a Keithley 2410 sourcemeter and the data was recorded by a home-made LabVIEW program. Figure 2.11 shows a schematic diagram of the setup for the photocurrent response measurement.

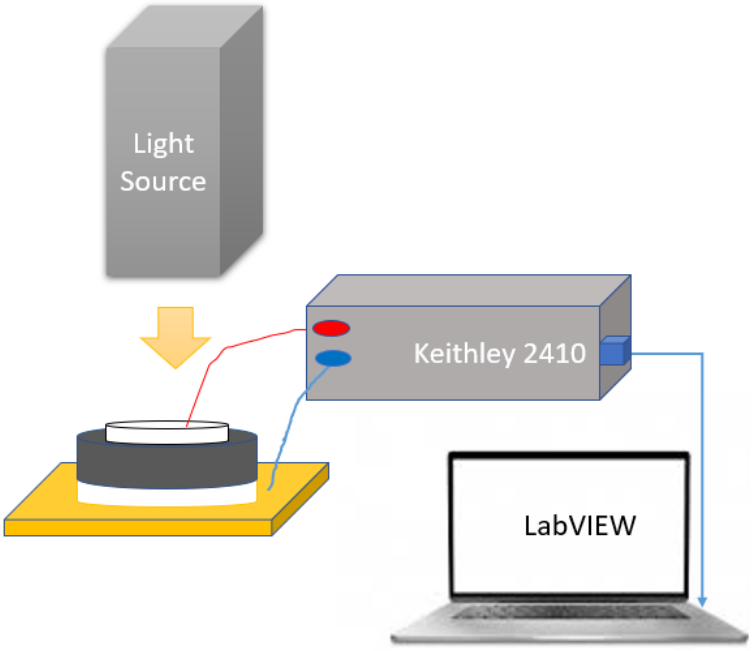

Figure 2.11 Schematic diagram of the setup for photovoltaic measurement.

Chapter 3. BCT-Fe-0.1 and BCT-Fe-0.025 Ceramics Sintered in Different Atmospheres

3.1. Introduction

As discussed in Chapter 1, defects such as oxygen vacancies will affect the photovoltaic performance of the ceramics. In addition, such defects are not preventable during the synthesis process of the ceramic samples [51]–[54], [66]. Although oxygen vacancies cannot be eliminated, it is possible to control the oxygen vacancy content inside the ceramics by sintering them in different atmospheres [51]–[54], [66]. Previous studies have reported that samples sintered in an oxygen-deficient atmosphere (such as pure nitrogen) will contain more oxygen vacancies than the samples sintered in an oxygen-rich atmosphere [17], [51]–[53], [56], [75].

The dielectric and ferroelectric properties of the BCT-Fe-0.025 and BCT-Fe-0.1 ceramics sintered in different atmospheres (N_2, air and O_2) are presented in this chapter. O1s XPS spectra have confirmed that the BCT-Fe-0.1 ceramics sintered in nitrogen contain the most oxygen vacancies. This result agrees with previous findings that the oxygen insufficient sintering atmosphere will create oxygen vacancies in the ceramics. The grain sizes of the ceramic samples were examined by SEM imaging. The SEM images of the samples show that the BCT-Fe-0.1and BCT-Fe-0.025 ceramics sintered in nitrogen have a larger grain size, which also agrees with previous studies.

In this chapter, the dielectric and ferroelectric properties of ceramics will be compared and discussed. The results show that the sintering atmosphere will greatly affect these properties which may affect the photovoltaic response of the samples.

3.2. SEM Image of the BCT-Fe-0.1 and BCT-Fe-0.025 ceramics

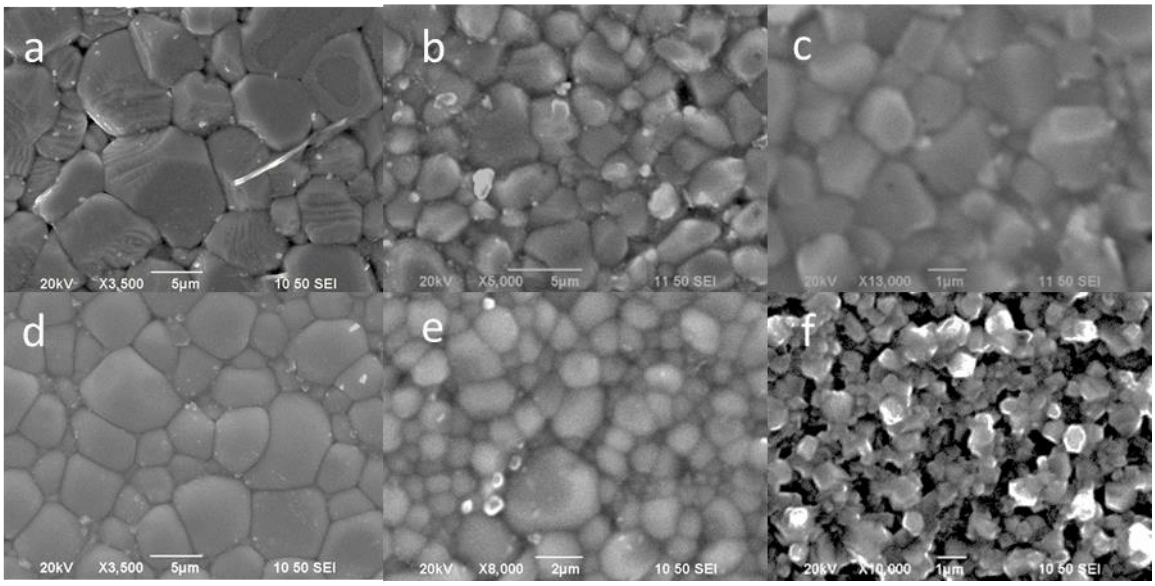

Figure 3.1 SEM micrograph of BCT-Fe-0.025 ceramics sintered in (a) N_2, (b) Air and (C) O_2 and BCT-Fe-0.1 ceramics sintered in (d) N_2, (e) Air and (f) O_2.

Figure 3.1 shows SEM images of the BCT-Fe-0.025 and BCT-Fe-0.1 ceramics sintered under different atmospheric conditions (N2, air and O2). As shown in Figure 3.1, for both BCT-Fe-0.025 and BCT-Fe-0.1, the samples sintered in the nitrogen atmosphere have the largest gain size while those sintered in the oxygen atmosphere have the smallest grain size. This result agrees with previous works which suggest that the grain growth of ceramics will be suppressed in an oxygen-rich sintering atmosphere. It is well known that the ceramic samples will contain more oxygen vacancies when they are sintered in oxygen-deficient atmospheres or under low oxygen pressure. Researchers believed that the increase of oxygen vacancies will assist the diffusion of oxygen ions and enhance densification [25], [69]–[71]. In other words, the oxygen vacancies inside the ceramics will enhance grain growth. Therefore, the ceramic samples sintered in nitrogen (oxygen-deficient) atmosphere have larger grain sizes and better densification [25], [69]–[71]. The

density of the BCT-Fe-0.025 and BCT-Fe-0.1 ceramics sintered in N2, air and O_2 are shown in Table 3.1.

Table 3.1 Density of the BCT-Fe-0.025 and BCT-Fe-0.1 ceramics sintered in N2, air and O2

Sample	Density (g/cm^3)
BCT-Fe-0.025-N_2	5.95
BCT-Fe-0.025-Air	5.84
BCT-Fe-0.025-O_2	5.81
BCT-Fe-0.1-N_2	5.93
BCT-Fe-0.1-Air	5.84
BCT-Fe-0.1-O_2	5.74

3.3. Crystalline structure

The crystalline structure of the BCT-Fe-0.1 and BCT-Fe-0.025 ceramics were examined by X-ray diffraction (XRD). The XRD patterns of the ceramic samples are shown in Figures 3.2 and 3.3. The results reveal that all the samples have a polycrystalline perovskite structure. No secondary phases are observed within the detection limit of our XRD. This gives evidence that Fe^{3+} ions have completely diffused into $Ba_{0.9}Ca_{0.1}TiO_3$ (BCT) lattices to form a new homogenous solid solution [20], [76], [77].

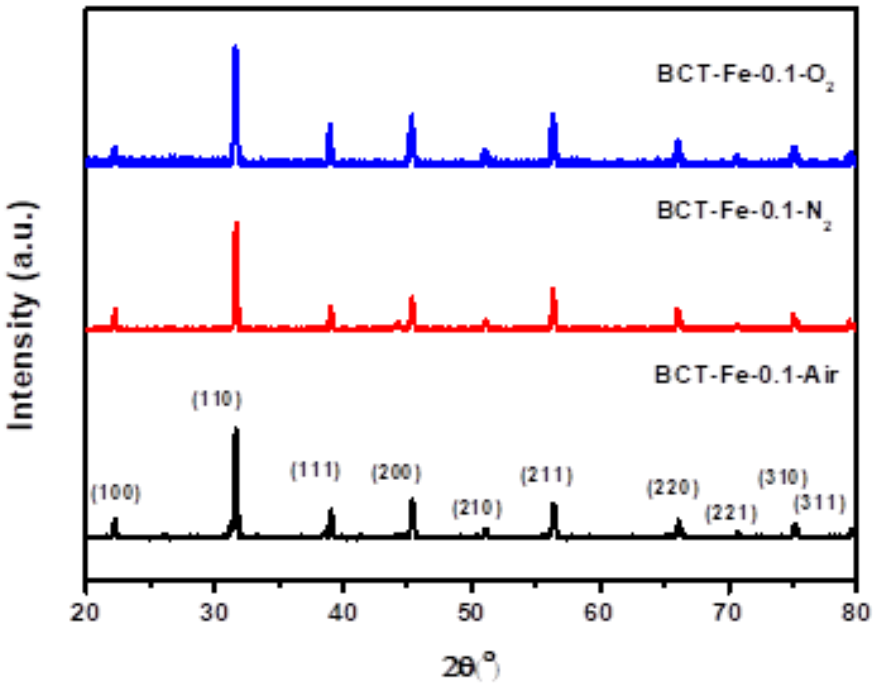

Figure 3.2 The XRD patterns of the BCT-Fe-0.1 ceramics in the range of 20°-80°.

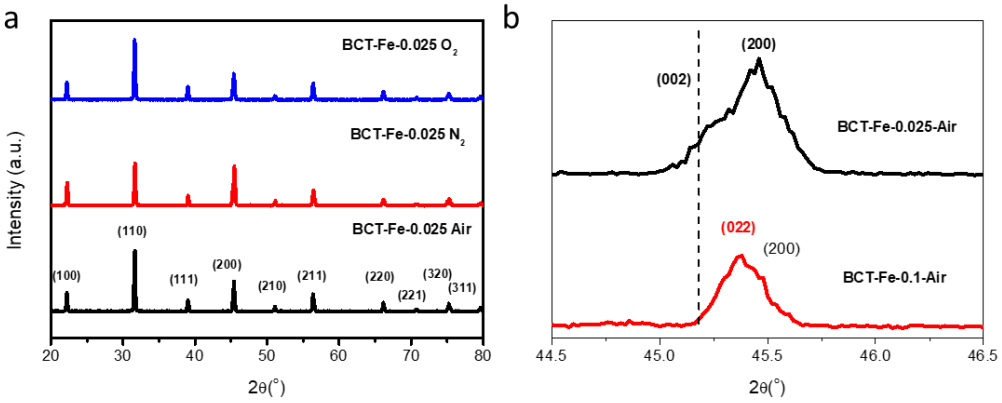

Figure 3.3 (a) The XRD patterns of the BCT-Fe-0.025 ceramics in the range of 20°-80°. (b) The XRD patterns of the BCT-Fe-0.1 and BCT-Fe-0.025 ceramics in the range of 44.5°-46.5°.

As shown in Figures 3.2 and 3.3, the XRD patterns of the BCT-Fe-0.1 and BCT-Fe-0.025 ceramics sintered in different atmospheres (N_2, Air and O_2) are similar. It is suggested the effect of the sintering atmosphere (N_2, air and O_2) on the crystal structure of the ceramics is limited.

The XRD patterns, in particular the (200) peak, of the BCT-Fe-0.1-Air and BCT-Fe-0.025-Air ceramics are compared, as an example, in Figure 3.3 b. It is observed that the peak of BCT-Fe-0.025-Air is more broadened, resulting from the splitting of the (002) and (200) peaks. It is suggested that the splitting of the (002) and (200) peaks is related to the electrostatic repulsion between the elections of O^{2-} in 2p valence states and those of Ti^{4+} in 3d valence states [44], [77], [78]. The observed split (002) and (200) peaks confirm that the BCT-Fe-0.025-Air ceramic has a tetragonal structure [77]. However, no splitting of the (002) and (200) peaks is observed for the BCT-Fe-0.1-Air ceramic. This implies that it has a cubic structure [78]–[80]. As mentioned, the splitting of the (002) and (200) peaks is related to the electrostatic repulsion between the O^{2-} 2p electrons and Ti^{4+} 3d electrons. It is expected that with increasing the Fe^{3+}doping level, the tetragonal structure of the ceramic will be distorted and the (002) and (200) peaks become merged [75]–[76].

3.3.1. XPS analysis (Binding energy)

To confirm the compositions of the BCT-Fe-0.1 and BCT-Fe-0.025 ceramics, the XPS measurements were conducted. The XPS survey spectra of the BCT-Fe-0.1 and BCT-Fe-0.025 ceramics sintered in N_2, air and O_2 are shown in Figure 3.4 and Figure 3.5 respectively. The XPS survey spectrums confirm that the BCT-Fe-0.1 and BCT-Fe-0.025 ceramics contain barium (Ba), calcium (Ca), titanium (Ti) and oxygen (O) [81]–[83]. The

strong C1s peak indicates the existence of carbon which originated from atmospheric contamination.

For the BCT-Fe-0.1 ceramic, as shown in Figure 3.5, the iron ($Fe2p_{3/2}$) peak in the XPS survey spectrum is very weak as the Fe^{3+} doping level of the ceramic is low.

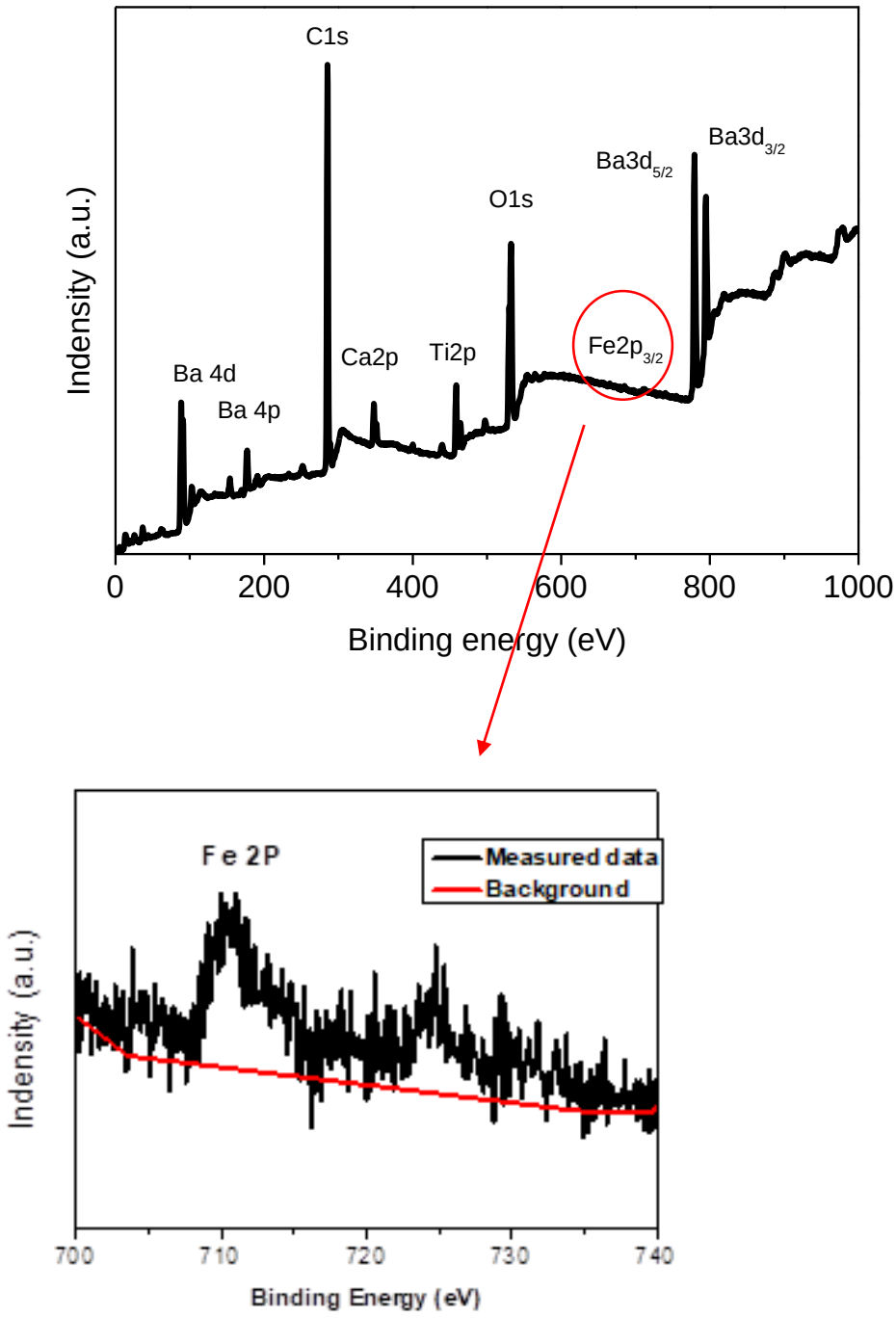

Figure 3.4 XPS survey spectrum of BCT-Fe-0.1 ceramics.

For the BCT-Fe-0.025 ceramics, the Fe^{3+}doping level is even lower. As a result, the $Fe2p_{3/2}$ peak from the XPS survey spectrum is more difficult to observe.

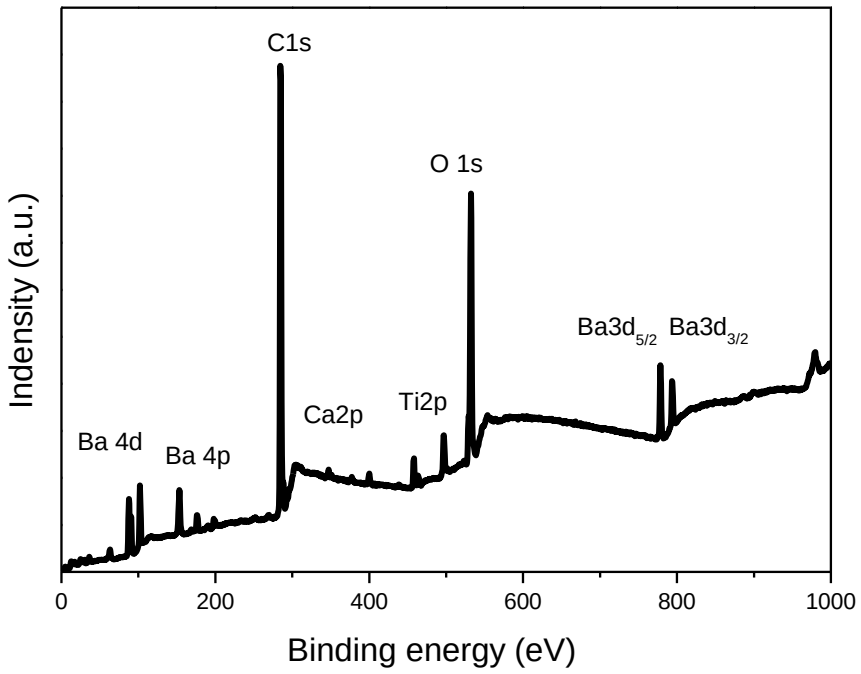

Figure 3.5 XPS survey spectrum of BCT-Fe-0.025 ceramics.

3.3.2. Oxygen vacancies analysis

As mentioned in Chapter 1, defects such as oxygen vacancies are unpreventable during the sample preparation. However, the oxygen vacancy content inside the material can be controlled by sintering the ceramic in different atmospheres [51], [54], [56], [84]. In this study, the BCT-Fe-0.1 and BCT-Fe-0.025 ceramics were sintered in O_2, air and N_2.

In Chapter 2, it has been discussed that the information on the oxygen vacancy content of the ceramics can be obtained through XPS O1s analysis. The XPS O1s spectrums

of all the BCT-Fe-0.1 ceramics have been deconvoluted into 3 corresponding peaks, i.e., O1s (I), O1s (II) and O1s (III), respectively, giving the results shown in Figure 3.6a to 3.6c.

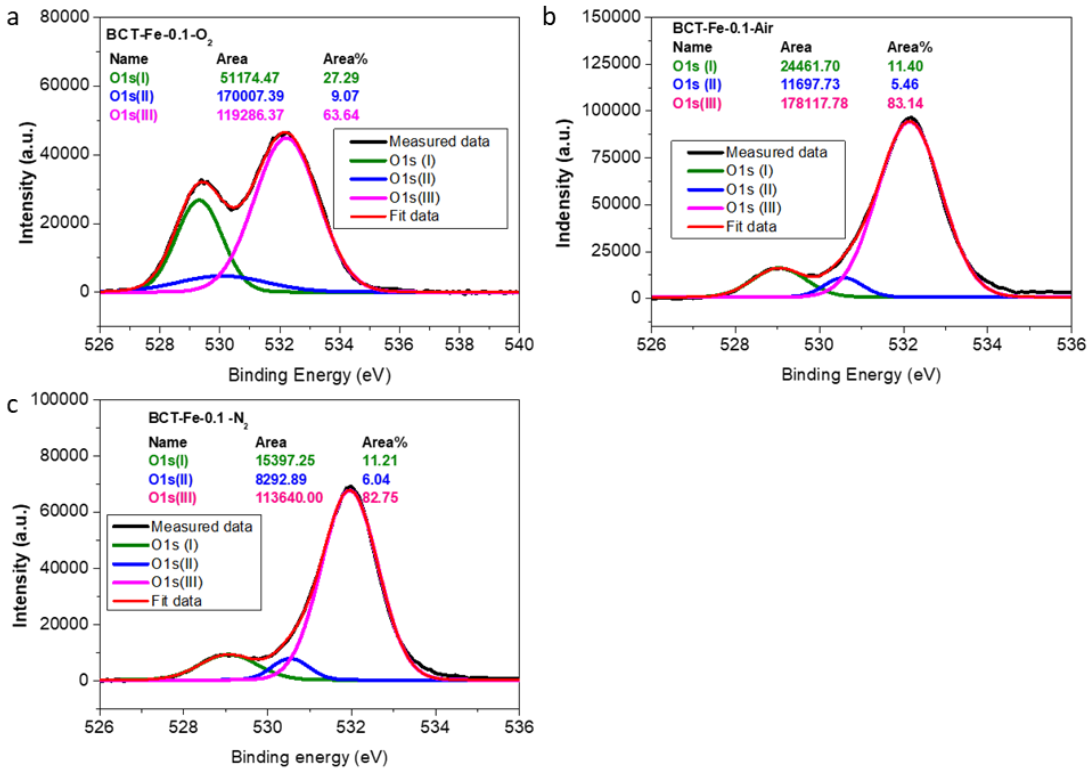

Figure 3.6 High-resolution O1s spectrum of the BCT-Fe-0.1 ceramics in various atmospheres: (a) O_2, (b) air and (c) N_2.

The O1s (I) peak (located at ~529.3eV) is related to the lattice oxygen ions, while the O1s (II) peak (530.95 eV) is attributed to the ions induced by the oxygen vacancies. The O1s (III) peak (531.74 eV) corresponds to the organic oxygen ions on the surface of the ceramics, and thus it has not been taken into account for analyzing the oxygen vacancy content of the ceramics. The oxygen vacancy content of the ceramics is estimated based on the area ratio between the O1s (II) and O1s (I) peaks. The larger the area ratio, the more oxygen vacancies the ceramic contains. The area ratios of the BCT-Fe-0.1 ceramics

sintered in O_2, air and N_2 are 0.33, 0.48 and 0.53 respectively. The results suggest that the BCT-Fe-0.1-O_2 ceramic contains the least oxygen vacancies, while BCT-Fe-0.1-N_2 contains the most oxygen vacancies, which agrees with the expectations that the oxygen vacancies inside the ceramic oxides increase when they are sintered in oxygen deficiency atmosphere (i.e., atmosphere with a lower partial pressure of O_2).

It is suggested that increasing the Fe^{3+} doping level in ceramics will increase the oxygen vacancy concentration [60]. In other words, by reducing the doping level, the ceramic will contain fewer oxygen vacancies. However, it is interesting to note that the XPS O1s spectra for all the BCT-Fe-0.025 ceramics are dominated by the O1s (III) peak and the O1s (I) and O1s (II) peaks become relatively weak. As a result, the corresponding area ratios cannot be calculated with reasonable accuracy and thus their oxygen vacancy contents cannot be estimated. Nevertheless, it is believed that the BCT-Fe-0.025 ceramic should contain fewer oxygen vacancies that BCT-Fe-0.1 due to the lower Fe^{3+} doping level.

3.4. Dielectric properties

The dielectric constant (ε_r) and dielectric loss (tan δ) of the BCT-Fe-0.025 and BCT-Fe-0.1 ceramics sintered in different atmospheres were measured at 1kHz at room temperature. The tan δ of all the ceramics are below 5%, suggesting that they are well sintered and dense enough for practical applications. Table 3.2 summarizes the ε_r and tan δ of the ceramics. It can be seen that the observed ε_r of the BCT-Fe-0.025 ceramics (2800 to 3400) are much larger than those of the BCT-Fe-0.1 ceramics (650-760).

For the BCT-Fe-0.1 ceramics, the one sintered in nitrogen has higher ε_r and a lower tan δ as compared to those sintered in oxygen and air. As discussed in Section 3.2 (Fig.

3.1), the BCT-Fe-0.1-N2 ceramic has the largest grain size, relatively more coarse-grained microstructure and better densification. Probably partly because of this, it exhibits the lowest tan δ [85]–[88]. On the contrary, the BCT-Fe-0.1-O_2 ceramic has the smallest grain size and thus the highest tan δ.

Table 3.2 The dielectric constant (ε_r) and dielectric loss (tan δ) of BCT-Fe-0.025 and BCT-Fe-0.1 ceramics sintered in different atmospheres were measured at 1kHz at room temperature

Sample	εr	tan δ(%)
BCT-Fe 0.1-O_2	650	4.9
BCT-Fe 0.1-Air	690	3.5
BCT-Fe 0.1-N_2	760	1.1
BCT-Fe 0.025-O_2	2800	2.2
BCT-Fe 0.025-Air	3400	1.2
BCT-Fe 0.025-N_2	3400	1.1

3.5. Temperature dependence of dielectric property

The temperature and frequency dependence of dielectric constant (εr) and dielectric loss (tan δ) of BCT-Fe-0.025 ceramics have also been measured at 1 kHz, 10 kHz and 100 kHz in a temperature range of 30°C to 150°C. The BCT-Fe-0.025-Air ceramic (i.e., sintered in Air) is used as an example to demonstrate the dielectric response of the BCT-Fe-0.025 ceramics at various frequencies (1 kHz, 10 kHz and 100 kHz), as shown in

Figure 3.7. A broad dielectric constant versus temperature curve near the transition temperature is observed in BCT-Fe-0.025 ceramics. In addition, the transient temperatures of the BCT-Fe-0.025 ceramics are frequency-independent. Therefore, it is suggested that the BCT-Fe-0.025 ceramics exhibit diffuse phase transition.

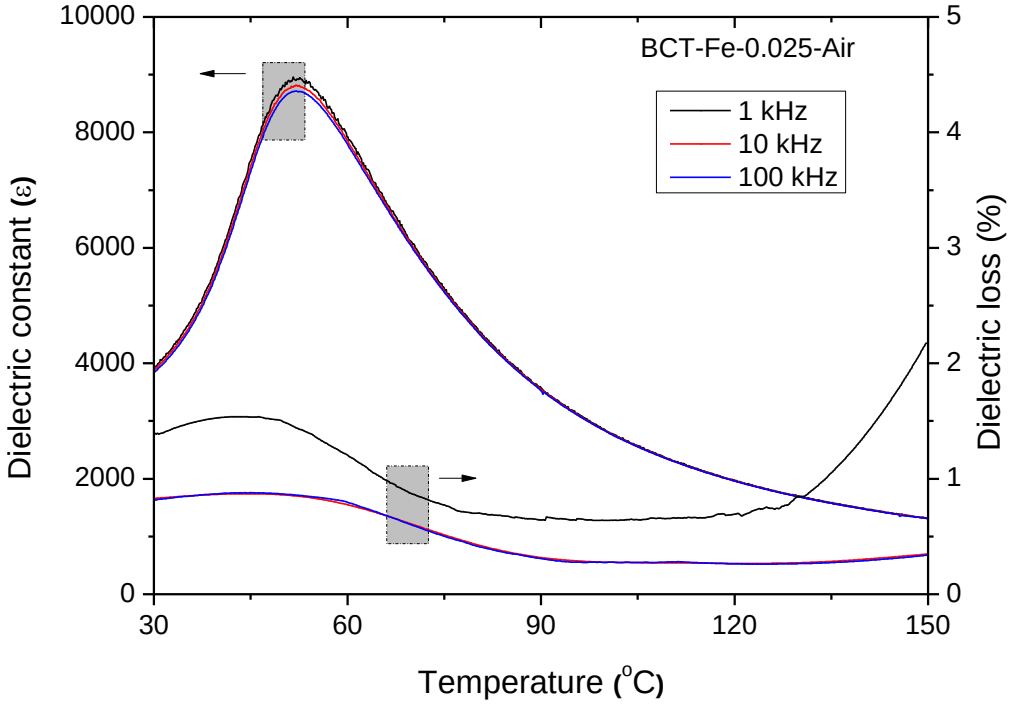

Figure 3.7 Temperature dependence of dielectric constant and dielectric loss of BCTFe-0.025-Air ceramics measured at 1 kHz, 10 kHz and 100kHz.

The dielectric constant (ε_r) of the BCT-Fe-0.025 ceramics sintered in different atmospheres has also been measured at 1 kHz in a temperature range of 30°C to 150°C, giving the results shown in Figure 3.8. All the ceramics exhibit a transition peak associated with the ferroelectric tetragonal to paraelectric cubic phase transition at ~ 55°C,

which is defined as the Curie temperature (T_c). It can be seen that the effect of the sintering atmosphere on the transition temperature is not significant, only causing a variation of about 3°C.

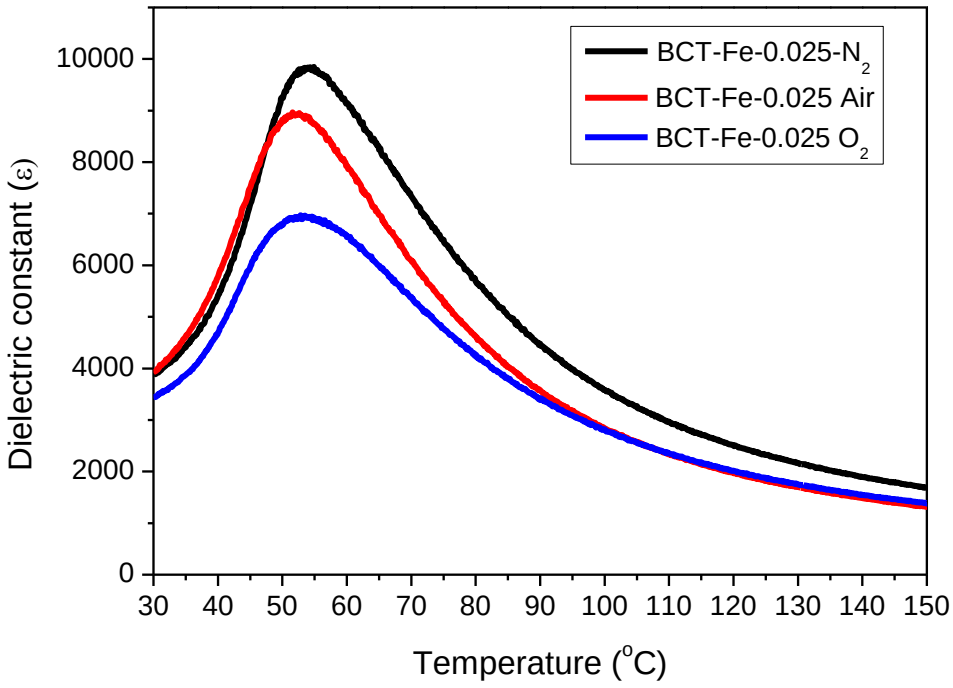

Figure 3.8 Temperature dependence of dielectric constant of BCTFe-0.025 ceramics sintered in various atmospheres (O_2, Air and N_2) at 1 kHz.

Figure 3.9 shows the temperature dependence of ε_r for the BCT-Fe-0.1 ceramics sintered in different atmospheres, in which the temperature range is extended to -50°C for arching the phase transitions. Unlike BCT-Fe-0.025, all the BCT-Fe-0.1 ceramics exhibit no transition peaks in the temperature range of -50°C to 120°C, suggesting that they all are non-ferroelectric at room temperature.

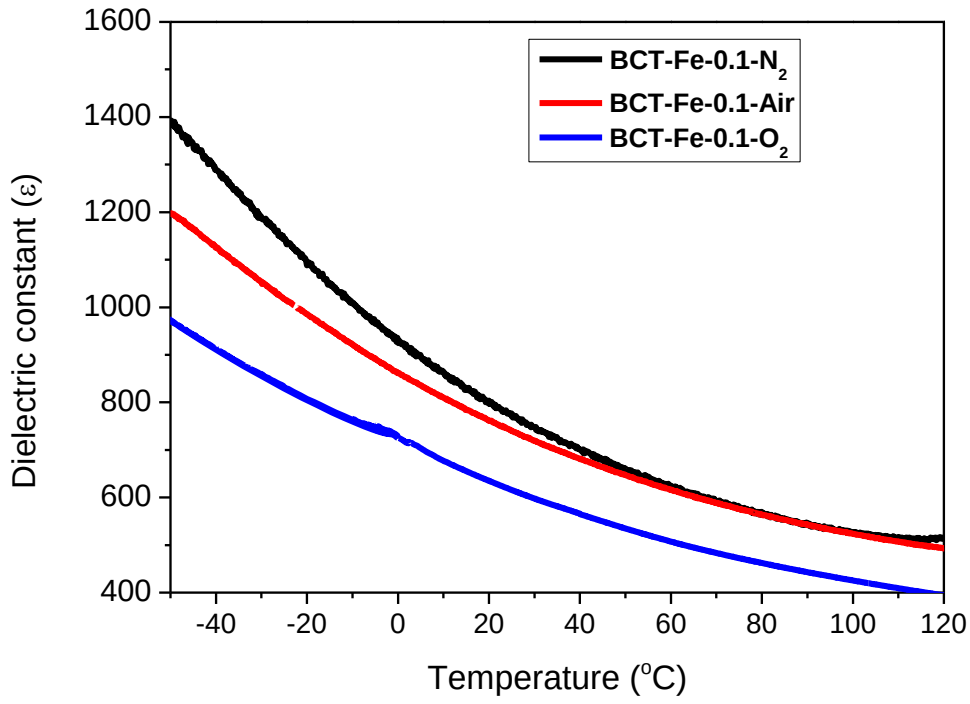

Figure 3.9 Temperature dependence of dielectric constant of BCTFe-0.1 ceramics sintered in various atmospheres (O_2, Air and N_2) at 1 kHz.

3.6. Ferroelectric properties

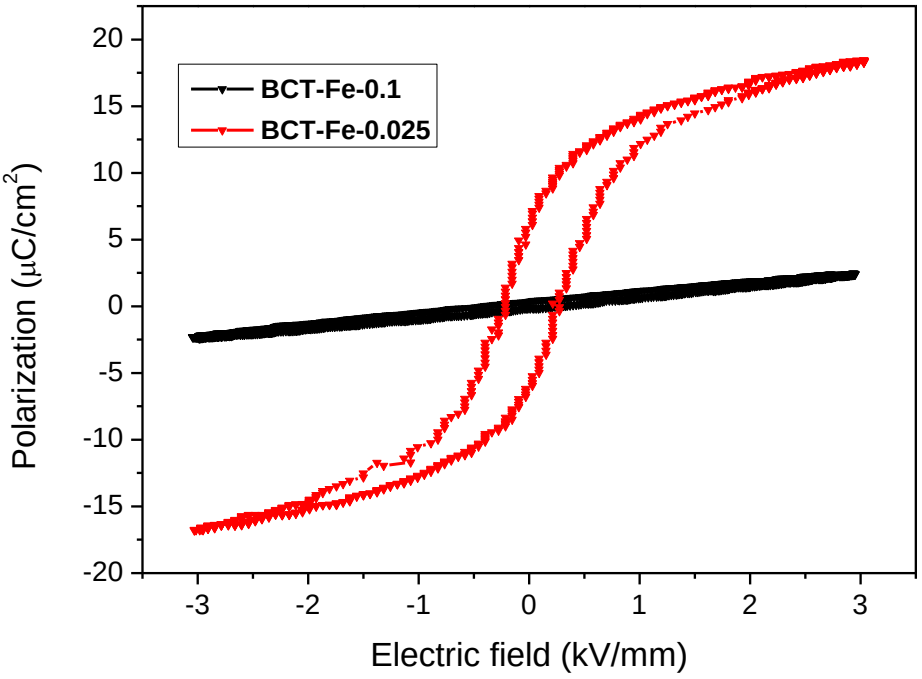

Figure 3.10 Ferroelectric properties of the BCT-Fe-0.025 and BCT-Fe-0.1 ceramics.

The ferroelectric properties of the BCT-Fe-0.025 and BCT-Fe-0.1ceramics can be evaluated based on their P-E loops. The P-E loops of all the ceramics have been measured under an electric field of 3 kV/mm at 100 Hz at room temperature. Figure 3.10 shows, as examples, the P-E loops for the ceramics sintered in Air. It can be seen that the relationship between the observed polarization and electric field is almost linearly for BCT-Fe-0.1, confirming that it is non-ferroelectric at room temperature. On the other hand, the BCT-Fe-0.025 ceramic exhibits a typical P-E loop, substantiating its ferroelectric characteristics. These agree with the above measurements of the temperature dependence of the dielectric constant.

3.6.1. P-E Loops of BCT-Fe-0.025 ceramics sintered in different atmospheres

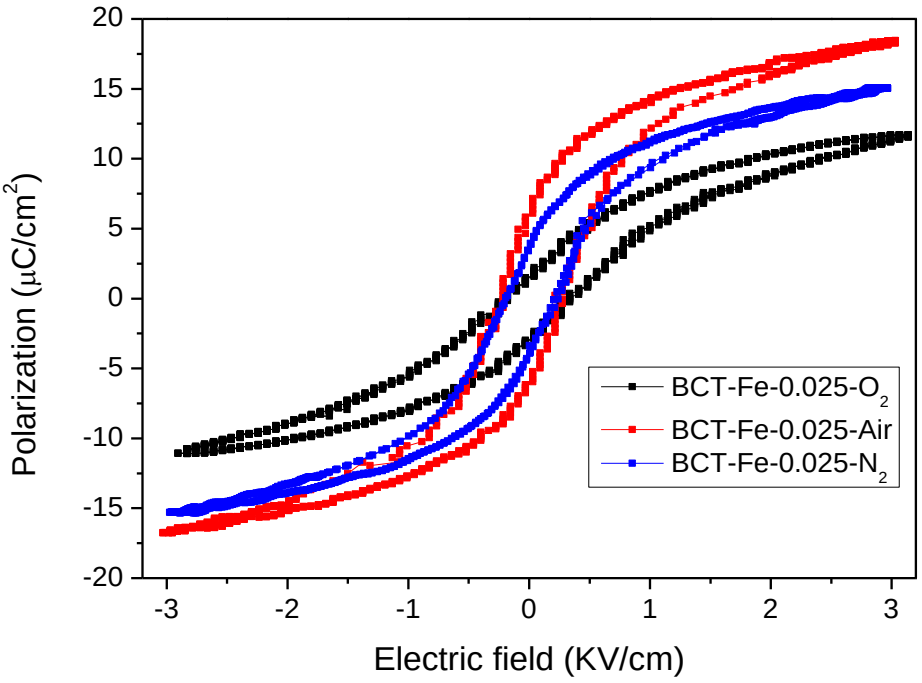

Figure 3.11 The P-E Loops of BCT-Fe-0.025 ceramics sintered in O_2, air and N_2.

Figure 3.11. shows the P-E loops of the BCT-Fe-0.025 ceramics sintered in oxygen, air and nitrogen. The observed saturated polarization (P_s), remnant polarization (P_r) and coercive field (E_c) are summarized in Table 3.3. It can be seen the sintering atmosphere can greatly affect the ferroelectric properties of the ceramics. For the ceramic sintered in O_2, i.e., BCT-Fe-0.025-O_2, it has the lowest P_r and P_s. Mudinepalli and his research team found that the spontaneous and remanent polarization of the BT-based ceramic increases with the increase of their grain sizes [85]–[87], [89]. They explained their findings by considering the effect of grain boundaries. Grain boundary is a low-permittivity region with poor ferroelectricity. In addition, space charges are easier to accumulate in grain

boundaries. It is believed that the number of grain boundaries increases as the grain size decreases Therefore, the remanent polarization of the ceramics decreases with the grain size.

As discussed in Chapter 3.1, it is suggested that the BCT-Fe-0.025-O_2 ceramic samples have the smallest grain size. As a result, it is expected that the BCT-Fe-0.025-O_2 samples have the smallest spontaneous polarization. However, the BCT-Fe-0.025-N_2 have the largest grain size have a lower Pr than the sample sintered in air. There must be other factors that contribute to such results. It is suggested that oxygen vacancies will reduce the polarization of the ceramic [86], [88]. It is believed that the sample sintered in N_2 contains more oxygen vacancies than the sample sintered in Air. Probably because of the coupling effect of grain sizes and concentration of oxygen vacancies, the remnant and spontaneous polarizations of the BCT-Fe-0.025-Air are slightly larger than the BCT-Fe-0.025-N_2.

Table 3.3 Summary of ferroelectric properties of the BCT-Fe-0.025 ceramics sintered in O_2, Air and N_2

Sample	Pr ($\mu C/cm^2$)	Ps ($\mu C/cm^2$)	Ec (kV/mm)
BCT-Fe 0.025-O_2	2.5	10	0.44
BCT-Fe 0.025-Air	4.5	18	0.27
BCT-Fe 0.025-N_2	3.8	15	0.22

3.7. Optical bandgap estimation

3.7.1. Tauc's plot of BCT-Fe-0.1 and BCT-Fe-0.025 ceramics sintered in various atmospheres

The diffuse reflectance spectra of the BCT-Fe-0.1 and BCT-Fe-0.025 ceramics sintered in different atmospheres (N_2, air and O_2) have been measured and based on which the corresponding Tauc's plots have been obtained, giving the results shown in Figure 3.12. Following the Tauc's model, the bandgap has been determined from the x-intercept of the extrapolation of the plot, giving the results summarized in Table 3.4. In general, the ceramics with a higher doping level of Fe^{3+} have a lower bandgap. This agrees with previous results in which the bandgap of barium titanates-based ceramics can be lowered by the doping of Fe^{3+}, and the reduction increases with the doping content [90].

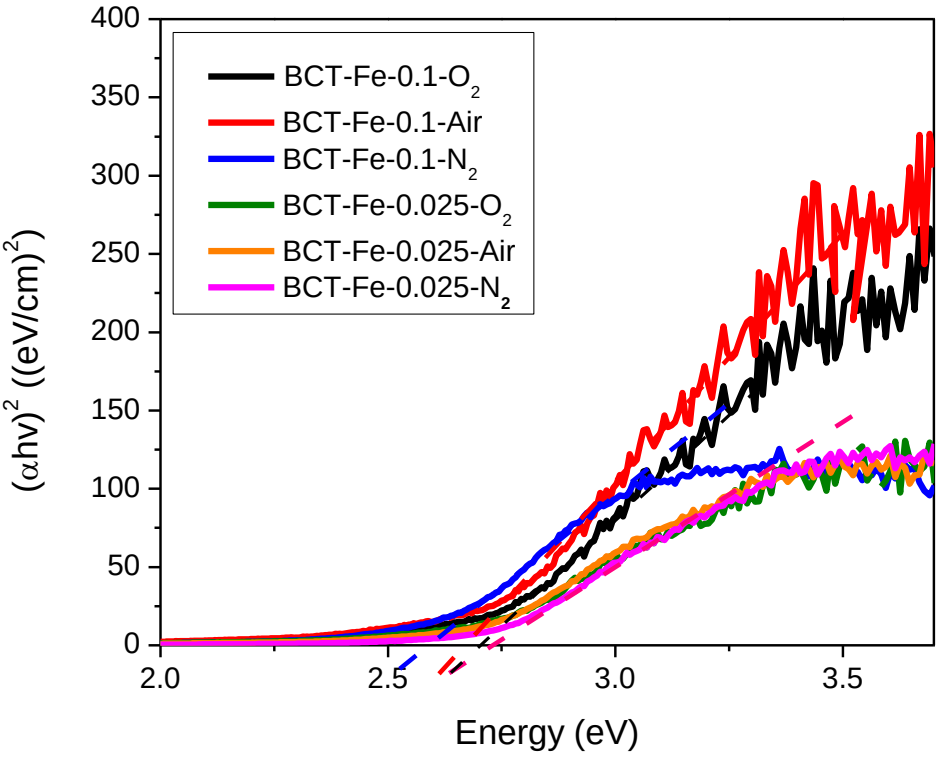

Figure 3.12 Tauc's plot of BCT-Fe-0.1 and BCT-Fe-0.025 ceramics.

It has also been suggested that oxygen vacancies will affect the bandgap of ceramic oxides [50]. When a large amount of oxygen vacancies exists in the ceramics, they will induce delocalized impurity states which overlap with the edge of the valence band. In consequence, the position of the valence band will be raised and the bandgap will become narrowed. As a result, the ceramic oxides that contain more oxygen vacancies are expected to have a narrower bandgap [50], [91]. As discussed in Chapter 3.2, the BCT-Fe-0.1 ceramics will contain more oxygen vacancies if they are sintered in oxygen deficiency atmospheres. Therefore, it is expected that the ceramics sintered in N_2 will contain more oxygen vacancies and have a lower bandgap. In contrast, the ceramics sintered in O_2 will contain fewer oxygen vacancies and have a wider optical bandgap. Although the change

is not very large, our results still agree with the expectation, i.e., the BCT-Fe-0.1-N2 ceramic exhibits the narrowest optical bandgap (~2.60 eV) while the BCT-Fe-0.1-O_2 ceramic has the largest bandgap (~2.69 eV).

However, probably because of the low doping level of Fe^{3+}, the effect of the sintering atmosphere on the oxygen vacancies is limited, and thus the BCT-Fe-0.025 ceramics sintered in N_2, air and O_2 exhibit similar bandgaps (~2.75 eV).

Table 3.4 Estimated optical band gaps of BCT-Fe-0.1 and BCT-Fe-0.025 ceramics

Sample	E_g (eV)
BCT-Fe-0.1-O_2	2.69
BCT-Fe-0.1-Air	2.67
BCT-Fe-0.1-N_2	2.60
BCT-Fe-0.025-O_2	2.75
BCT-Fe-0.025-Air	2.75
BCT-Fe-0.025-N_2	2.75

3.8. Conclusions

The BCT-Fe-0.1 and BCT-Fe-0.025 ceramics have been successfully synthesized with solid-state reactions. The XRD patterns reveal that all the ceramics have a pure perovskite structure. All the Fe^{3+} ions have diffused into the BCT lattices to form a solid solution. The XPS O1s spectrums also reveal that the ceramics contain more oxygen vacancies if they are sintered in an oxygen-deficient atmosphere (e.g., N_2).

The physical properties of the BCT-Fe-0.1 and BCT-Fe-0.025 ceramics (sintered in different atmospheres) have been studied. The BCT-Fe-0.025 ceramics exhibit ferroelectricity at room temperature. The Curie temperature of the ceramic sintered in O_2, air and N_2 varies slightly from 53°C to 56°C. Moreover, the BCT-Fe-0.025 ceramic sintered in Air has the maximum remnant polarization P_r and saturated P_s. The optical bandgaps of the BCT-Fe-0.1 and BCT-Fe-0.025 ceramics have been estimated using diffuse reflectance spectroscopy. The optical bandgaps of the BCT-Fe-0.1 ceramics sintered in O_2, air and N_2 are ~2.69 eV, 2.67 eV and 2.60 eV, respectively. It is suggested that the ceramic sintered in an oxygen deficiency atmosphere will contain more oxygen vacancies, which will induce delocalized impurity states overlapping with the edge of the valence band and thus narrow the bandgap. However, probably because of the low doping level of Fe^{3+}, the effect of the sintering atmosphere on the oxygen vacancies is limited, and thus the BCT-Fe-0.025 ceramics sintered in N_2, air and O_2 exhibit similar bandgaps (~2.75 eV).

Chapter 4. Photocurrent Response of BCT-Fe-0.1 Non-ferroelectric Ceramics

4.1. Introduction

As discussed in Chapter 3, the P-E hysteresis loops have shown that the BCT-Fe-0.1 ceramics are non-ferroelectric at room temperature. It is thus expected that they will not exhibit any ferroelectric photovoltaic responses. However, photocurrent has been observed when they are illuminated.

In addition, previous studies have shown that oxygen vacancies can contribute to the photocurrent response. The XPS O1s spectra discussed in Chapter 3 confirmed that the BCT-Fe-0.1 ceramics sintered in different atmospheres (O_2, air and N_2) will have different oxygen vacancy contents.

In this chapter, the photocurrent responses of the BCT-Fe-0.1 ceramics sintered in different atmospheres are presented and discussed. Symmetric (i.e., both the top and bottom electrodes are ITO or Au) electrode configurations were used to study the photocurrent response of the ceramics. The symmetric electrode configuration was used to eliminate the impact of the Schottky barrier arising from the asymmetry electrode configuration. The photo-induced short-circuit current of the ceramics under AM 1.5G illumination (100 mW/cm^2) was measured for showing the influence of oxygen vacancies on the photocurrent response. The photocurrent response of the as-fabricated ceramics was first measured. An external electric field was then applied to the ceramics for 60 minutes at different temperatures (i.e., room temperature and 100^{o}C), and the photocurrent of the ceramics after short-circuited for 24 hours was re-measured. It has been shown that there

is no influence on the photocurrent response if the electric field is applied to the ceramics at room temperature. This result is expected as the BCT-Fe-0.1 ceramics are not ferroelectric and therefore there is no spontaneous polarization in the ceramics which will affect the photocurrent response. However, if the electric field is applied at 100^{o}C, the photocurrent can be modified, which has never been reported.

4.2. Photocurrent response of the BCT-Fe-0.1 ceramics with the symmetric electrode configuration

A non-negligible photocurrent response is observed for as-fabricated non-ferroelectric BCT-Fe-0.1 ceramics. It is suggested that oxygen vacancy is the major factor that contributes to the photocurrent response [15], [48], [57]. Researchers believed that defects such as oxygen vacancies may not evenly distribute in the ceramics but accumulate near one side of the sample, which will reduce the Schottky barrier at the ceramic-electrode interface. As a result, Schottky barriers with different barrier heights can even be formed in ceramics with symmetric electrode configuration and thus induce a net built-in electric field to drive the photo-induced holes and electrons. Moreover, oxygen vacancies can trap the photo-induced electrons and the photo-induced holes become the extra charge carriers which contribute to the diffusion current. Figure 4.1 shows the schematic diagram of a BCT-Fe-0.1 ceramic with oxygen vacancies accumulated near the top electrode. When the top electrode is illuminated, a downward (net) photocurrent flowing from the top electrode to the bottom electrode is generated. The photocurrent is composed of two components, i.e., diffusion current $I_{diffusion}$ and drift current I_{drift}. $I_{diffusion}$ is resulted from the separation of photo-induced electron-hole pairs during the illumination (Fig. 4.1) $I_{diffusion}$ always depends on the gradient of the induced charge carriers which flows in the downward direction (top / illuminated electrode to the bottom electrode). On the other hand, I_{drift} is

affected by the internal (or built-in) electric field at the ceramic-electrode interface. As shown in Figure 4.1, oxygen vacancies accumulate near the top electrode, which will reduce the Schottky barrier and then decrease the (outward) built-in electric field at the (top) interface. In contrast, without the effect of oxygen vacancies, a strong (outward or downward) built-in field is created at the interface of the ceramic and bottom electrode due to the (unaffected) Schottky barrier. As a result, a net downward built-in electric field is formed, which induces a downward drift current under the illumination. In this chapter, a downward current is defined as a positive current.

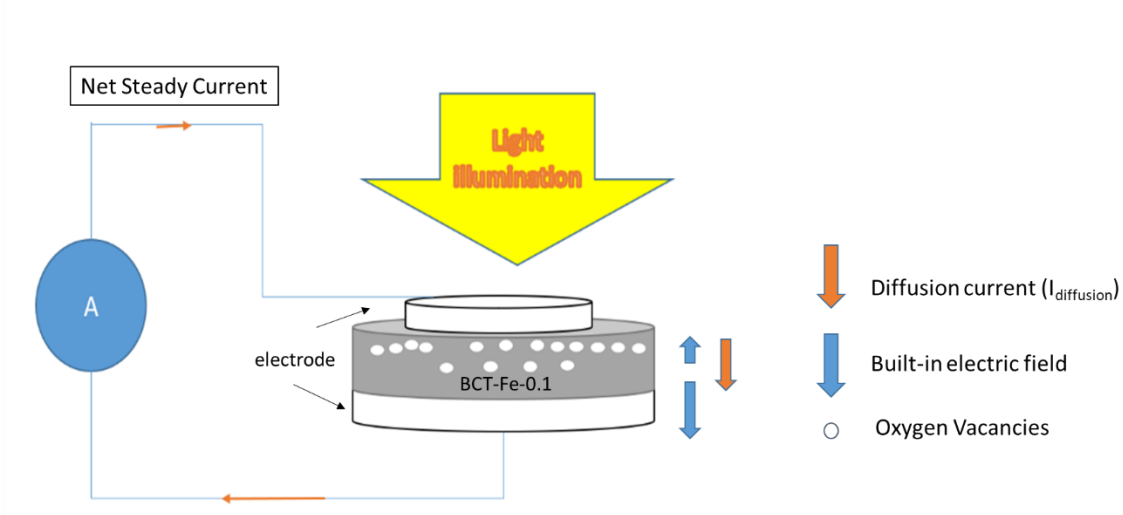

Figure 4.1 Schematic diagram of a BCT-Fe-0.1 ceramic with oxygen vacancies accumulated near the top electrode. . The orange and blue arrows indicate the direction of the diffusion current and the built-in electric field.

The photocurrent responses of the BCT-Fe-0.1ceramics sintered in N_2, air and O_2 are shown in Figure 4.2. It can be seen that both the BCT-Fe-0.1-O_2 and BCT-Fe-0.1-Air ceramics (i.e., sintered in O_2 and air, respectively) exhibit a photocurrent of 4.8 nA/cm^2 and 3.5 nA/cm^2, respectively, while no response is observed for BCT-Fe-0.1-N_2.

It has also been observed that the short-circuit photocurrents of both the BCT-Fe-0.1-Air and BCT-Fe-0.1-O_2 ceramics keep increasing under the illumination. As the temperature of the ceramics increases during the illumination process, it is suggested that the increase of the short-circuit current is due to the increase in the conductivity and the charge mobility of the ceramics. Moreover, positive (negative) current peaks are observed for the BCT-Fe-0.1-O_2 ceramic at the moment when the light is switched on (off). As discussed in Chapter 1, the photocurrent is mainly contributed by diffusion current ($I_{diffusion}$) and drift current (I_{drift}). At the moment when the light is switched on, it is suggested that the numbers of photo–induced electrons will suddenly increase and thus leading to a large $I_{diffusion}$ [15], [58], [59], [92]. The photo-induced electrons may recombine afterwards. As a result, $I_{diffusion}$ decreases and I_{drift} becomes the dominant portion of the photocurrent. On the other hand, when the light is switched off, the photo-induced electrons will recombine quickly and the trapped electrons will release, thus leading to a reverse (negative) diffusion current ($I_{diffusion}$). Further investigations are needed for verifying the proposed mechanism of the photocurrent response observed for the BCT-Fe-0.1-O_2 ceramic.

For the BCT-Fe-0.1-N_2 ceramic, only weak and sharp current peaks (0.38 nA or 0.75 nA/cm^2) are observed at the moment when the light is switched on or off. Similarly, the current peaks should be related to $I_{diffusion}$ and charge recombination [14]. During the illumination, no steady photocurrent is observed, which should be due to the weakness of the current and/or the limitation of the Keithley 2410 sourcemeter.

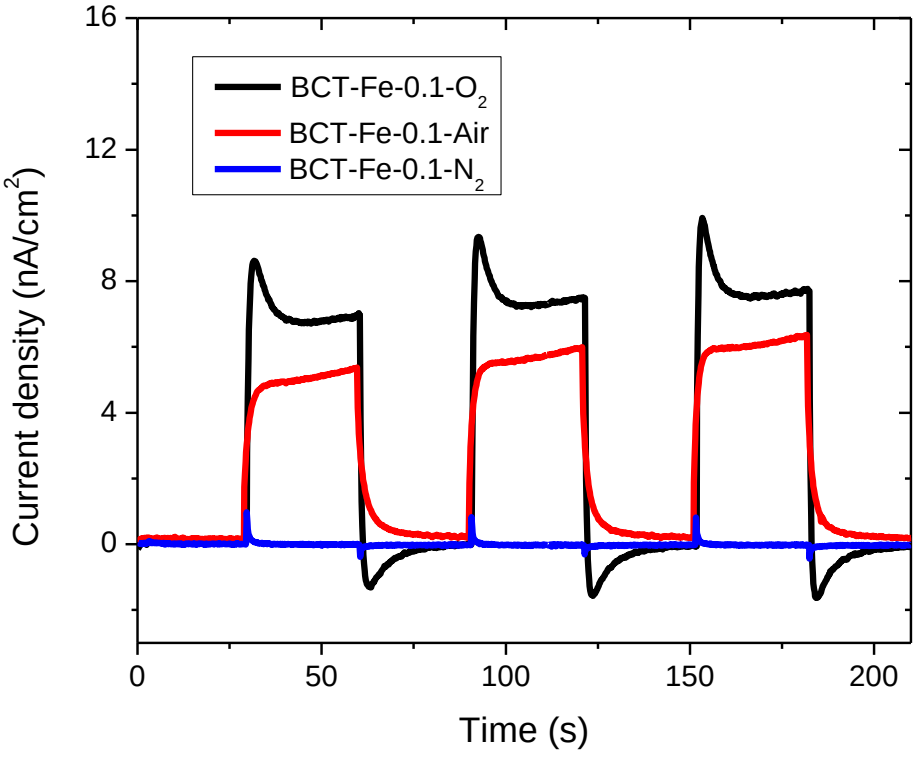

Figure 4.2 The short-circuit photocurrent of the BCT-Fe-0.1-N_2, BCT-Fe-0.1-Air and BCT-Fe-0.1-O_2 under periodic AM 1.5G illumination.

Among all the ceramics, BCT-Fe-0.1-N_2 contains the most oxygen vacancies. Although oxygen vacancies are suggested to be essential for the photocurrent response of the non-ferroelectric BCT-Fe-0.1 ceramics, a high oxygen vacancy content may suppress the photocurrent response. As discussed in Chapter 1, oxygen vacancies can contribute to the photocurrent response when they accumulate near one side of the ceramic. In other words, the oxygen vacancies which do not accumulate near one side (either the top or bottom electrode) of the ceramic will not contribute to the photocurrent response. In addition, if the content of the non-accumulated oxygen vacancies is too high, they will trap the drifted photo-induced electrons and then act as additional sites for the recombination

of electrons and holes [93]. Therefore, they will suppress the photocurrent response [94]–[96], thus leading to a very weak photocurrent.

Surprisingly, the BCT-Fe-0.1-O_2 ceramic exhibits the strongest photocurrent response. The XPS O1s spectrum shows that the ceramic also contains oxygen vacancies. It is then suggested that the oxygen vacancies accumulate near the top surface and induce a net built-in field (pointing downward) for the photocurrent response. Moreover, it contains the fewest oxygen vacancies, and thus fewer photo-induced electrons will be trapped by the oxygen vacancies. As a result, the BCT-Fe-0.1-O_2 ceramic exhibits the strongest photocurrent response.

4.3. Controllable photocurrent response of the BCT-Fe-0.1 ceramics with ITO electrodes

Researchers suggested that oxygen vacancies can migrate under an external electric field [11]–[19], [34], [49], [66]. It is then anticipated that the oxygen vacancies accumulated near the top electrode of the as-fabricated ceramics can be dispersed by the application of an external electric field, and thus the built-in electric field will decrease and the photocurrent response will become weakened. For verifying the anticipation, an external electric field of 1.5 kV/mm has been applied to the BCT-Fe-0.1 ceramics at room temperature. Probably because of the low mobility at low temperatures and then no migration, almost no changes in the photocurrent response are observed for all the ceramics. However, when the electric field is applied at 100^{o}C, noticeable changes in both the magnitude and direction of the photocurrent are observed for all the ceramics.

Chen and his research team have reported that enhanced photovoltaic performance of $BiFeO_3$ thin films can be observed after applying an electric field at high temperatures

[9]. It has been hypothesized that increasing the temperature of the sample will increase the mobility of oxygen vacancies which favours their migration under an external electric field. It is thus suggested that the distribution of oxygen vacancies in the BCT-Fe-0.1 ceramics can be modulated by a strong external electric field at high temperatures such as 100^{o}C. Figure 4.3a shows the schematic diagram of the setup used for applying an external electric field. A heater was used to heat the sample to 100^{o}C before applying the external electric field. Similar to the photocurrent, a downward electric field is defined as a positive electric field in this work. After applying a positive electric field, it is expected the oxygen vacancies will migrate toward the bottom electrode [9], [15], [97]. The sample is then short-circuited at room temperature for 24 hours before the re-measurements of photocurrent responses. Figure 4.3 b shows the schematic diagram predicting the new distribution of oxygen vacancies in a BCT-Fe-0.1 ceramic after the application of an external electric field, and the expected photocurrent under the illumination. Since most of the oxygen vacancies accumulate near the bottom electrode, a weaker downward built-in electric field is resulted at the bottom ceramic-electrode interface, whereas a stronger upward built-in electric field is formed at the top interface. As a result, a net upward built-in electric field is formed and generate an upward drift current. In addition, fewer oxygen vacancies accumulate near the top electrode which is illuminated electrode, and the photo-induced electron-hole pairs are much easier to recombine [15], [58], [59], [92]. Therefore, it is expected that the induced diffusion current is weaker than that in a ceramic with oxygen vacancies accumulated near the top electrode.

(a)

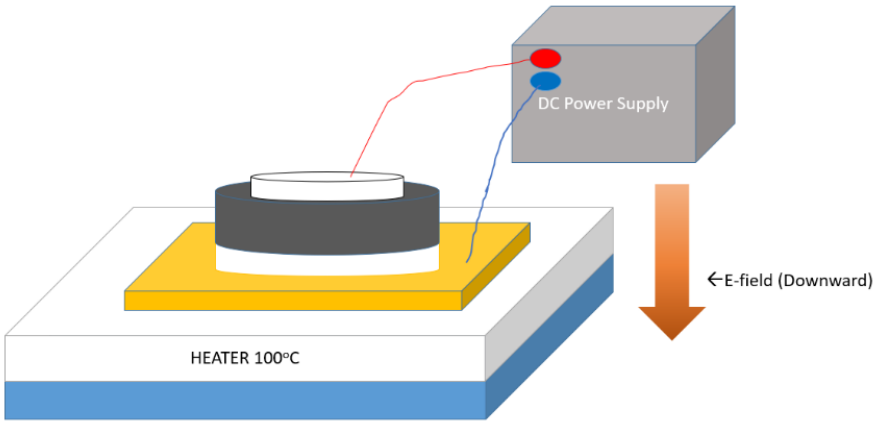

(b)

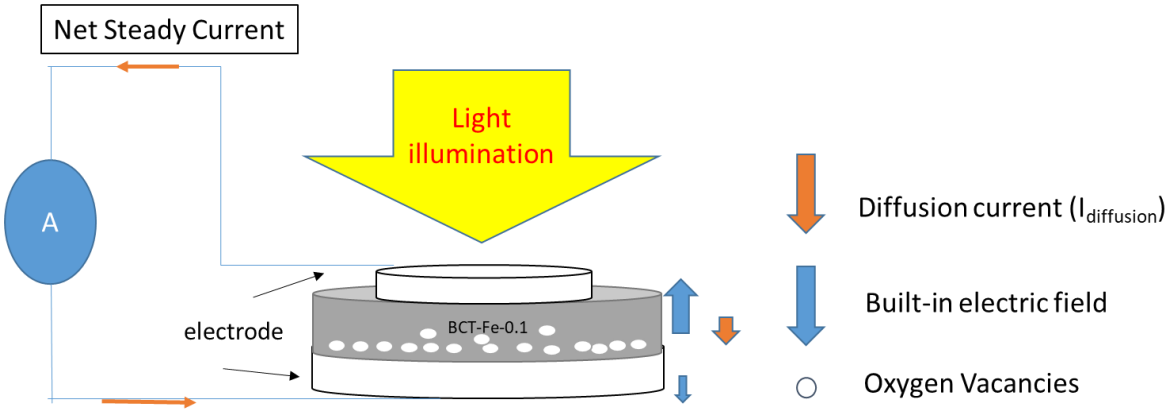

Figure 4.3 (a) Schematic diagram of the setup used for applying an external electric field. A heater was used to heat the sample to 100°C before applying the external electric field. (b) Schematic diagram predicting the new distribution of oxygen vacancies in a BCT-Fe-0.1 ceramic after the application of an external electric field and the expected photocurrent under the illumination. The orange and blue arrows indicate the direction of the diffusion current and the built-in electric field respectively.

Accordingly, different external electric fields have been applied at 100°C to the BCT-Fe-0.1 ceramics sintered in N_2, Air and O_2 for 60 minutes and their short-circuit photo-current responses have been re-measured, giving the results presented in the following sections.

4.3.1. BCT-Fe-0.1-N_2 ceramics

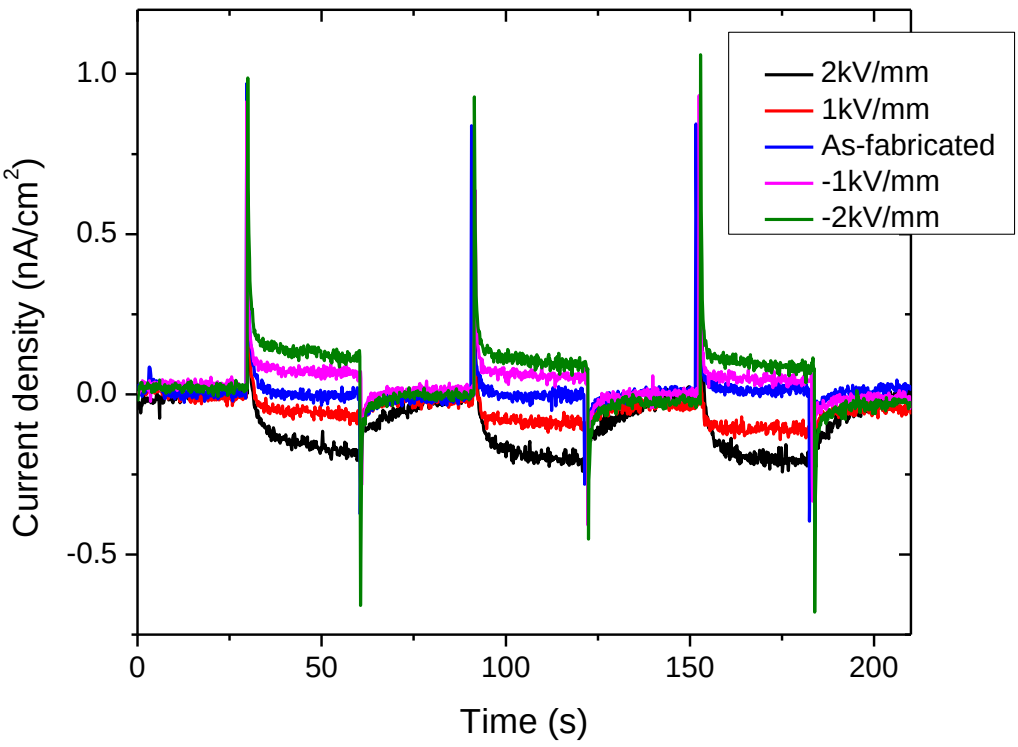

Figure 4.4 The short-circuit photocurrent of the BCT-Fe-0.1-N_2 under periodic AM 1.5G illumination.

Figure 4.4 summarizes the short-circuit photocurrent responses of the BCT-Fe-0.1-N_2 ceramics under periodic illuminations. Photocurrent peaks are observed for all the ceramics (which have been subjected to different external electric fields). It is noticed that the as-fabricated ceramic does not exhibit a steady photocurrent. However, after being

subjected to an external electric field (of any magnitude), the ceramic exhibits a steady photocurrent after a current peak during the illumination. The direction of the (steady) photocurrent is opposite to the applied electric field, i.e., if a positive or downward electric field is applied to the ceramic, a negative photocurrent flowing from the top electrode to the bottom electrode is observed. It is suggested that the distribution of the oxygen vacancies is modified by the external electric field (e.g. more oxygen vacancies will accumulate near the bottom electrodes if a positive electric field is applied). As a result, a built-in electric field arising from the uneven distribution of oxygen vacancies is formed (e.g., pointing upward) and thus leading to an upward photocurrent (e.g., flowing from the bottom electrode to the top electrode). Apparently, the magnitude of the photocurrent is dependent on the magnitude of the applied electric field.

It is interesting to note that the direction of the photocurrent can be switched during the illumination. For the ceramics subjected to a positive external electric field, the observed photocurrent exhibits a sharp positive peak first, then decreases rapidly and becomes steady with a negative value. This can be explained by considering I_{drift} and $I_{diffusion}$ [14], [15], [59], [71], [98]. As discussed in Chapter 1, the photocurrent caused by the uneven distribution of oxygen vacancies is mainly contributed by $I_{diffusion}$ and I_{drift} [15], [59], [71], [98], [99]. It is suggested that the directions and response times of $I_{diffusion}$ and I_{drift} are different [14]. Once the light is switched on, the photo-generated electrons lead to a positive diffusion current ($I_{diffusion}$). After a long illumination time, the negative drift current (I_{drift}) will become dominant [14]. As a result of the two current responses with different directions, a change in the photocurrent direction during the illumination is observed.

4.3.2. BCT-Fe-0.1-Air ceramics

The short-circuit photocurrent responses of the BCT-Fe-0.1-Air ceramics are shown in Figure 4.5. Since the magnitude of the photocurrent keeps increasing during the illumination, the illumination period for these investigations has been extended to 10 minutes.

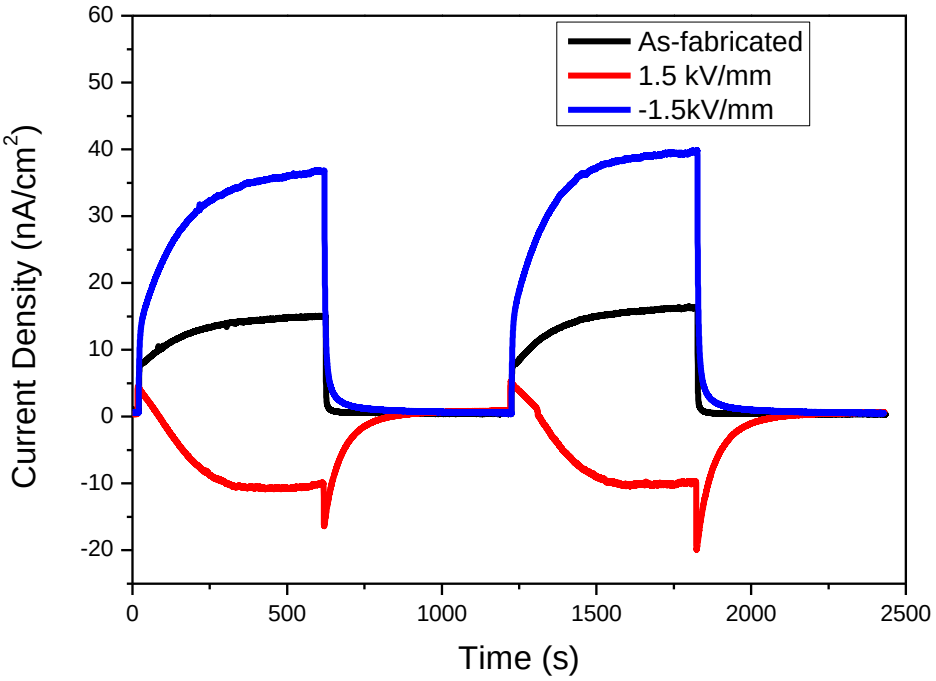

Figure 4.5 The short-circuit photocurrent of the BCT-Fe-0.1-Air under periodic AM 1.5G illumination.

Similar to BCT-Fe-0.1-N2, the photocurrent of the BCT-Fe-0.1-Air ceramics can be switched by an external electric field (which is applied to the ceramics at 100^{o}C for 60 minutes). For the as-fabricated ceramic, a positive photocurrent is observed, which first increases rapidly and then becomes almost saturated after a long illumination time. The gradual increase of the photocurrent during the illumination should be attributed to the increase in the sample temperature. Similar to the case in BCT-Fe-0.1-N_2, for the ceramic

subjected to a positive or downward electric field of 1.5 kV/mm, the photocurrent first exhibits a positive peak, and then decreases and becomes saturated at a negative value after a long illumination time. This should also be attributed to the two current responses, i.e., $I_{diffusion}$ and I_{drift}. The positive current peak is related to the positive $I_{diffusion}$ [14]. It is suggested that the oxygen vacancies inside the ceramic have migrated from near the top electrode to the bottom electrode after being subjected to the downward electric field. Therefore, a negative I_{drift} is resulted, which becomes dominant after a long illumination time [14]. The gradual increase in the magnitude of the photocurrent should be attributed to the increase in sample temperature arising from the long-term illumination. On the other hand, at the moment when the light is switched off, a negative current peak is resulted, which may also be related to $I_{diffusion}$ [14]. Since once the light is switched off, I_{drift} will disappear, and the trapped photoelectrons are assumed to be released and contribute to the negative $I_{diffusion}$ [14], [59].

An upward electric field has also been applied to the BCT-Fe-0.1-Air ceramic. It can be seen that the positive photocurrent increases by nearly two times after the treatment. Similar to BCT-Fe-0.1-N_2, our results have shown that the photocurrent response of the air-sintered ceramic can be enhanced or switched by modifying the distribution of oxygen vacancies via an external electric field.

4.3.3. BCT-Fe-0.1-O_2 ceramics

Figure 4.6 shows the short-circuit photocurrent of the BCT-Fe-0.1-O_2 ceramics. Again, as the observed photocurrent (magnitude) keeps increasing in 30 seconds due to the rise of temperature, the illumination time for the investigation has been extended to 10 minutes.

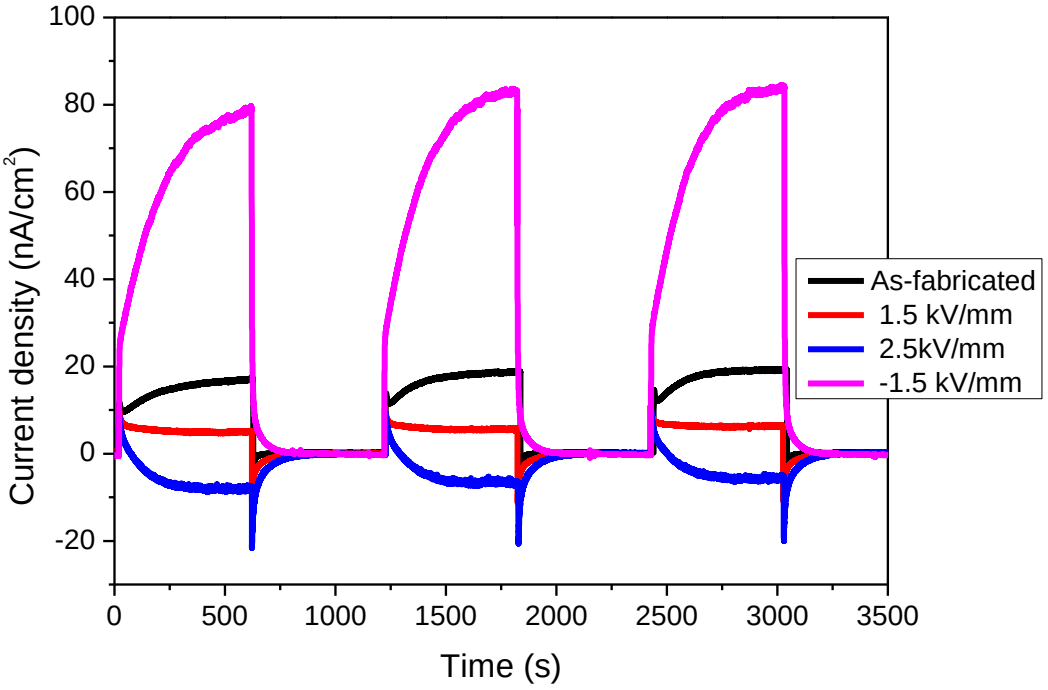

Figure 4.6 The short-circuit photocurrent of the BCT-Fe-0.1-O_2 under periodic AM 1.5G illumination.

Similar to the other two ceramics, the photocurrent of the as-fabricated ceramic exhibits a positive peak first, then increases and becomes saturated slowly due to the temperature rise. However, it can be seen that a positive or downward electric field of 1.5 kV/mm (which is the same as that used for the other two ceramics) cannot switch the observed photocurrent to negative or pointing upward. It can only decrease the magnitude of the photocurrent by about 50%. It is suggested that the BCT-Fe-0.1-O_2 ceramic contains fewer oxygen vacancies which accumulate near the top electrode of the sample. The migration of the oxygen vacancies caused by the 1.5-kV/mm electric field may not be sufficient to produce an uneven distribution with most of the oxygen vacancies accumulated near the bottom electrode. As shown in Figure 4.6, if the downward external electric field is increased to 2.5 kV/mm, the photocurrent will change gradually to negative after

exhibiting a positive peak at the beginning of the illumination. Similar to the cases in BCT-Fe-0.1-Air and BCT-Fe-0.1-N_2, it is suggested that the positive current peak is originated from $I_{diffusion}$ and the negative (steady) photocurrent is related to I_{drift} [14]. Although a larger electric field is needed, our results have shown that the direction of the photocurrent of the BCT-Fe-0.1-O_2 ceramic can also be switched.

Our results have also shown that an upward electric field of 1.5 kV/mm can also enhance the photocurrent response of the BCT-Fe-0.1-O_2 ceramic. As shown in Figure 4.6, the observed photocurrent increases by about 3 times after being subjected to the electric field. Probably because of the stronger response, photocurrent peaks are not observed at the beginning of each illumination cycle. It is suggested that I_{drift} increases and becomes dominant as more oxygen vacancies accumulate near the top electrode of the ceramic.

Our results reveal that switchable photocurrent response can be achieved in all the non-ferroelectric BCT-Fe-0.1 ceramics with symmetric electrode configuration, regardless of the sintering atmosphere, via the application of an external electric field at high temperatures such as 100°C. On the other hand, the electric field (with a suitable direction) can enhance the photocurrent response. It is suggested that at high temperatures, the mobility of oxygen vacancies increases and can migrate to near the bottom electrode when a downward electric field is applied, thus leading to a negative photocurrent response. In contrast, an upward external electric field can facilitate the migration of most of the oxygen vacancies toward the top surface, thus enhancing the photocurrent response.

4.4. Photocurrent response of the BCT-Fe-0.1 ceramics with symmetric Au electrode configuration

ITO is one of the most widely used transparent conducting oxides due to its high optical transparency and low electrical resistivity. However, a few researchers have reported that it may not be a stable electrode due to its sensitivity to the deposition conditions, such as temperature and annealing atmosphere [100]–[106]. The conductivity and transparency of ITO are highly dependent on its oxygen vacancy content [99], [103], which can be controlled by modifying the deposition and annealing conditions [101], [102], [105], [106]. A high oxygen vacancy content is beneficial for improving the electrical conductivity of ITO, but not for the optical transparency. It has also been shown that a strong electric field can degrade its conductivity [107]. In this work, a strong external electric field is applied to the BCT-Fe-0.1 ceramics at 100^{o}C, and thus it is important to confirm if the different current responses of the ceramics after subjected to an external electric field are originated from the modification of the oxygen vacancy distribution or the characteristics of the ITO electrodes.

It is supposed that Au is more stable at high temperatures and electric fields. Furthermore, Au thin films are semi-transparent and have been used as top electrodes for their photocurrent devices [59]. In this work, 40-nm thick gold (Au) thin films have been used as the top and bottom electrodes for the BCT-Fe-0.1 ceramics for investigating the photocurrent responses.

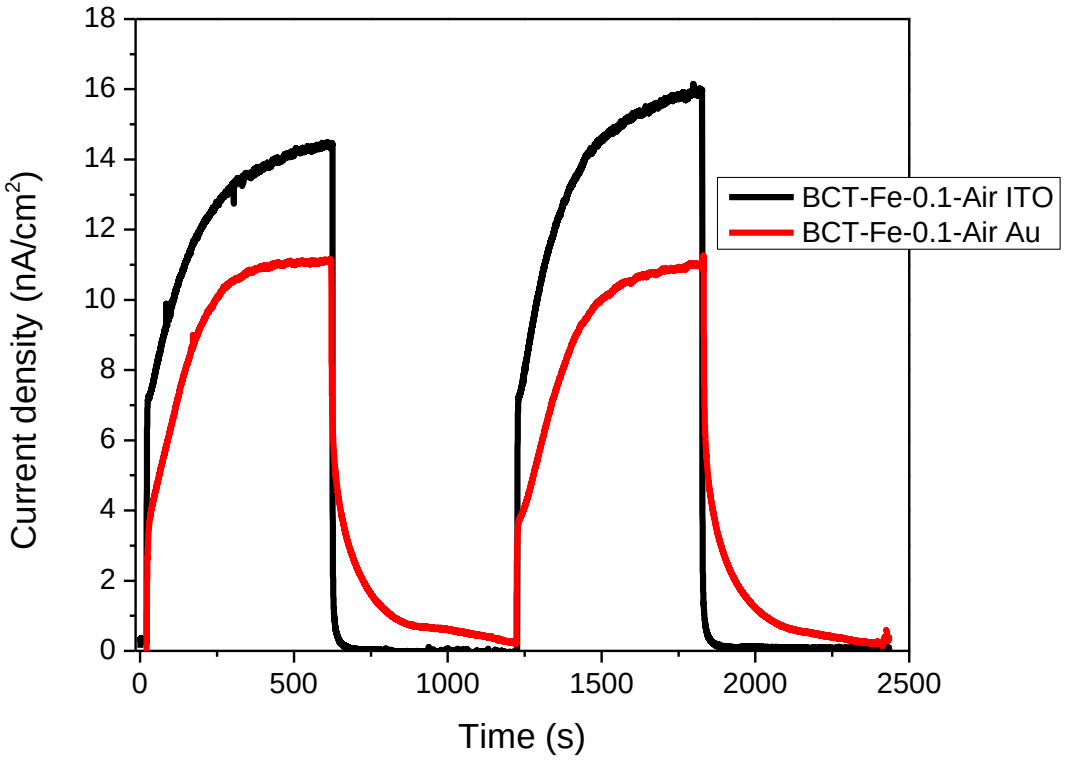

Figure 4.7 The short-circuit photocurrent of BCT-Fe-0.1-Air ceramics with symmetric ITO and Au electrode under periodic AM 1.5G illumination.

Figure 4.7 shows the photocurrent responses of the as-fabricated BCT-Fe-0.1-Air samples with symmetric Au and ITO electrode configurations. It can be seen that both the ceramics exhibit a positive photocurrent under illumination. The observed photocurrent keeps increasing as heat is generated during the illumination. The photocurrent of the ceramic with Au electrodes is weaker than that of the ceramic with ITO electrodes. This should be attributed to the lower transmittance of the Au electrode as compared to the ITO electrode (Figure 2.2).

The photocurrent responses of the BCT-Fe-0.1 ceramics sintered in N_2, O_2 and air have also been studied. Similar to the ceramics with ITO electrodes, different external

electric fields have also been applied at 100°C to the ceramics with Au electrodes for 60 minutes. The observed short-circuit photocurrent of the BCT-Fe-0.1 ceramics (with Au electrode) will be discussed in the following sections.

4.4.1. BCT-Fe-0.1-N_2 ceramics

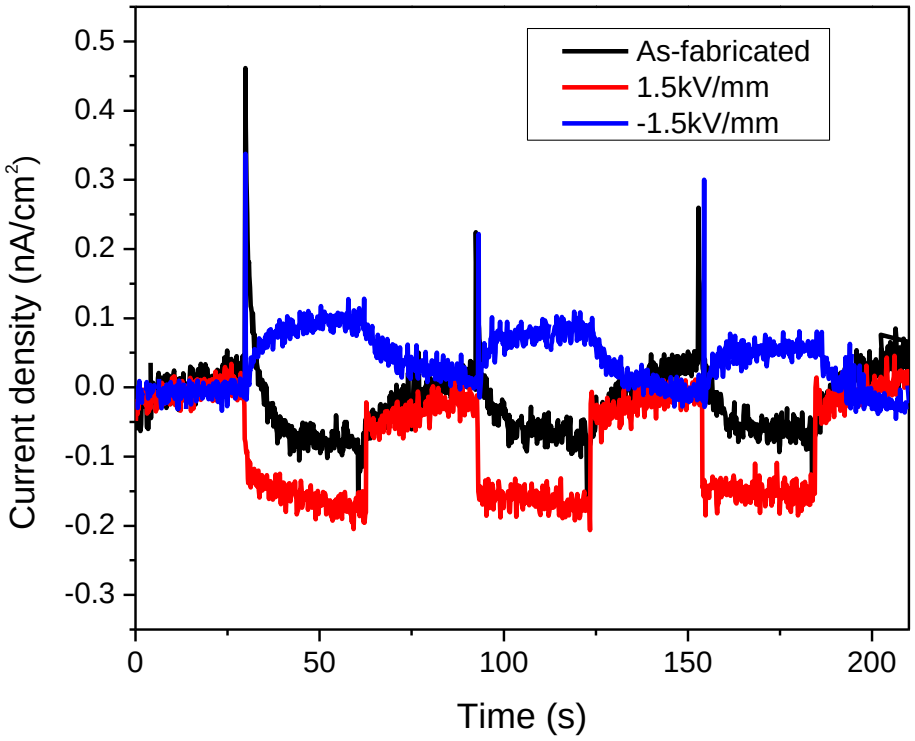

Figure 4.8 The short-circuit photocurrent of BCT-Fe-0.1-N_2 ceramics with Au electrodes under periodic AM 1.5G illumination.

The photocurrent responses of the BCT-Fe-0.1-N_2 ceramics are shown in Figure 4.8. Similar to the ceramics with ITO electrodes, current peaks are observed. However, probably because of the low transmittance of the Au electrode, the photocurrent is very weak. As also shown in Figure 4.8, a negative photocurrent is observed for the ceramic after being subjected to an electric field of 1.5 kV/mm (i.e., downward). It is suggested that the

oxygen vacancies have migrated from near the top surface to the bottom surface of the ceramic after being subjected to the downward electric field. As discussed in Chapter 4.2, diffusion current ($I_{diffusion}$) and drift current (I_{drift}) are the major contributions to the photocurrent response of the ceramics. It is suggested that the accumulation of oxygen vacancies will create an internal electric field for I_{drift}. After being subjected to a downward electric field, the oxygen vacancies will migrate to the bottom side of the ceramic, and the observed negative steady photocurrent is related to I_{drift} caused by the accumulation of oxygen vacancies. It is suggested that the current peaks are related to $I_{diffusion}$. Because of the lower transmittance, the amounts of photo-induced electrons in the sample with Au electrodes will be smaller. As a result, I_{drift} will dominate the photocurrent response of the sample and the current peaks are too weak to be observed.

On the other hand, an upward electric field (i.e., -1.5 kV/mm) is subjected to the BCT-Fe-0.1-N_2 ceramic. Current peaks and positive steady photocurrent are observed. It is suggested that more oxygen vacancies will be accumulated near the top surface of the ceramic. Once the illumination is switched on, a positive current peak is observed. It is suggested that $I_{diffusion}$ is responsible for the positive current peaks [14]. As the illumination is switched on, electron-hole pairs are generated and the photo-induced electrons will be trapped by the oxygen vacancies. The remaining holes will then induce a positive $I_{diffusion}$. During the illumination, I_{drift} will become dominant and a positive steady current has resulted.

4.4.2. BCT-FE-0.1-O_2 ceramics

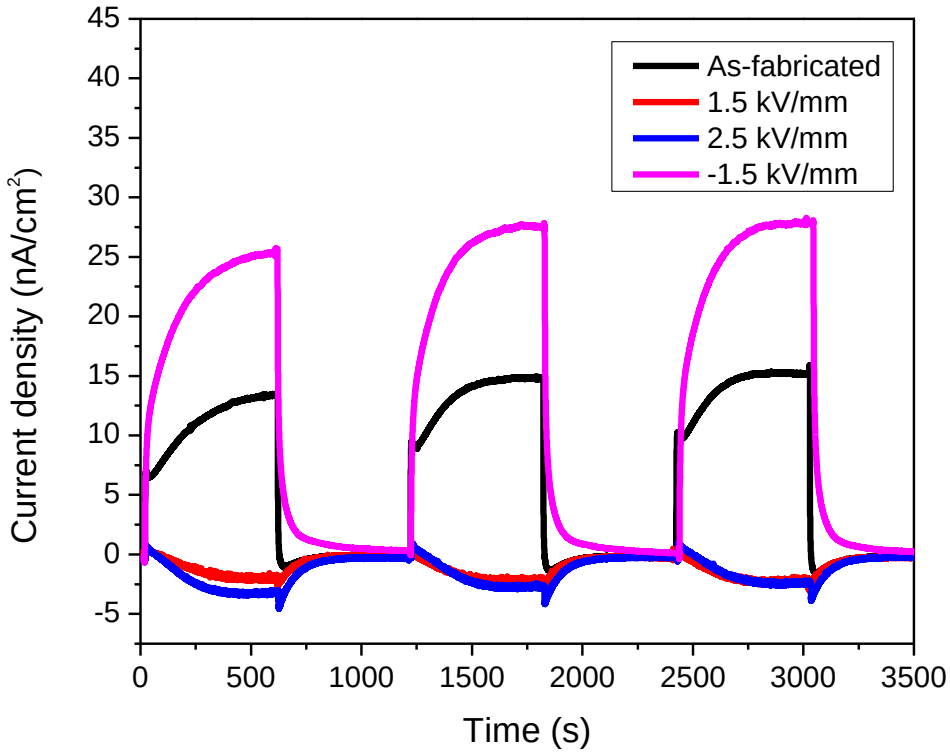

Figure 4.9 The short-circuit photocurrent of BCT-Fe-0.1-O_2 ceramics with Au electrodes under periodic AM 1.5G illumination.

Figure 4.9 shows the short-circuit photocurrent of the BCT-Fe-0.1-O_2 ceramics with Au electrodes. In general, the ceramics with Au electrodes exhibit similar photocurrent responses to their counterparts with ITO electrodes, and similar effects of the external electric fields, both downward and upward, on the responses are also observed. For the as-fabricated ceramic, small current peaks and photocurrent of which the magnitude keeps increasing during the illumination are observed. After being subjected to a downward electric field of 1.5 kV/mm, both the current peaks and steady photocurrent change the direction, which should be attributed to the re-distribution of the oxygen vacancies as

discussed in Chapter 4.3 for its counterpart with ITO electrodes. However, it is noted that the negative photocurrent is weak, and cannot be enhanced significantly by increasing the downward field to 2.5 kV/mm. An electrical breakdown will occur if a stronger downward electric field is applied. Further investigations are required for studying the reasons for the much weaker photocurrents for the ceramics with Au electrodes as compared to their counterparts with ITO electrodes. On the other hand, an upward electric field of 1.5 kV/mm can enhance the response significantly, and the changes, including the disappearance of the current peaks, are similar to its counterpart with ITO electrodes.

4.4.3. BCT-Fe-0.1-Air ceramics

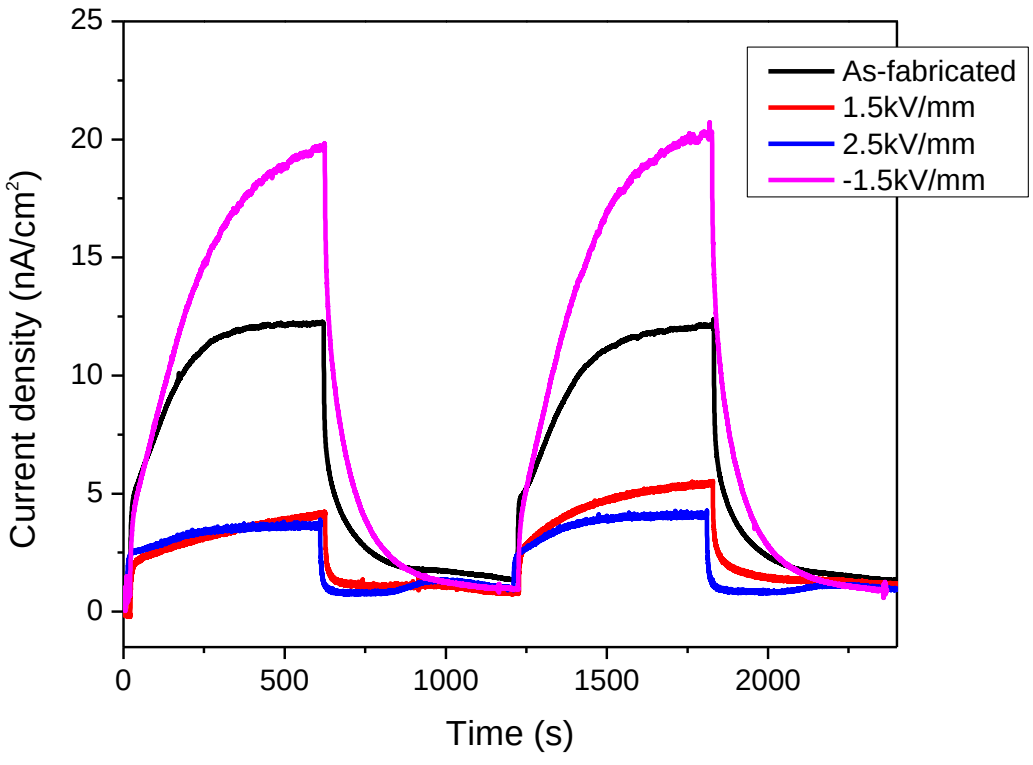

Figure 4.10 The short-circuit photocurrent of BCT-Fe-0.1-Air ceramics with Au electrodes under periodic AM 1.5G illumination.

Figure 4.10 shows the photocurrent responses of the BCT-Fe-0.1-Air ceramics with Au electrodes. The as-fabricated ceramic exhibits similar photocurrent responses to its counterpart with ITO electrodes. After being subjected to an upward electric field of 1.5 kV/mm, the photocurrent increases by about two times, which is suggested to be caused by the accumulation of more oxygen vacancies near the top surface of the ceramic. However, unlike its counterpart with ITO electrodes, the photocurrent of the ceramic cannot be switched to the opposite direction after being subjected to a downward electric field of 1.5 kV/mm or 2.5 kV/mm. It is only reduced by about 75%, and the reduction is independent of the field strength. It is suggested that the electric field may not be strong enough to migrate enough amount of oxygen vacancies to near the bottom surface of the ceramic for producing a negative photocurrent.

Our results show that the as-fabricated BCT-Fe-0.1 ceramics with ITO and Au electrodes exhibit similar photocurrent responses. Because of the higher transmittance, the observed photocurrent of the ceramic with ITO is stronger. For both the ceramics, the photocurrent can be enhanced by a downward electric field applied at 100^{o}C. It is suggested that the enhancement is originated from the accumulation of more oxygen vacancies near the top surface of the ceramic. Except for the BCT-Fe-0.1-Air ceramic with Au electrodes, the photocurrent of all the other ceramics, regardless of the sintering atmosphere and electrode, can be switched to the opposite direction by an upwards electric field applied at 100°C.

4.5. Conclusions

The photocurrent responses of the BCT-Fe-0.1 non-ferroelectric ceramics (sintered in air, N_2 and O_2) with symmetric ITO or Au electrode configuration have been investigated.

The photocurrent responses of the BCT-Fe-0.1 ceramics with ITO electrodes have first been investigated. Photocurrent responses are observed for all the BCT-Fe-0.1 ceramics. During the 30-second solar light illumination, the observed average photocurrent of the BCT-Fe-0.1-Air and BCT-Fe-0.1-O_2 ceramics are 4.8 nA/cm^2 and 6.9 nA/cm^2, respectively. On the other hand, the BCT-Fe-0.1-N_2 ceramic exhibits only sharp current peaks (0.75 nA/cm^2) at the moment when the illumination source is switched on/ off, but no steady photocurrent during the illumination. It is suggested that the reduction of the steady photocurrent is caused by the non-accumulated oxygen vacancies in the ceramic. The BCT-Fe-0.1-N_2 ceramic contains the most oxygen vacancies which can trap the photo-induced electrons. As a result, because of the charge recombination, the photocurrent generated by the BCT-Fe-0.1-N_2 is the lowest (Only current peaks are observed). In contrast, the BCT-Fe-0.1-Air and BCT-Fe-0.1-O_2 ceramics contain fewer oxygen vacancies, and thus their photocurrents are larger.

Both upward and downward electric field of 1.5 kV/mm has then been applied to all the BCT-Fe-0.1 ceramics respectively. No changes in photocurrent responses are observed for all the ceramics if the electric field is applied at room temperature. However, if it is applied at 100^{o}C, both the magnitude and direction of the photocurrent are changed. It is suggested that the oxygen vacancies inside the ceramics can migrate under an external electric field, and the photocurrent responses of the BCT-Fe-0.1 ceramics are dependent on the distribution of the oxygen vacancies.

The photocurrent responses of the ceramics with Au electrodes have also been investigated. Probably because of the lower transmittance of Au, the photocurrents of the ceramics are generally lower than those of their counterparts with ITO electrodes. Switchable photocurrent responses are also observed for the BCT-Fe-0.1-O_2 and BCT-Fe-0.1-N_2 ceramics. For the BCT-Fe-0.1-Air ceramic, only the magnitude of the photocurrent can be modified by an external electric field. Nevertheless, our results have shown that the observed switchable photocurrent responses are originated from the distribution of oxygen vacancies in the ceramics.

Chapter 5. Photocurrent Response of BCT-Fe-0.025 Ceramics

5.1. Introduction

In Chapter 3, it has been confirmed that the BCT-Fe-0.025 ceramic is ferroelectric at room temperature. Moreover, the sintering atmospheres (such as O_2, N_2 and air) will affect the ferroelectric properties of the ceramic. When the ceramics are sintered in O_2, N_2 and air, respectively, their saturated polarizations P_s vary from ~10 μC/cm^2 to ~18 μC/cm^2, while the remnant polarizations P_r varies from ~2.5 μC/cm^2 to ~4.5 μC/cm^2. These differences may contribute to different photocurrent responses of the BCT-Fe-0.025 ceramics sintered in different atmospheres.

In this chapter, the photocurrent responses of the BCT-Fe-0.025 ceramics sintered in air, N_2 and O_2 are presented. The I_{sc} of the ceramics under A.M. 1.5 solar illumination was examined for exploring the photocurrent response. Unlike BCT-Fe-0.1 ceramics discussed in Chapter 4, the BCT-Fe-0.025 ceramic is ferroelectric and can be poled by an external electric field. The BCT-Fe-0.025 ceramics were then poled under an electric field of 1 kV/mm at room temperature and their photocurrent responses were compared.

As discussed in Chapter 1, researchers have reported that defects such as oxygen vacancies can be a dominant factor in the photovoltaic response in ferroelectric photovoltaic devices [12], [14], [59]. They have suggested that the accumulation of oxygen vacancies near the ceramic-electrode interface will reduce the barrier height at the interface [14], [59]. As a result, a Schottky-like barrier is formed, which contributes a build-in electric field for separating the photo-generated electron-hole pairs [12], [14], [59]. They have also suggested that the distribution of oxygen vacancies can be modified by a high

external electric field. To investigate the influence of the distribution of defects (oxygen vacancies) on the photovoltaic response of the ferroelectric ceramics, an electric field of 1 kV/mm was applied to the BCT-Fe-0.025 ceramics at 100^{o}C for poling and re-distributing the oxygen vacancies inside the ceramics. The photocurrent responses of the BCT-Fe-0.025 ceramics were then studied for investigating the effects.

5.2. Photocurrent response of BCT-Fe-0.0225 ceramics poled at room temperature

The photocurrent responses of the as-fabricated and poled BCT-Fe-0.025 ceramics are presented. The schematic diagram of the poling process and I_{sc} measurement are shown in Figure 5.1. In this work, a downward poling field is defined as a positive electric field and a downward current (from the top electrode to the bottom electrode) is defined as a positive current. As shown in Figure 5.1, BCT-Fe-0.025 ceramics with symmetric Au electrodes were used for the measurements. It is suggested that the use of symmetric electrodes can eliminate the effect caused by Schottky barriers formed at the ceramic-electrode interface.

(a)

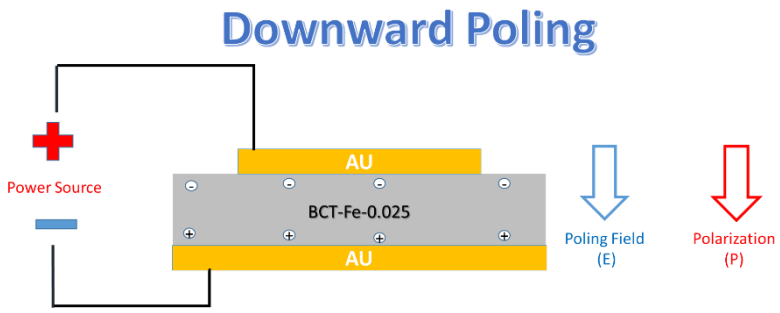

(b)

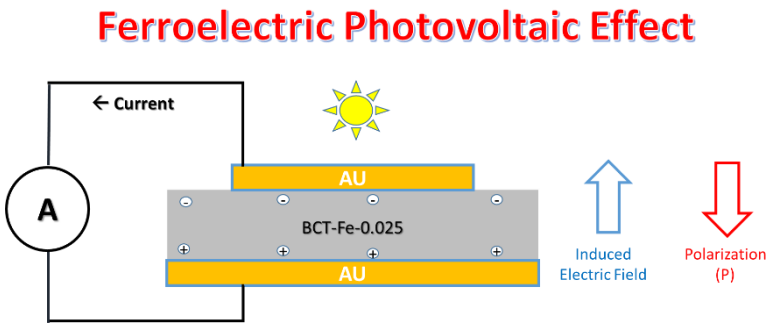

Figure 5.1 The schematic diagram of (a) the downward poling process (positive poling) and (b) the current direction for the ferroelectric photovoltaic process after poling in a positive electric field.

In addition, as discussed in Chapter 4, the observed photocurrent of the BCT-Fe-0.1 ceramics is not affected by the application of an electric field of 2.5 kV/mm at room temperature. This suggests that the distribution of oxygen vacancies in the BCT-Fe-0.025 ceramics will not be changed by the electric field of 1 kV/mm applied at room temperature. Therefore, it is believed that the net polarization of the BCT-Fe-0.025 ceramics resulting from the poling field of 1 kV/mm at room temperature is the major cause of the observed photocurrent response.

The BCT-Fe-0.025-Air (i.e., sintered in Air) ceramic is used as an example to demonstrate the ferroelectric photovoltaic effect. Figure 5.2 shows the short-circuit photocurrent

I_{sc} of the as-fabricated and poled BCT-Fe-0.025-Air ceramics under periodic AM 1.5G illumination (i.e., the illumination is switched on for 30 seconds and then off for 30 seconds). Since the as-fabricated BCT-Fe-0.025-Air ceramic exhibits a zero net remnant polarization, there is no internal field to drive the photo-induced holes and electrons, and thus almost no current response is observed for the ceramic. On the other hand, the photocurrent responses of the poled BCT-Fe-0.025-Air ceramics can be observed. A sharp negative/positive current peak is observed at the moment when the illumination is switched on / off. It is suggested that the current peaks are dominated by the pyroelectric effect. As discussed in Chapter 1.2, the pyroelectric effect is that a material releases electric charges due to a temperature change. Moreover, the magnitude of the current is dependent on the temperature change. When the illumination is switched on, there will be a sudden increase in temperature which leads to a pyroelectric current. A weak negative steady current is observed after the current peak. It is believed that the ferroelectric photovoltaic effect is the major contributor to the steady current. As the illumination is kept on, the temperature of the ceramic will keep on increasing at a lower rate or become stable. Therefore, the pyroelectric effect will become weak, and the ferroelectric photovoltaic effect will be the dominant effect. Similarly, when the illumination is switched off, there will be a sudden decrease in temperature which leads to a positive pyroelectric current. Our results are consistent with previous research in which sharp pyroelectric current peak and steady current response have been observed in ferroelectric photovoltaic devices [10], [33].

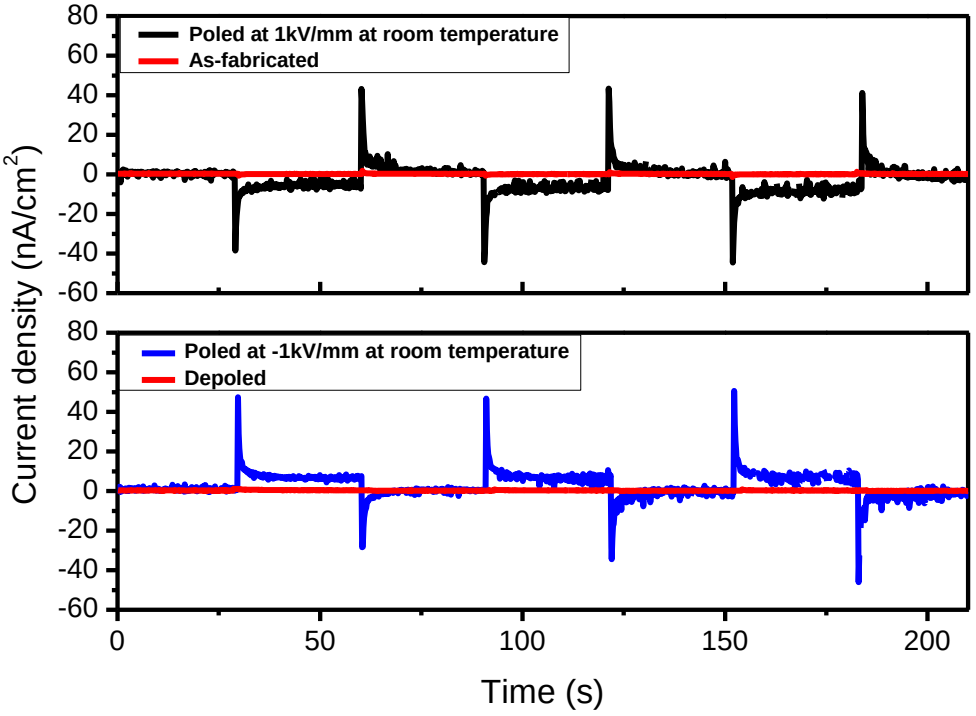

Figure 5.2 The short-circuit photocurrent of the as-fabricated, poled (1kV/mm and -1kV/mm) and depoled BCT-Fe-0.025-Air ceramic under AM 1.5G illumination.

One of the characteristics of the ferroelectric photovoltaic effect is the switchable photocurrent response. The switchable photocurrent response of the BCT-Fe-0.025-Air ceramic is also presented in Figure 5.2. After the measurements, the poled ceramic has been annealed at 100^{o}C for 24 hours for depolarization. It can be seen that, after the de-polarization process, the photocurrent response of the ceramic disappears.

After the depolarization process, the BCT-Fe-0.025 ceramic was poled under an electric field of -1 kV/mm (i.e., upward poling) at room temperature. Similar to the downward poled ceramic, both the current peak and steady photocurrent, but in a reverse direction, are observed in the upward-poled BCT-Fe-0.025 ceramic. This provides strong evidence that the photocurrent response of the ceramic is strongly dependent on its polarization.

No photocurrent response is observed in the as-fabricated or de-poled ceramics. In addition, the direction of the photocurrent can be switched by reversing the polarization of the ceramics. The switchable and polarization-dependent photocurrent response in the BCT-Fe-0.025 ceramics is thus demonstrated.

The switchable photocurrent responses of the BCT-Fe-0.025-N2 and BCT-Fe-0.025-O2 (i.e., sintered in N_2 and O_2, respectively) ceramics have also been studied. The observed I_{sc} for the downward-poled (1 kV/mm) ceramics under periodic illumination are shown in Figure 5.3.

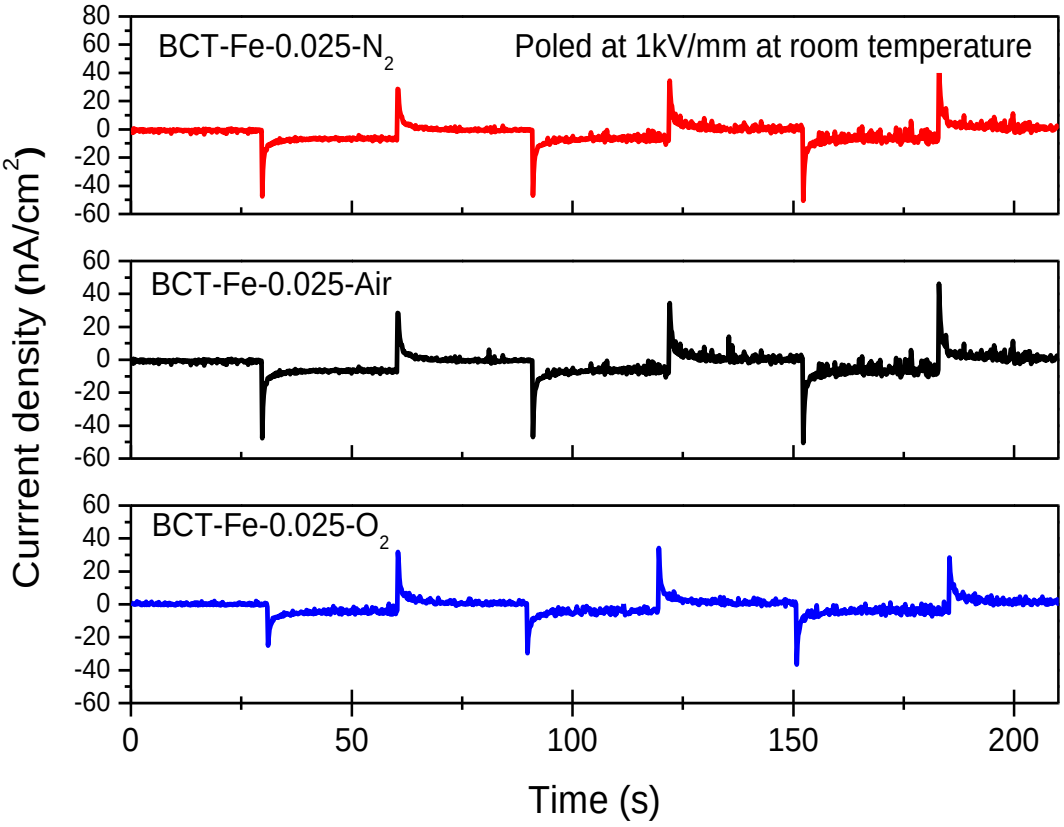

Figure 5.3 The short-circuit photocurrent of the poled (1kV/mm) BCT-Fe-0.025 ceramics sintered in N_2, Air and O_2.

As shown in Figure 5.3, all the BCT-Fe-0.025 ceramics exhibit both the pyroelectric current peak and steady photocurrent. The BCT-Fe-0.025-Air and BCT-Fe-0.025-N_2 ceramics exhibit similar pyroelectric current peaks (~48 nA/cm^2 and ~47 nA/cm^2, respectively) and steady photocurrents (~6.7 nA/cm^2 and ~6.4 nA/cm^2), while both of them for the BCT-Fe-0.025-O_2 ceramic are lower (~ 30 nA/cm^2 and ~ 4.4 nA/cm^2, respectively). The variations in the pyroelectric current and photocurrent should be attributed to the lower remnant polarization P_r of the BCT-Fe-0.025-O2 ceramic. It is suggested that the magnitudes of the pyroelectric current and ferroelectric photocurrent are dependent on the remnant polarization of the material. As shown by the P-E loops discussed in Chapter 3.2, the remnant polarization P_r of the BCT-Fe-0.025-O_2 ceramic is the lowest (~2.5 μC/cm^2), while those of the BCT-Fe-0.025-Air and BCT-Fe-0.025-N_2 ceramics are similar (~4.5 μC/cm^2 and ~3.8 μC/cm^2, respectively).

5.3. Photocurrent response of BCT-Fe-0.025 ceramics poled at 100°C

In Chapter 1 and Chapter 4, the influence of oxygen vacancies on the photocurrent response in ferroelectric photovoltaic devices is introduced. For example, if the oxygen vacancies are accumulated near one of the ceramic-electrode interfaces, the Schottky barrier height at that interface will be reduced. As a result, asymmetric Schottky barriers have resulted even in the ceramics with the same top and bottom electrodes (or symmetric electrode configuration). A net built-in electric field is thus created to drive and separate the photo-induced electron-hole pairs. In addition, the accumulated oxygen vacancies will trap the photo-induced electrons, thus preventing them from recombining with photo-induced holes [11], [90], [108]. As a result, the remaining photo-induced holes will produce an additional diffusion current. It is then suggested that the photocurrent response of the ceramics can be modified or controlled by changing or adjusting the distribution of

oxygen vacancies. As discussed in Chapter 4.2, the photocurrent response of the non-ferroelectric BCT-Fe-0.1 ceramics can be modified (enhanced/ suppressed/ switched) by a high electric field applied at 100^{o}C. The modification is suggested to result from the change or adjustment of the distribution of oxygen vacancies inside the ceramic (e.g. more oxygen vacancies are accumulated near the bottom electrode). Therefore, to study the influence of the distribution of oxygen vacancies inside the ceramic on the photocurrent response of the BCT-Fe-0.025 ceramics, the poling temperature is increased to 100^{o}C. Since the T_c of the BCT-Fe-0.025 ceramics is ~55^{o}C, the poling field is removed after the ceramic is cooled down to below its T_c. Figure 5.4a shows a schematic diagram of the downward poling process for the BCT-Fe-0.025 ceramic and the resultant distribution of oxygen vacancies. A schematic diagram of the photocurrent generated by the coupling effect of oxygen vacancies and ferroelectric photovoltaic effect is illustrated in Figure 5.4b.

(a)

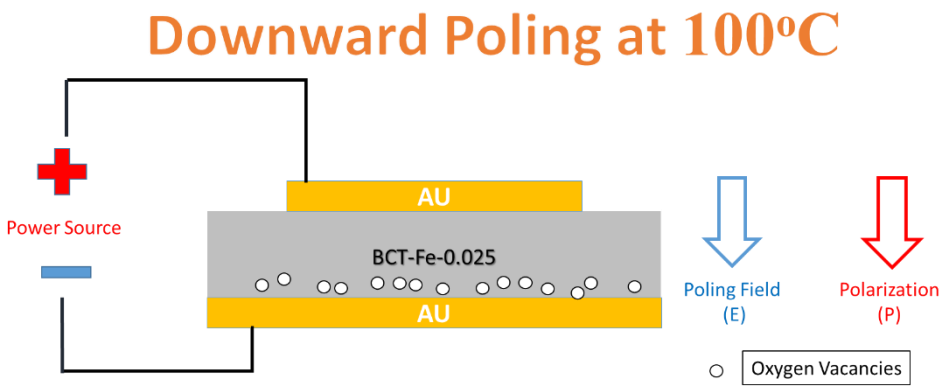

(b)

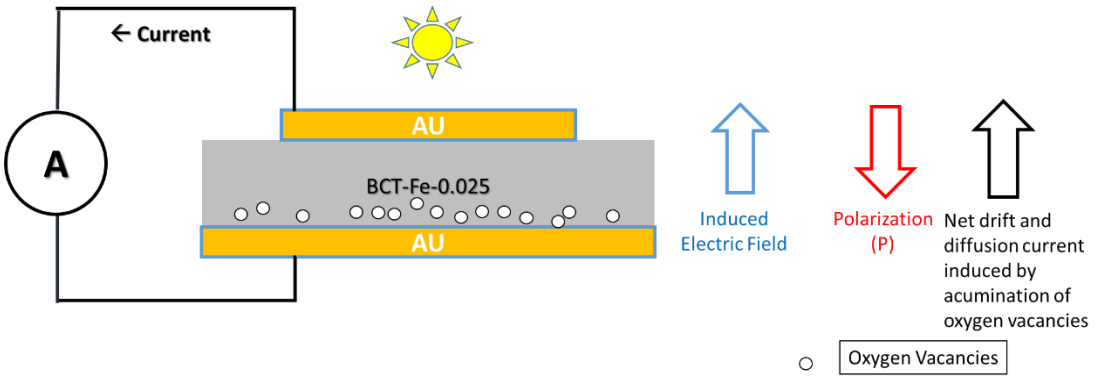

Figure 5.4 (a) The schematic diagram of the downward poling process at 100°C for the BCT-Fe-0.025 ceramic and the resultant distribution of oxygen vacancies. (b) The schematic diagram of the photocurrent generated by the coupling effect of oxygen vacancies and ferroelectric photo-current effect BCT-Fe-0.025-N_2 ceramics

5.3.1. BCT-Fe-0.025-N_2 ceramics

Figure 5.5 illustrates the photocurrent response of the BCT-Fe-0.025-N_2 ceramics poled under an electric field of 1 kV/mm at 100°C. As shown in Figure 5.3, when the BCT-Fe-0.025-N_2 ceramic is poled at room temperature, once the illumination is switched on/off, a negative/positive sharp current peak is observed. It is believed that the current peaks are caused by the pyroelectric effect. However, as shown in Figure 5.5, current peaks do not appear in the ceramic poled at 100°C.

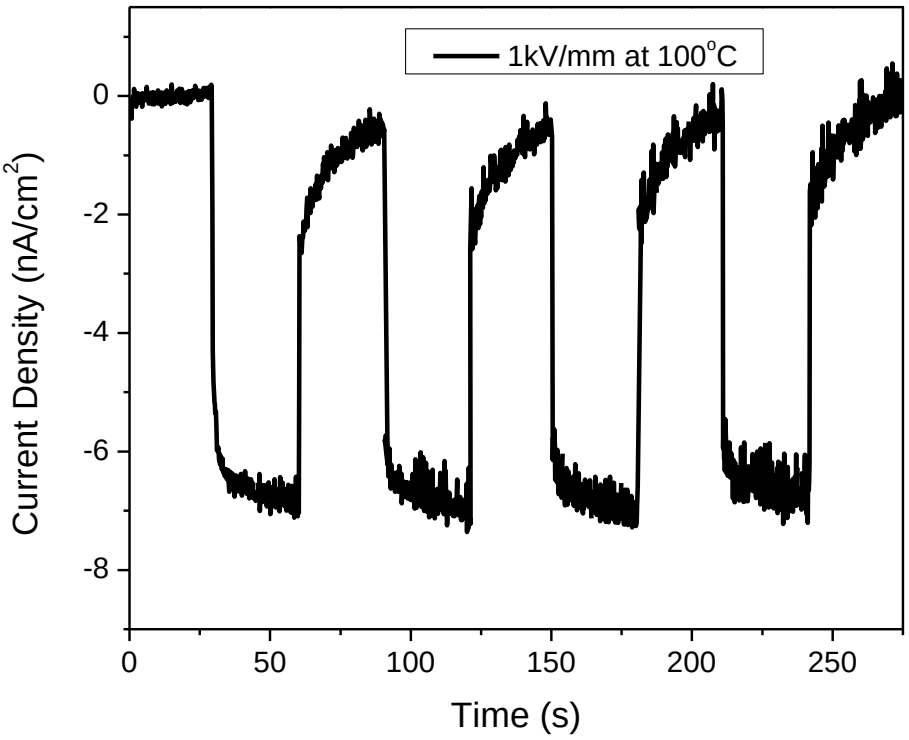

Figure 5.5 The short-circuit photocurrent of the poled BCT-Fe-0.025-N_2 ceramics after poling (1kV/mm) at 100°C.

It has been shown that the distribution of oxygen vacancies may affect the magnitude and direction of the pyroelectric current [108]. As the BCT-Fe-0.025-N_2 ceramic should

contain more oxygen vacancies, it is anticipated that the oxygen vacancies in the ceramic may migrate and re-distribute after the polling process and then affect the pyroelectric response of the ceramic [108]. However, further experimental works are needed for investigating the mechanism for the disappearance of the pyroelectric currents.

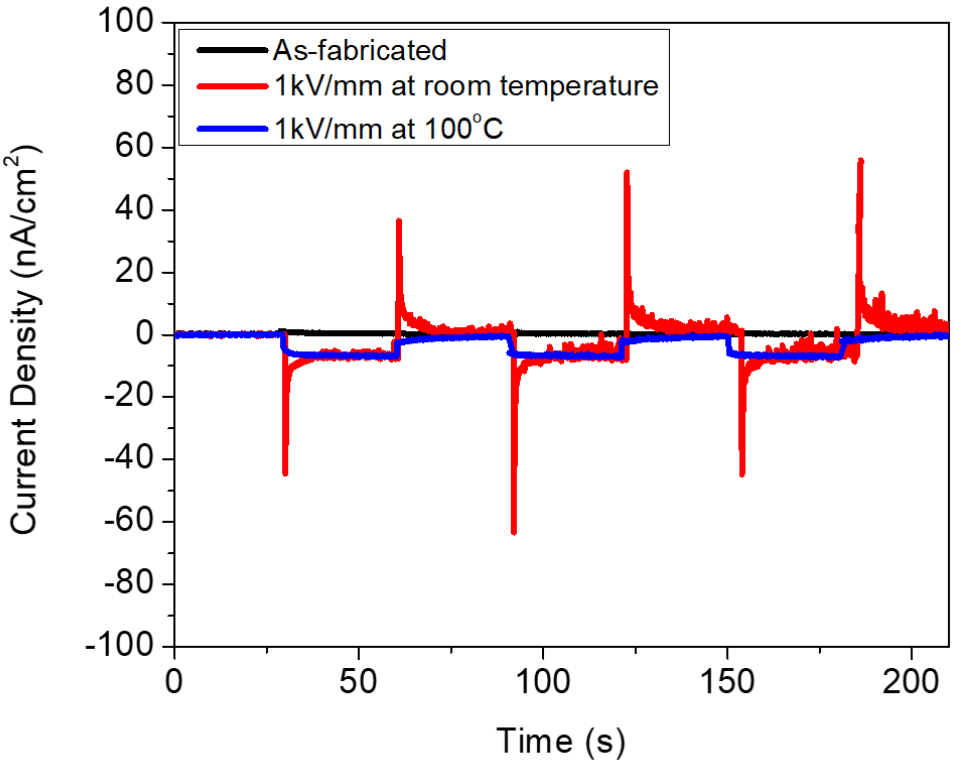

Figure 5.6 The short circuit photocurrent of the as-fabricated, poled at room temperature and 100°C BCT-Fe-0.025-N_2 ceramics.

Figure 5.6 compares the short-circuit photocurrent responses of the ceramics under different conditions (i.e., as-fabricated, poled at room temperature and poled at 100°C). It is noticed that the steady photocurrent of the ceramics poled at room temperature and 100°C have similar values. The only difference between their responses is the disappearance of the current peaks in the ceramic poled at 100°C. It is anticipated that the oxygen vacancies in the BCT-Fe-0.025-N_2 ceramics will be more evenly distributed. Similar to

the case of the BCT-Fe-0.1-N_2 ceramic discussed in Chapter 4, the non- accumulated oxygen vacancies will not contribute to the photocurrent response. It is also difficult to migrate and accumulate a large number of oxygen vacancies to one side of the ceramics. It is thus suggested that the photocurrent response of the BCT-Fe-0.025-N_2 ceramic is not significantly improved by the poling at 100°C.

5.3.2. BCT-Fe-0.025-O_2 ceramics

The photocurrent responses of the BCT-Fe-0.025-O_2 ceramics under different conditions (i.e., as-fabricated, poled at room temperature and poled at 100°C) are shown in Figure 5.7. It can be seen that the current peaks of the ceramic poled at 100°C are slightly lower than those of the ceramics poled at room temperature.

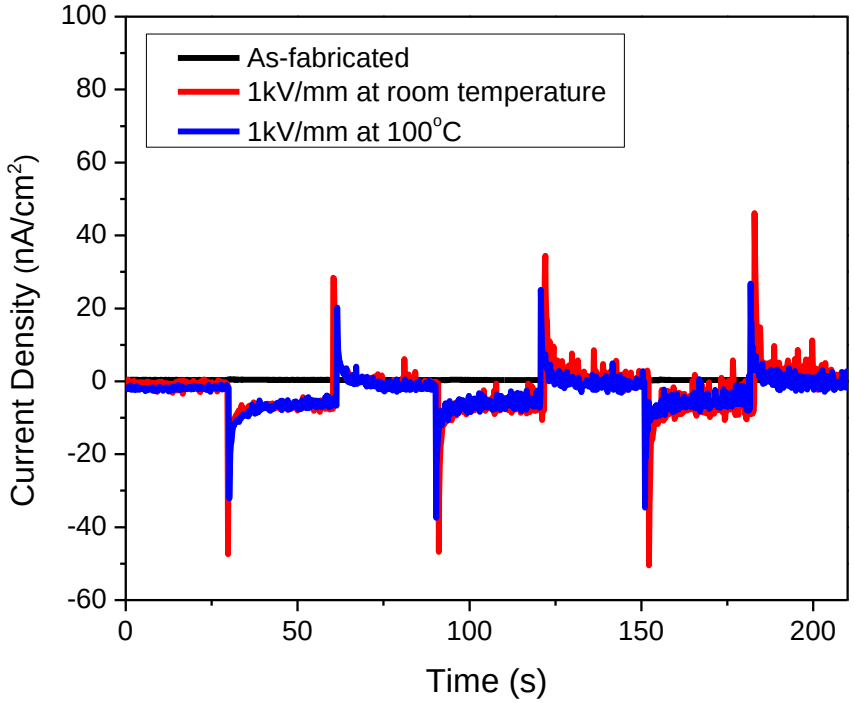

Figure 5.7 The short-circuit photocurrent of the as-fabricated, poled (room temperature and 100°C) BCT-Fe-0.025-O_2 ceramics.

It is also noted that the steady photocurrent response of the ceramic is not enhanced by the poling temperature; i.e., both the ceramics poled at room temperature and 100°C exhibit similar steady photocurrents. It is suggested that the BCT-Fe-0.025 ceramics contain fewer oxygen vacancies than the BCT-Fe-0.1 ceramics due to a lower doping content of Fe^{3+} level [75]. In addition, the generation of oxygen vacancies will be suppressed by the oxygen-rich sintering atmosphere [51]. Therefore, the oxygen vacancy content of the BCT-Fe-0.025-O_2 ceramic should be low, which limits the enhancement of the photocurrent response.

5.3.3. BCT-Fe-0.025-Air ceramics

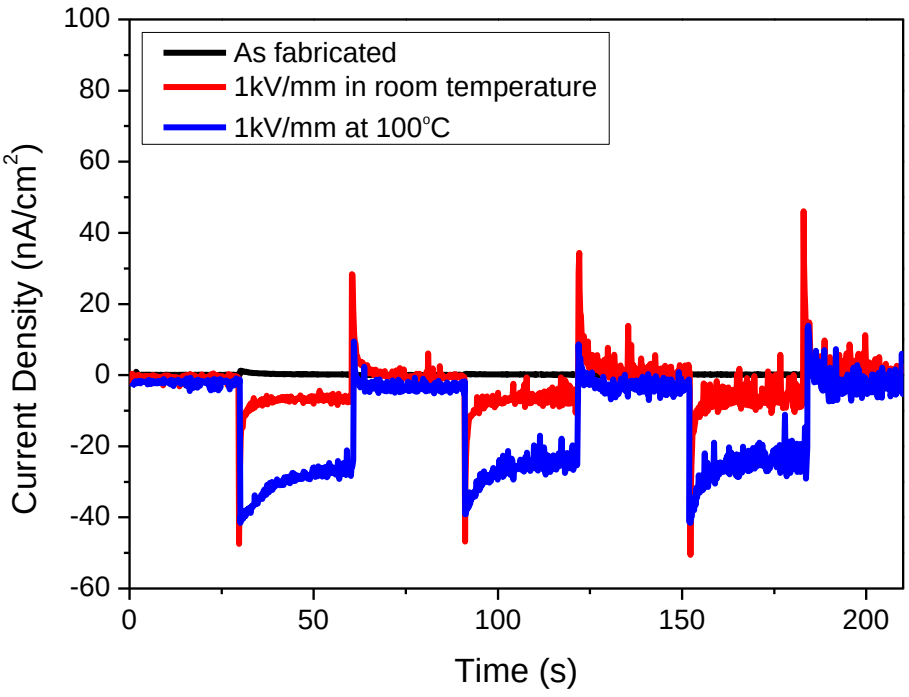

Figure 5.8 The short-circuit photocurrent of the as-fabricated, poled at 1 kV/mm (room temperature and 100°C) BCT-Fe-0.025-Air ceramics.

The photocurrent response of the BCT-Fe-0.025-Air ceramics under different conditions (i.e., as-fabricated, poled at room temperature and poled at 100°C) are shown in Figure 5.8. It can be seen that the pyroelectric current peaks of the ceramic poled at 100°C are lower than those of the ceramic poled at room temperature. It is anticipated that the pyroelectric current peak is reduced due to the accumulation of oxygen vacancies [11], [90], [108]. Once the illumination is switched on, a negative photocurrent peak is resulted. In contrast, when the illumination is switched off, a small positive photocurrent peak is resulted. It is noticed that after switching off the illumination, the positive current peak of the ceramic poled at 100°C is much weaker. It is suggested that the oxygen vacancies accumulated near the bottom electrode after the poling process at 100°C. Similar to the case of BCT-Fe-0.1-Air ceramics discussed in Chapter 4, the oxygen vacancies accumulated near the bottom electrode may generate a negative diffusion current which opposes the positive pyroelectric current [14]. Therefore, the positive current peak of the ceramic poled at 100°C is much weaker than that of the ceramic poled at room temperature.

After comparing the steady photocurrents of the ceramics poled at room temperature and 100°C, it is noted that the steady photocurrent of the BCT-Fe-0.025-Air ceramic is significantly enhanced by the poling at 100°C. It is suggested that oxygen vacancies accumulated near the bottom electrode will contribute to the photocurrent response. As a result, the ferroelectric photocurrent effect and the drift current caused by the accumulation of oxygen vacancies combine to generate a larger photocurrent response. It has been demonstrated that the photocurrent response of the BCT-Fe-0.025-Air ceramic can be enhanced by poling at high temperatures.

5.4. Conclusions

Photocurrent responses of the ferroelectric BCT-Fe-0.025 ceramics (sintered in N_2, Air and O_2) are investigated with symmetric Au electrode configurations. A solar simulator (Newport 91160,300W) with AM 1.5 G filter (100mW/cm^2) is used as a light source for the investigation.

With the purpose of studying the ferroelectric photovoltaic effect, all the BCT-Fe-0.025 ceramics are poled under an electric field of 1 kV/mm at room temperature before the photocurrent measurements. The switchable and polarization-dependent photocurrent responses are successfully demonstrated in all the ceramics. Both a sharp current peak and steady current are observed in all the ceramics. It is believed that the pyroelectric effect is the dominant effect contributing to the sharp current peak, while the ferroelectric photovoltaic effect is responsible for the steady photocurrent. Among the ceramics sintered in different atmospheres, the ceramic sintered in Air (i.e., BCT-Fe-0.025-Air) exhibits the highest current peak (48.4 nA/cm^2) and steady photocurrent (6.68 nA/cm^2). The BCT-Fe-0.025-N_2 ceramic exhibits a slightly weaker current peak (47.1 nA/cm^2) and steady photocurrent (6.40 nA/cm^2), while both the current peak and steady photocurrent of the BCT-Fe-0.025-O2 ceramic are the weakest (29.7 nA/cm^2 and 4.4 nA/cm^2, respectively). It is believed that both the pyroelectric and ferroelectric photovoltaic responses are dependent on the polarization of ferroelectric ceramics. The P-E loops show that the remnant polarization of the BCT-Fe-0.025-Air, BCT-Fe-0.025-N_2 and BCT-Fe-0.025-O_2 ceramics are 4.5 μC/cm^2, 3.8 μC/cm^2 and 2.5 μC/cm^2 respectively. Since the BCT-Fe-0.025-Air ceramic has the largest remnant polarization, it exhibits the best photocurrent response.

To investigate the influence of defects (oxygen vacancies) on the photocurrent response in ferroelectric ceramics, an electric field of 1 kV/mm is applied to the BCT-Fe-0.025 ceramics at 100^{o}C for poling the ceramics and redistributing the oxygen vacancies. No significant change in the photocurrent response of the BCT-Fe-0.025-O_2 ceramic is observed after the poling at 100^{o}C. For the BCT-Fe-0.025-N_2 ceramic, no current peaks are observed when the illumination is switched on/off. In addition, the steady photocurrents of the BCT-Fe-0.025-O_2 and BCT-Fe-0.025-N_2 ceramics are not improved. On the other hand, the photocurrent response of the BCT-Fe-0.025-Air ceramic is significantly enhanced after the poling at 100^{o}C.

In conclusion, the sintering atmosphere will affect the ferroelectric properties (remnant polarization) of the BCT-Fe-0.025 ceramics and thus affect their photocurrent responses. Moreover, the weak photocurrent response of the BCT-Fe-0.025-Air ceramic can be enhanced via poling at high temperatures. It is suggested that the accumulation of oxygen vacancies can produce additional diffusion current and drift current to enhance the photocurrent responses of the ferroelectric ceramics.

Chapter 6. Conclusions

This study demonstrates the influence of the sintering atmosphere and oxygen vacancies on the photocurrent response of the ferroelectric BCT-Fe-0.025 ceramics and non-ferroelectric BCT-Fe-0.1 ceramics. It shows that the sintering atmosphere will affect the dielectric and ferroelectric properties of the ceramics, thus leading to different photocurrent responses. In addition, photocurrent responses can be observed in non-ferroelectric oxides with symmetric electrode configuration (i.e., the top and bottom electrodes are of the same material). Switchable current responses are achieved in non-ferroelectric BCT-Fe-0.1 ceramics by modifying the distribution of oxygen vacancies. The photocurrent of the ferroelectric ceramics can be enhanced by redistributing the oxygen vacancies.

The BCT-Fe-0.025 and BCT-Fe-0.1 ceramics have been fabricated by a conventional solid-state reaction. The ceramics are sintered in different atmospheres (N_2, Air and O_2). The XRD results show that all the ceramics have a pure perovskite structure. The dielectric and ferroelectric properties of the BCT-Fe-0.1 and BCT-Fe-0.025 ceramics sintered in different atmospheres (N_2, Air and O_2) have been studied. The XPS results show that the ceramics will contain more oxygen vacancies when they are sintered in an oxygen-deficient atmosphere (e.g. N_2 atmosphere). The dielectric loss of the ceramics increases when they are sintered in the atmosphere with higher oxygen concentrations. For the BCT-Fe-0.025 ceramics, a ferroelectric tetragonal phase to the non-ferroelectric cubic phase transition is observed. The observed T_c varies slightly with the sintering atmosphere (O_2~ 53^{o}C, Air ~54^{o}C, N_2 ~56^{o}C). Since the BCT-Fe-0.025 ceramics remain the ferroelectric tetragonal structure at room temperature, they exhibit a large P_r. In addition, the sintering atmosphere has a great effect on the ferroelectric properties of the BCT-Fe-0.025 ceramics. The BCT-Fe-0.025-O_2 ceramic has the lowest P_r (2.5 μC/cm^2) and P_s (10

$\mu C/cm^2$). The P_r and P_s of the BCT-Fe-0.025-N_2 ceramic are 3.8 $\mu C/cm^2$ and 15 $\mu C/cm^2$, respectively. The BCT-Fe-0.025-Air ceramic has the highest P_r (4.5 $\mu C/cm^2$) and P_s (18 $\mu C/cm^2$). These differences in ferroelectric properties will play a non-neglectable role in the photocurrent response of the BCT-Fe-0.025 ceramics. For the BCT-Fe-0.1 ceramics, no phase transitions are observed in the temperature range of -50^{o}C to 150^{o}C. The P-E Loops confirm that they are non-ferroelectric at room temperature. The optical bandgaps of the BCT-Fe-0.1 ceramics sintered in O_2 (~2.69 eV), air (~2.67 eV) and N_2 (~2.60 eV) are also measured. The BCT-Fe-0.025 ceramics sintered in different atmospheres exhibit similar bandgaps (2.75 eV).

The photocurrent responses of the BCT-Fe-0.1 and BCT-Fe-0.025 ceramics have been investigated using the symmetric electrode configuration (i.e., the top and bottom electrodes are of the same material). Since the BCT-Fe-0.1 ceramics are non-ferroelectric, they should exhibit no photocurrent response. However, photocurrent responses have been observed in the BCT-Fe-0.1 ceramics. It is suggested that the observed photocurrent responses are related to the accumulation of oxygen vacancies near one side of the ceramics. The uneven distribution of the oxygen vacancies will generate an electric field for inducing a drift current. The photocurrent responses of the BCT-Fe-0.1 ceramics have first been investigated using symmetric ITO electrode configurations. During a 30-second solar light illumination, the observed photocurrent of the BCT-Fe-0.1-O_2 ceramic is the largest (~6.9 nA/cm^2), and that of the BCT-Fe-0.1-Air is slightly lower (~4.8 nA/cm^2). On the other hand, the BCT-Fe-0.1-N_2 ceramic exhibits only sharp current peaks when the illumination is switched on/off, but no steady photocurrent during the illumination. It is suggested that the BCT-Fe-0.1-N_2 ceramic contains more non- accumulated oxygen vacancies which trap and recombine with the photo-induced electron. As a result, due to

the charge recombination, the photocurrent generated by the BCT-Fe-0.2-N_2 ceramic is the lowest (only sharp current peaks are observed when the illumination is switched on/off). An electric field of 2.5 kV/mm is applied to the BCT-Fe-0.1 ceramics at room temperature with the aim of changing the distribution of oxygen vacancies. No observable changes in photocurrent responses are observed for all the BCT-Fe-0.1 ceramics. However, if the electric field (1.5 kV/mm) is applied at 100^{o}C, the observed photocurrent responses become different. Since ITO is sensitive to high temperature and high electric field, the ceramics with symmetric Au electrode configuration have also been used for the investigation, and similar results have been observed. Our results show that the magnitude and direction of the photocurrent can be modified by an external electric field. It is suggested that the distribution of oxygen vacancies can be modulated by a high external electric field at high temperatures, thus leading to a switchable photocurrent response. The effects of the sintering atmosphere on the photocurrent response of the BCT-Fe-0.1 ceramics have also been investigated.

Photocurrent responses of the ferroelectric BCT-Fe-0.025 ceramics with symmetric Au electrode configuration have been investigated. All the ceramics are poled under an electric field of 1 kV/mm at room temperature. Both a sharp pyroelectric current peak and steady ferroelectric photovoltaic current are observed in all the ceramics. The steady photocurrent generated by the BCT-Fe-0.025 ceramics sintered in air, N_2 and O_2 are 06.68 nA/cm^2, 6.4 nA/cm^2 and 4.4 nA/cm^2, respectively. Among them, The BCT-Fe-0.025-O_2 ceramic exhibits the lowest pyroelectric current peak and steady photocurrent. The ferroelectric photovoltaic response and pyroelectric effect are dependent on the remnant polarization. The P-E hysteresis loops show that the remnant polarization of the BCT-Fe-0.025-O_2 ceramic is the lowest and therefore it exhibits the weakest photocurrent response.

Similar to BCT-Fe-0.1, an electric field (1 kV/mm) has been applied to the BCT-Fe-0.025 ceramics at 100ºC for adjusting the distribution of oxygen vacancies as well as poling the ceramics. No significant changes in the photocurrent responses are observed for the BCT-Fe-0.025 ceramics sintered in N_2 and O_2. However, a significant enhancement in the photocurrent response is observed for the BCT-Fe-0.025-Air ceramic.

To conclude, our results show that the sintering atmosphere plays an important role in the photocurrent responses of the ceramics. The BCT-Fe-0.1-O_2 ceramic exhibits the strongest photocurrent responses. In addition, switchable photocurrent response can be obtained in non-ferroelectric ceramics which provides evidence that oxygen vacancies can play an important role in the photocurrent response. It is believed that the concentration of oxygen vacancies in the ceramic can be controlled by the sintering atmosphere, and their distribution can be modified by an external electric field. Moreover, the accumulation of oxygen vacancies may induce additional photocurrent responses.

Reference

[1] N. Ma and Y. Yang, 'Boosted photocurrent in ferroelectric BaTiO3 materials via two dimensional planar-structured contact configurations', *Nano Energy*, vol. 50, pp. 417–424, Aug. 2018, doi: 10.1016/j.nanoen.2018.05.069.

[2] S. Y. Yang *et al.*, 'Above-bandgap voltages from ferroelectric photovoltaic devices', *Nat. Nanotechnol.*, vol. 5, no. 2, pp. 143–147, Feb. 2010, doi: 10.1038/nnano.2009.451.

[3] Y. Yuan, Z. Xiao, B. Yang, and J. Huang, 'Arising applications of ferroelectric materials in photovoltaic devices', *J Mater Chem A*, vol. 2, no. 17, pp. 6027–6041, 2014, doi: 10.1039/C3TA14188H.

[4] R. R. Mehta, B. D. Silverman, and J. T. Jacobs, 'Depolarization fields in thin ferroelectric films', *J. Appl. Phys.*, vol. 44, no. 8, pp. 3379–3385, Aug. 1973, doi: 10.1063/1.1662770.

[5] D. Damjanovic, 'Ferroelectric, dielectric and piezoelectric properties of ferroelectric thin films and ceramics', *Rep. Prog. Phys.*, vol. 61, no. 9, pp. 1267–1324, Sep. 1998, doi: 10.1088/0034-4885/61/9/002.

[6] A. G. Chynoweth, 'Surface Space-Charge Layers in Barium Titanate', *Phys. Rev.*, vol. 102, no. 3, pp. 705–714, May 1956, doi: 10.1103/PhysRev.102.705.

[7] R. W. Whatmore, 'Pyroelectric devices and materials', *Rep. Prog. Phys.*, vol. 49, no. 12, pp. 1335–1386, Dec. 1986, doi: 10.1088/0034-4885/49/12/002.

[8] H. He, Z. He, Z. Jiang, J. Wang, T. Liu, and N. Wang, 'A controllable photoresponse and photovoltaic performance in Bi4Ti3O12 ferroelectric thin films', *J. Alloys Compd.*, vol. 694, pp. 998–1003, Feb. 2017, doi: 10.1016/j.jallcom.2016.10.160.

[9] C. Ge *et al.*, 'Toward Switchable Photovoltaic Effect via Tailoring Mobile Oxygen Vacancies in Perovskite Oxide Films', *ACS Appl. Mater. Interfaces*, vol. 8, no. 50, pp. 34590–34597, Dec. 2016, doi: 10.1021/acsami.6b13203.

[10] N. Ma, K. Zhang, and Y. Yang, 'Photovoltaic–Pyroelectric Coupled Effect Induced Electricity for Self-Powered Photodetector System', *Adv. Mater.*, vol. 29, no. 46, p. 1703694, Dec. 2017, doi: 10.1002/adma.201703694.

[11] A. Bihari Swain, D. Murali, B. R. K. Nanda, and P. Murugavel, 'Large Bulk Photovoltaic Response by Symmetry-Breaking Structural Transformation in Ferroelectric [Ba (Zr 0.2 Ti 0.8) O 3] $_{0.5}$ [(Ba 0.7 Ca 0.3) Ti O 3] $_{0.5}$', *Phys. Rev. Appl.*, vol. 11, no. 4, p. 044007, Apr. 2019, doi: 10.1103/PhysRevApplied.11.044007.

[12] T. Yang, J. Wei, Y. Guo, Z. Lv, Z. Xu, and Z. Cheng, 'Manipulation of Oxygen Vacancy for High Photovoltaic Output in Bismuth Ferrite Films', *ACS Appl. Mater. Interfaces*, vol. 11, no. 26, pp. 23372–23381, Jul. 2019, doi: 10.1021/acsami.9b06704.

[13] Z. Tan *et al.*, 'Thinning ferroelectric films for high-efficiency photovoltaics based on the Schottky barrier effect', *NPG Asia Mater.*, vol. 11, no. 1, p. 20, Dec. 2019, doi: 10.1038/s41427-019-0120-3.

[14] Z. Bai, W. Geng, Y. Zhang, S. Xu, H. Guo, and A. Jiang, 'The abnormal photovoltaic effect in BiFeO3 thin films modulated by bipolar domain orientations and oxygen-vacancy migration', *Appl. Phys. A*, vol. 123, no. 8, p. 561, Aug. 2017, doi: 10.1007/s00339-017-1165-1.

[15] R. L. Gao, H. W. Yang, Y. S. Chen, J. R. Sun, Y. G. Zhao, and B. G. Shen, 'Oxygen vacancies induced switchable and nonswitchable photovoltaic effects in Ag/Bi $_{0.9}$ La $_{0.1}$ FeO $_3$ /La $_{0.7}$ Sr $_{0.3}$ MnO $_3$ sandwiched capacitors', *Appl. Phys. Lett.*, vol. 104, no. 3, p. 031906, Jan. 2014, doi: 10.1063/1.4862793.

[16] Z. Liao, P. Gao, X. Bai, D. Chen, and J. Zhang, 'Evidence for electric-field-driven migration and diffusion of oxygen vacancies in Pr $_{0.7}$ Ca $_{0.3}$ MnO $_3$', *J. Appl. Phys.*, vol. 111, no. 11, p. 114506, Jun. 2012, doi: 10.1063/1.4724333.

[17] F. Zhang, C. Li, H. Li, X. Guo, and S. Fan, 'Ceramic Processing Research', p. 4.

[18] Y. W. Li *et al.*, 'Oxygen-vacancy-related dielectric relaxation in BiFeO $_3$ films grown by pulsed laser deposition', *J. Phys. Appl. Phys.*, vol. 41, no. 21, p. 215403, Nov. 2008, doi: 10.1088/0022-3727/41/21/215403.

[19] J. Wu, J. Wang, D. Xiao, and J. Zhu, 'Migration Kinetics of Oxygen Vacancies in Mn-Modified BiFeO $_3$ Thin Films', *ACS Appl. Mater. Interfaces*, vol. 3, no. 7, pp. 2504–2511, Jul. 2011, doi: 10.1021/am2003747.

[20] Y. H. Han, J. B. Appleby, and D. M. Smyth, 'Calcium as an Acceptor Impurity in BaTiO3', *J. Am. Ceram. Soc.*, vol. 70, no. 2, pp. 96–100, Feb. 1987, doi: 10.1111/j.1151-2916.1987.tb04936.x.

[21] W. Ji, K. Yao, and Y. C. Liang, 'Bulk Photovoltaic Effect at Visible Wavelength in Epitaxial Ferroelectric BiFeO $_3$ Thin Films', *Adv. Mater.*, vol. 22, no. 15, pp. 1763–1766, Apr. 2010, doi: 10.1002/adma.200902985.

[22] Y. Zhang, H. Sun, and W. Chen, 'A brief review of Ba(Ti 0.8 Zr 0.2)O 3 -(Ba 0.7 Ca 0.3)TiO 3 based lead-free piezoelectric ceramics: Past, present and future perspectives', *J. Phys. Chem. Solids*, vol. 114, pp. 207–219, Mar. 2018, doi: 10.1016/j.jpcs.2017.10.041.

[23] J. A. Gonzalo, Ed., *Ferroelectricity: the fundamentals collection*. Weinheim: Wiley-VCH, 2005.

[24] A. Zenkevich, Yu. Matveyev, K. Maksimova, R. Gaynutdinov, A. Tolstikhina, and V. Fridkin, 'Giant bulk photovoltaic effect in thin ferroelectric BaTiO 3 films', *Phys. Rev. B*, vol. 90, no. 16, p. 161409, Oct. 2014, doi: 10.1103/PhysRevB.90.161409.

[25] G. H. Haertling, 'Ferroelectric Ceramics: History and Technology', *J. Am. Ceram. Soc.*, vol. 82, no. 4, pp. 797–818, Apr. 1999, doi: 10.1111/j.1151-2916.1999.tb01840.x.

[26] H. Zhang *et al.*, 'A review on the development of lead-free ferroelectric energy-storage ceramics and multilayer capacitors', *J. Mater. Chem. C*, vol. 8, no. 47, pp. 16648–16667, 2020, doi: 10.1039/D0TC04381H.

[27] M. R. Panigrahi and S. Panigrahi, 'Synthesis and microstructure of Ca-doped BaTiO3 ceramics prepared by high-energy ball-milling', *Phys. B Condens. Matter*, vol. 404, no. 21, pp. 4267–4272, Nov. 2009, doi: 10.1016/j.physb.2009.08.012.

[28] K. Lhoussain, E. Abdelilah, and S. Salaheddine, 'Dielectric study of calcium doped barium titanate Ba1-xCaxTiO3 ceramics', *Int. J. Phys. Sci.*, vol. 11, no. 6, pp. 71–79, Mar. 2016, doi: 10.5897/IJPS2015.4415.

[29] A. Rani, J. Kolte, S. S. Vadla, and P. Gopalan, 'Structural, electrical, magnetic and magnetoelectric properties of Fe doped BaTiO3 ceramics', *Ceram. Int.*, vol. 42, no. 7, pp. 8010–8016, May 2016, doi: 10.1016/j.ceramint.2016.01.205.

[30] T. M. Kamel and G. de With, 'Grain size effect on the poling of soft Pb(Zr,Ti)O3 ferroelectric ceramics', *J. Eur. Ceram. Soc.*, vol. 28, no. 4, pp. 851–861, Jan. 2008, doi: 10.1016/j.jeurceramsoc.2007.08.010.

[31] S. Pal *et al.*, 'Giant photovoltaic response in band engineered ferroelectric perovskite', *Sci. Rep.*, vol. 8, no. 1, p. 8005, Dec. 2018, doi: 10.1038/s41598-018-26205-x.

[32] S. Malato, P. Fernández-Ibáñez, M. I. Maldonado, J. Blanco, and W. Gernjak, 'Decontamination and disinfection of water by solar photocatalysis: Recent overview and trends', *Catal. Today*, vol. 147, no. 1, pp. 1–59, Sep. 2009, doi: 10.1016/j.cattod.2009.06.018.

[33] A. Matsumura, Y. Kamaike, T. Horiuchi, M. Shimizu, T. Shiosaki, and K. Matsushige, 'Thermal Effects in Properties of Photovoltaic Currents of $Pb(Zr,Ti)O_3$ Thin Films', *Jpn. J. Appl. Phys.*, vol. 34, no. Part 1, No. 9B, pp. 5258–5262, Sep. 1995, doi: 10.1143/JJAP.34.5258.

[34] W. Ji, K. Yao, and Y. C. Liang, 'Evidence of bulk photovoltaic effect and large tensor coefficient in ferroelectric BiFeO 3 thin films', *Phys. Rev. B*, vol. 84, no. 9, p. 094115, Sep. 2011, doi: 10.1103/PhysRevB.84.094115.

[35] Z. Gu *et al.*, 'Mesoscopic Free Path of Nonthermalized Photogenerated Carriers in a Ferroelectric Insulator', *Phys. Rev. Lett.*, vol. 118, no. 9, p. 096601, Mar. 2017, doi: 10.1103/PhysRevLett.118.096601.

[36] M. Qin, K. Yao, and Y. C. Liang, 'Photovoltaic mechanisms in ferroelectric thin films with the effects of the electrodes and interfaces', *Appl. Phys. Lett.*, vol. 95, no. 2, p. 022912, Jul. 2009, doi: 10.1063/1.3182824.

[37] J. Seidel *et al.*, 'Efficient Photovoltaic Current Generation at Ferroelectric Domain Walls', *Phys. Rev. Lett.*, vol. 107, no. 12, p. 126805, Sep. 2011, doi: 10.1103/PhysRevLett.107.126805.

[38] P. Wurfel and I. P. Batra, 'Depolarization-Field-Induced Instability in Thin Ferroelectric Films—Experiment and Theory', *Phys. Rev. B*, vol. 8, no. 11, pp. 5126–5133, Dec. 1973, doi: 10.1103/PhysRevB.8.5126.

[39] Y. S. Yang *et al.*, 'Schottky barrier effects in the photocurrent of sol–gel derived lead zirconate titanate thin film capacitors', *Appl. Phys. Lett.*, vol. 76, no. 6, pp. 774–776, Feb. 2000, doi: 10.1063/1.125891.

[40] 'Photovoltaic characteristics in polycrystalline and epitaxial (Pb0.97La0.03)(Zr0.52Ti0.48)O3 ferroelectric thin films sandwiched between different top and bottom electrodes', *J Appl Phys*, p. 8.

[41] L. Pintilie, C. Dragoi, and I. Pintilie, 'Interface controlled photovoltaic effect in epitaxial Pb(Zr,Ti)O $_3$ films with tetragonal structure', *J. Appl. Phys.*, vol. 110, no. 4, p. 044105, Aug. 2011, doi: 10.1063/1.3624738.

[42] S. Y. Yang *et al.*, 'Photovoltaic effects in BiFeO3', *Appl. Phys. Lett.*, vol. 95, no. 6, p. 062909, Aug. 2009, doi: 10.1063/1.3204695.

[43] L. Fang, L. You, Y. Zhou, P. Ren, Z. Shiuh Lim, and J. Wang, 'Switchable photovoltaic response from polarization modulated interfaces in BiFeO $_3$ thin films', *Appl. Phys. Lett.*, vol. 104, no. 14, p. 142903, Apr. 2014, doi: 10.1063/1.4870972.

[44] D. Lee *et al.*, 'Polarity control of carrier injection at ferroelectric/metal interfaces for electrically switchable diode and photovoltaic effects', *Phys. Rev. B*, vol. 84, no. 12, p. 125305, Sep. 2011, doi: 10.1103/PhysRevB.84.125305.

[45] L. Pintilie, I. Vrejoiu, G. Le Rhun, and M. Alexe, 'Short-circuit photocurrent in epitaxial lead zirconate-titanate thin films', *J. Appl. Phys.*, vol. 101, no. 6, p. 064109, Mar. 2007, doi: 10.1063/1.2560217.

[46] R. Nechache *et al.*, 'Bandgap tuning of multiferroic oxide solar cells', *Nat. Photonics*, vol. 9, no. 1, pp. 61–67, Jan. 2015, doi: 10.1038/nphoton.2014.255.

[47] Y. Noguchi, H. Matsuo, Y. Kitanaka, and M. Miyayama, 'Ferroelectrics with a controlled oxygen-vacancy distribution by design', *Sci. Rep.*, vol. 9, no. 1, p. 4225, Dec. 2019, doi: 10.1038/s41598-019-40717-0.

[48] M. W. Allen and S. M. Durbin, 'Influence of oxygen vacancies on Schottky contacts to ZnO', *Appl. Phys. Lett.*, vol. 92, no. 12, p. 122110, Mar. 2008, doi: 10.1063/1.2894568.

[49] S. Starschich, S. Menzel, and U. Böttger, 'Evidence for oxygen vacancies movement during wake-up in ferroelectric hafnium oxide', *Appl. Phys. Lett.*, vol. 108, no. 3, p. 032903, Jan. 2016, doi: 10.1063/1.4940370.

[50] J. Wang *et al.*, 'Oxygen Vacancy Induced Band-Gap Narrowing and Enhanced Visible Light Photocatalytic Activity of ZnO', *ACS Appl. Mater. Interfaces*, vol. 4, no. 8, pp. 4024–4030, Aug. 2012, doi: 10.1021/am300835p.

[51] T. Aizawa, I. Fujii, S. Ueno, T. S. Suzuki, and S. Wada, 'Effect of oxygen partial pressure during sintering on electric properties of $BiFeO_3$-based piezoelectric ceramics', *J. Ceram. Soc. Jpn.*, vol. 127, no. 6, pp. 383–387, Jun. 2019, doi: 10.2109/jcersj2.19001.

[52] Y.-K. Paek, J.-H. Ahn, G.-H. Kim, and S.-J. L. Kang, 'Effect of Nitrogen Atmosphere on the Densification of a 3-mol%-Yttria-Doped Zirconia', *J. Am. Ceram. Soc.*, vol. 85, no. 6, pp. 1631–1633, Jun. 2002, doi: 10.1111/j.1151-2916.2002.tb00327.x.

[53] J. Jiang *et al.*, 'Effects of sintering atmosphere on the densification and microstructure of yttrium aluminum garnet fibers prepared by sol-gel process', *J. Eur. Ceram. Soc.*, vol. 39, no. 16, pp. 5332–5337, Dec. 2019, doi: 10.1016/j.jeurceramsoc.2019.08.033.

[54] Z. Yao *et al.*, 'Greatly reduced leakage current and defect mechanism in atmosphere sintered BiFeO3–BaTiO3 high temperature piezoceramics', *J. Mater. Sci. Mater. Electron.*, vol. 25, no. 11, pp. 4975–4982, Nov. 2014, doi: 10.1007/s10854-014-2260-0.

[55] C. Voisin, S. Guillemet-Fritsch, P. Dufour, C. Tenailleau, H. Han, and J. C. Nino, 'Influence of Oxygen Substoichiometry on the Dielectric Properties of $BaTiO_{3-\delta}$ Nanoceramics Obtained by Spark Plasma Sintering', *Int. J. Appl. Ceram. Technol.*, vol. 10, pp. E122–E133, Sep. 2013, doi: 10.1111/ijac.12058.

[56] K. Bakken, 'Sintering of lead-free piezoelectric materials', p. 96.

[57] J. Liu, Y. Gao, X. Wu, G. Jin, Z. Zhai, and H. Liu, 'Inhomogeneous Oxygen Vacancy Distribution in Semiconductor Gas Sensors: Formation, Migration and Determination on Gas Sensing Characteristics', *Sensors*, vol. 17, no. 8, p. 1852, Aug. 2017, doi: 10.3390/s17081852.

[58] V. Lo, W. W. Chung, H. Cao, and X. Dai, 'Investigating the effect of oxygen vacancy on the dielectric and electromechanical properties in ferroelectric ceramics', *J. Appl. Phys.*, vol. 104, no. 6, p. 064105, Sep. 2008, doi: 10.1063/1.2978376.

[59] H. T. Yi, T. Choi, S. G. Choi, Y. S. Oh, and S.-W. Cheong, 'Mechanism of the Switchable Photovoltaic Effect in Ferroelectric BiFeO3', *Adv. Mater.*, vol. 23, no. 30, pp. 3403–3407, Aug. 2011, doi: 10.1002/adma.201100805.

[60] C. Slouka *et al.*, 'The Effect of Acceptor and Donor Doping on Oxygen Vacancy Concentrations in Lead Zirconate Titanate (PZT)', *Materials*, vol. 9, no. 11, p. 945, Nov. 2016, doi: 10.3390/ma9110945.

[61] P. Goudochnikov and A. J. Bell, 'Correlations between transition temperature, tolerance factor and cohesive energy in 2+:4+ perovskites', *J. Phys. Condens. Matter*, vol. 19, no. 17, p. 176201, Apr. 2007, doi: 10.1088/0953-8984/19/17/176201.

[62] P. Pal, K. Rudrapal, P. Maji, A. R. Chaudhuri, and D. Choudhury, 'Toward an Enhanced Room-Temperature Photovoltaic Effect in Ferroelectric Bismuth and Iron Codoped $BaTiO_3$', *J. Phys. Chem. C*, vol. 125, no. 9, pp. 5315–5326, Mar. 2021, doi: 10.1021/acs.jpcc.0c10655.

[63] Kane Phlip and Graydon B .LArrabee, *Characterization of solid surfaces*. New York : Plenum Press, 1974.

[64] U. B. Gawas, V. K. Mandrekar, and M. S. Majik, 'Structural analysis of proteins using X-ray diffraction technique', in *Advances in Biological Science Research*, Elsevier, 2019, pp. 69–84. doi: 10.1016/B978-0-12-817497-5.00005-7.

[65] J. F. Watts and J. Wolstenholme, *An introduction to surface analysis by XPS and AES*, Second edition. Hoboken: Wiley, 2019.

[66] Y. Tu *et al.*, 'Control of oxygen vacancies in ZnO nanorods by annealing and their influence on ZnO/PEDOT:PSS diode behaviour', *J. Mater. Chem. C*, vol. 6, no. 7, pp. 1815–1821, 2018, doi: 10.1039/C7TC04284A.

[67] M. Wegmann, L. Watson, and A. Hendry, 'XPS Analysis of Submicrometer Barium Titanate Powder', *J. Am. Ceram. Soc.*, vol. 87, no. 3, pp. 371–377, Mar. 2004, doi: 10.1111/j.1551-2916.2004.00371.x.

[68] S. R. Reddy, V. V. B. Prasad, S. Bysakh, V. Shanker, N. Hebalkar, and S. K. Roy, 'Superior energy storage performance and fatigue resistance in ferroelectric BCZT thin films grown in an oxygen-rich atmosphere', *J. Mater. Chem. C*, vol. 7, no. 23, pp. 7073–7082, 2019, doi: 10.1039/C9TC00569B.

[69] S. Chen, M. E. A. Warwick, and R. Binions, 'Effects of film thickness and thermal treatment on the structural and opto-electronic properties of Ga-doped ZnO films deposited by sol–gel method', *Sol. Energy Mater. Sol. Cells*, vol. 137, pp. 202–209, Jun. 2015, doi: 10.1016/j.solmat.2015.02.016.

[70] W. Cai *et al.*, 'Effects of oxygen partial pressure on the electrical properties and phase transitions in (Ba,Ca)(Ti,Zr)O3 ceramics', *J. Mater. Sci.*, vol. 55, no. 23, pp. 9972–9992, Aug. 2020, doi: 10.1007/s10853-020-04771-8.

[71] S. Jaiswar and K. D. Mandal, 'Evidence of Enhanced Oxygen Vacancy Defects Inducing Ferromagnetism in Multiferroic $CaMn_7O_{12}$ Manganite with Sintering Time', *J. Phys. Chem. C*, vol. 121, no. 36, pp. 19586–19601, Sep. 2017, doi: 10.1021/acs.jpcc.7b05415.

[72] P. J. Brimmer and P. R. Griffiths, 'Angular Dependence of Diffuse Reflectance Infrared Spectra. Part III: Linearity of Kubelka-Munk Plots', *Appl. Spectrosc.*, vol. 42, no. 2, pp. 242–247, Feb. 1988, doi: 10.1366/0003702884428293.

[73] S. Yang, Y. Liu, Y. Zhang, and D. Mo, 'Investigation of annealing-treatment on structural and optical properties of sol-gel-derived zinc oxide thin films', *Bull. Mater. Sci.*, vol. 33, no. 3, pp. 209–214, Jun. 2010, doi: 10.1007/s12034-010-0032-x.

[74] J. B. Coulter and D. P. Birnie, 'Assessing Tauc Plot Slope Quantification: ZnO Thin Films as a Model System', *Phys. Status Solidi B*, vol. 255, no. 3, p. 1700393, Mar. 2018, doi: 10.1002/pssb.201700393.

[75] K. Albertsen, D. Hennings, and O. Steigelmann, 'Donor-Acceptor Charge Complex Formation in Barium Titanate Ceramics: Role of Firing Atmosphere', p. 6.

[76] A. Chawla, A. Singh, P. D. Babu, and M. Singh, 'Magnetic ion oxidation state dependent magnetoelectric coupling strength in Fe doped BCT ceramics', *RSC Adv.*, vol. 10, no. 35, pp. 21019–21027, 2020, doi: 10.1039/D0RA00969E.

[77] B. C. Keswani *et al.*, 'Correlation between structural, magnetic and ferroelectric properties of Fe-doped (Ba-Ca)TiO3 lead-free piezoelectric', *J. Alloys Compd.*, vol. 712, pp. 320–333, Jul. 2017, doi: 10.1016/j.jallcom.2017.03.301.

[78] H. Nakayama and H. Katayama-Yoshida, 'Theoretical Prediction of Magnetic Properties of Ba(Ti1-xMx)O3 (M=Sc,V,Cr,Mn,Fe,Co,Ni,Cu)', *Jpn. J. Appl. Phys.*, vol. 40, no. Part 2, No. 12B, pp. L1355–L1358, Dec. 2001, doi: 10.1143/JJAP.40.L1355.

[79] Z. Guo *et al.*, 'Structural and multiferroic properties of Fe-doped Ba0.5Sr0.5TiO3 solids', *J. Magn. Magn. Mater.*, vol. 325, pp. 24–28, Jan. 2013, doi: 10.1016/j.jmmm.2012.08.023.

[80] D.-H. Yoon, 'Ceramic Processing Research', p. 13.

[81] İ. C. Kaya, V. Kalem, and H. Akyildiz, 'Hydrothermal synthesis of pseudocubic $BaTiO_3$ nanoparticles using TiO_2 nanofibers: Study on photocatalytic and dielectric properties', *Int. J. Appl. Ceram. Technol.*, vol. 16, no. 4, pp. 1557–1569, Jul. 2019, doi: 10.1111/ijac.13225.

[82] D. P. Dutta, M. Roy, N. Maiti, and A. K. Tyagi, 'Phase evolution in sonochemically synthesized Fe^{3+} doped $BaTiO_3$ nanocrystallites: structural, magnetic and ferroelectric characterisation', *Phys. Chem. Chem. Phys.*, vol. 18, no. 14, pp. 9758–9769, 2016, doi: 10.1039/C5CP07736B.

[83] Z. Quan *et al.*, 'Surface chemical bonding states and ferroelectricity of Ce-doped BiFeO3 thin films prepared by sol–gel process', *J. Sol-Gel Sci. Technol.*, vol. 48, no. 3, pp. 261–266, Dec. 2008, doi: 10.1007/s10971-008-1825-x.

[84] B. Wang, Y.-P. Pu, H.-D. Wu, K. Chen, and N. Xu, 'Influence of sintering atmosphere on dielectric properties and microstructure of CaCu3Ti4O12 ceramics', *Ceram. Int.*, vol. 39, pp. S525–S528, May 2013, doi: 10.1016/j.ceramint.2012.10.127.

[85] V. R. Mudinepalli, L. Feng, W.-C. Lin, and B. S. Murty, 'Effect of grain size on dielectric and ferroelectric properties of nanostructured Ba0.8Sr0.2TiO3 ceramics', *J. Adv. Ceram.*, vol. 4, no. 1, pp. 46–53, Mar. 2015, doi: 10.1007/s40145-015-0130-8.

[86] Q. Li, J. Cheng, and J. Chen, 'Reduced dielectric loss and enhanced piezoelectric properties of Mn modified 0.71BiFeO3–0.29BaTiO3 ceramics sintered under oxygen atmosphere', *J. Mater. Sci. Mater. Electron.*, vol. 28, no. 2, pp. 1370–1377, Jan. 2017, doi: 10.1007/s10854-016-5670-3.

[87] Y. Tan *et al.*, 'Unfolding grain size effects in barium titanate ferroelectric ceramics', *Sci. Rep.*, vol. 5, no. 1, p. 9953, Sep. 2015, doi: 10.1038/srep09953.

[88] Y. Li, M. Borbely, and A. Bell, 'The influence of oxygen vacancies on piezoelectricity in samarium-doped Pb(Mg $_{1/3}$ Nb $_{2/3}$)O $_3$ -PbTiO $_3$ ceramics', *J. Am. Ceram. Soc.*, vol. 104, no. 6, pp. 2678–2688, Jun. 2021, doi: 10.1111/jace.17619.

[89] F. Zhang, L. Zhang, X. Guo, S. Yang, Q. Tian, and S. Fan, 'The effect of sintering atmospheres on the properties of CSBT-0.15 ferroelectric ceramics', *Ceram. Int.*, vol. 44, no. 12, pp. 13502–13506, Aug. 2018, doi: 10.1016/j.ceramint.2018.04.180.

[90] P. Pal, K. Rudrapal, P. Maji, A. R. Chaudhuri, and D. Choudhury, 'Toward an Enhanced Room-Temperature Photovoltaic Effect in Ferroelectric Bismuth and Iron Codoped BaTiO $_3$', *J. Phys. Chem. C*, vol. 125, no. 9, pp. 5315–5326, Mar. 2021, doi: 10.1021/acs.jpcc.0c10655.

[91] B. Choudhury, P. Chetri, and A. Choudhury, 'Annealing temperature and oxygen-vacancy-dependent variation of lattice strain, band gap and luminescence properties of CeO $_2$ nanoparticles', *J. Exp. Nanosci.*, vol. 10, no. 2, pp. 103–114, Jan. 2015, doi: 10.1080/17458080.2013.801566.

[92] H. Matsuo, Y. Kitanaka, R. Inoue, Y. Noguchi, and M. Miyayama, 'Cooperative effect of oxygen-vacancy-rich layer and ferroelectric polarization on photovoltaic properties in BiFeO $_3$ thin film capacitors', *Appl. Phys. Lett.*, vol. 108, no. 3, p. 032901, Jan. 2016, doi: 10.1063/1.4940374.

[93] D. Fukushi, A. Sasaki, H. Hirabayashi, and M. Kitano, 'Effect of oxygen vacancy in tungsten oxide on the photocatalytic activity for decomposition of organic materials in the gas phase', *Microelectron. Reliab.*, vol. 79, pp. 1–4, Dec. 2017, doi: 10.1016/j.microrel.2017.09.025.

[94] X. Pan, M.-Q. Yang, X. Fu, N. Zhang, and Y.-J. Xu, 'Defective TiO2 with oxygen vacancies: synthesis, properties and photocatalytic applications', *Nanoscale*, vol. 5, no. 9, p. 3601, 2013, doi: 10.1039/c3nr00476g.

[95] S. Corby, L. Francàs, A. Kafizas, and J. R. Durrant, 'Determining the role of oxygen vacancies in the photoelectrocatalytic performance of WO_3 for water oxidation', *Chem. Sci.*, vol. 11, no. 11, pp. 2907–2914, 2020, doi: 10.1039/C9SC06325K.

[96] J. Gan *et al.*, 'Oxygen vacancies promoting photoelectrochemical performance of In2O3 nanocubes', *Sci. Rep.*, vol. 3, no. 1, p. 1021, Dec. 2013, doi: 10.1038/srep01021.

[97] M.-G. Han *et al.*, 'Interface-induced nonswitchable domains in ferroelectric thin films', *Nat. Commun.*, vol. 5, no. 1, p. 4693, Dec. 2014, doi: 10.1038/ncomms5693.

[98] Y. Guo, B. Guo, W. Dong, H. Li, and H. Liu, 'Evidence for oxygen vacancy or ferroelectric polarization induced switchable diode and photovoltaic effects in $BiFeO_3$ based thin films', *Nanotechnology*, vol. 24, no. 27, p. 275201, Jul. 2013, doi: 10.1088/0957-4484/24/27/275201.

[99] Y. Guo, B. Guo, W. Dong, H. Li, and H. Liu, 'Evidences for oxygen vacancy or ferroelectric polarization induced switchable diode and photovoltaic effect in BiFeO3 based thin films', p. 3.

[100] O. J. Sandberg, K. Tvingstedt, P. Meredith, and A. Armin, 'Theoretical Perspective on Transient Photovoltage and Charge Extraction Techniques', *J. Phys. Chem. C*, vol. 123, no. 23, pp. 14261–14271, Jun. 2019, doi: 10.1021/acs.jpcc.9b03133.

[101] J. Lee, D.-G. Lim, W. Song, and J. Yi, 'Influence of Annealing Temperature and Atmosphere on the Properties of ITO Films Deposited Using a Powdery Target', *J. Korean Phys. Soc.*, vol. 51, no. 3, p. 1143, Sep. 2007, doi: 10.3938/jkps.51.1143.

[102] O. Tuna, Y. Selamet, G. Aygun, and L. Ozyuzer, 'High quality ITO thin films grown by dc and RF sputtering without oxygen', *J. Phys. Appl. Phys.*, vol. 43, no. 5, p. 055402, Feb. 2010, doi: 10.1088/0022-3727/43/5/055402.

[103] B. Wu, Z. Wu, H. L. Tam, and F. Zhu, 'Contrary interfacial exciton dissociation at metal/organic interface in regular and reverse configuration organic solar cells', *Appl. Phys. Lett.*, vol. 105, no. 10, p. 103302, Sep. 2014, doi: 10.1063/1.4895675.

[104] F. Kurdesau, G. Khripunov, A. F. da Cunha, M. Kaelin, and A. N. Tiwari, 'Comparative study of ITO layers deposited by DC and RF magnetron sputtering at room temperature', *J. Non-Cryst. Solids*, vol. 352, no. 9–20, pp. 1466–1470, Jun. 2006, doi: 10.1016/j.jnoncrysol.2005.11.088.

[105] M. H. Rein, J. Mayandi, E. Monakhov, and A. Holt, 'ANNEALING OF ITO FILMS SPUTTERED WITH ARGON AND OXYGEN', p. 5.

[106] D. S. Ghosh, *Ultrathin Metal Transparent Electrodes for the Optoelectronics Industry*. Heidelberg: Springer International Publishing, 2013. doi: 10.1007/978-3-319-00348-1.

[107] J. He *et al.*, 'Damage study of ITO under high electric ®eld', *Thin Solid Films*, p. 4, 2000.

[108] L. Jin, Y. He, D. Zhang, H. Zhang, M. Wei, and Z. Zhong, 'Near-ultraviolet photodetector based on hexagonal $TmFeO_3$ ferroelectric semiconductor thin film with photovoltaic and pyroelectric effects', *APL Mater.*, vol. 7, no. 12, p. 121105, Dec. 2019, doi: 10.1063/1.5128702.